KU LEUVEN

FACULTY OF SCIENCE

Low-temperature scanning tunneling microscopy and spectroscopy of magnetic Co and Cr dopants at the surface of the topological insulator Bi_2Te_3

Heleen DAUSY

Supervisor: Prof. C. Van Haesendonck
Faculty of Science KU Leuven

Co-supervisor: Prof. M.J. Van Bael
Faculty of Science KU Leuven

Mentor: A. Netsou
Faculty of Science KU Leuven

Thesis presented in
fulfillment of the requirements
for the degree of Master of Science
in Physics

Academic year 2018-2019

Acknowledgements

Many people have contributed to this project, and I would like to thank them all. Advice given by professor Chris Van Haesendonck and professor Margriet Van Bael has been a great help in laying out the roadmap for this thesis. I am particularly grateful for the assistance given by Asteri: thank you for introducing me to the low temperature STM setup, for helping me analyze the STM data and for measuring overnight and in the weekends - all of that with an herniated disc. I really appreciated the help of Sasha: thanks for all the weekends of refilling, for the days you spent tinkering with the cluster setup and of course for the network switch. To Ivan I would like to extend my thanks for taking the time to help me with Auger measurements even though he already had a great deal to do. I owe gratitude to doctor Dmitry Muzychenko of the Scanning Probe and Nanoelectronics Laboratory at Lomonosov Moscow State University for his very valuable simulations. Thank you also to professor Ewald Janssens, for allowing us to use the cluster setup and for the advice on size-selected clusters. The experiment didn't work out this time, but I still learned a lot in the process.

Heleen Dausy
June 2019

Scientific summary

Topological insulators (TIs) are a new class of insulators with intriguing properties and exist in both 2D and 3D. Their bulk is insulating, but their boundaries host metallic states. These conducting states are protected by time reversal symmetry, which makes them robust against nonmagnetic backscattering. Furthermore, the topological boundary states may host exotic quantum phenomena like the quantum anomalous Hall effect when time reversal symmetry is broken. In order to realize these phenomena experimentally, it is necessary for the used TI materials to be intrinsic. However, several TIs are degenerately doped due to structural defects. Because of this, clear identification and understanding of native defects is an important part of TI research. To break time reversal symmetry, great efforts have been made in the magnetic bulk doping of TI materials. Research looking into magnetic doping at the surface has not been as elaborate. Most research performed on magnetic surface doping of TIs has been carried out by spatially averaging techniques, which are not able to probe local phenomena. For this reason, it is interesting to perform an investigation using local techniques like scanning tunneling microscopy and spectroscopy (STM and STS).

In the first part of this thesis, the characterization of the surface of the 3D TI bismuth telluride (Bi_2Te_3) by means of several surface analysis techniques is described and results are presented. Using STM, STS and Auger electron spectroscopy (AES), the native defects of the crystal are studied. Where possible, they are identified with the help of density functional theory (DFT) based simulated images or literature. Low-energy electron diffraction (LEED) reveals that there is surface reconstruction. Scattering events happening at the bare surface are studied through STS. The results show that backscattering is indeed forbidden at certain energies. The surface states have a linear dispersion, as expected for massless Dirac fermions. The dispersion shows that the Dirac point is buried under the bulk valence band maximum.

The second part of this thesis focuses on magnetic doping at the sample surface. This surface doping is achieved by two separate atomic depositions of cobalt and chromium. After each deposition, new features arise at the surface, which are studied by means of STM and STS. They can be divided into two categories. The first category of features is believed to consist of atoms and small clusters of cobalt or chromium at the surface. The second category might be explained by single-atom substitution of bismuth atoms in the second atomic layer by cobalt or chromium atoms, but this hypothesis can only be verified or disproven by ab initio calculations. Scattering events at the surface after the depositions are studied by means of STS. It is plausible that time reversal symmetry is broken and backscattering is no longer prohibited. The dispersion of the surface states

after the depositions remains linear. A shift in the Dirac energy point indicates that the deposited atoms introduce some doping effect, but do not act to bring the Dirac point out of the valence band.

The experimental results presented in this thesis are a starting point for the understanding of the interaction between 3D TI surfaces and magnetic surface dopants. The interaction can be modified by changing either the surface properties or the magnetic impurity properties. For this reason, it is interesting to repeat the experiments performed in this work with another Bi_2Te_3 sample grown under different conditions or to vary the deposited amount of atoms. One might also gain better understanding by depositing atoms of magnetic elements other than cobalt or chromium. Depositing clusters instead of atoms is a promising approach as well. A next step could consist of investigating the magnetic properties of the deposited magnetic impurities.

Summary in layman's terms

Topological insulators are materials which are insulating everywhere except at their boundaries. They exist in two dimensions, where only the edges are conducting, and in three dimensions, where their whole surface is. The difference with regular insulators is expressed using a mathematical entity known as a topological invariant, hence the name *topological* insulator. The conducting boundaries of these materials are special: in normal metals electrons can scatter back from impurities or imperfections, leading to dissipation in the current. In the conducting boundary of topological insulators however, the movement of the electrons are coupled to a property known as spin. This means that when an electron collides with an impurity, it cannot go back to the direction it came from unless the spin of the electron is flipped by the impurity: backscattering is not allowed and so the current is dissipationless. The first part of this thesis investigates the surface of bismuth telluride (Bi_2Te_3), a three dimensional topological insulator. First, native defects of the crystal are studied and identified. This is interesting because defects in the crystal can result in doping, which plays an important role when applications are considered. After that, the scattering occurring at the surface is studied. The findings confirm that backscattering is prohibited, at least for some energies.

If the electrons at the boundary encounter something that can flip their spin, it is expected that the electron movement can also be altered and backscattering is no longer suppressed. To see this backscattering, atoms of magnetic materials are deposited on the Bi_2Te_3 surface. This is done two times in this work: once with cobalt atoms, and once with chromium atoms. In both cases, several new features arise on the surface, which can be divided into two categories. The first category of features consists of atoms and small groups of atoms on the surface. The second group of features might be explained as deposited atoms sinking into lower layers of the crystal, but this cannot be stated with certainty from the experimental work alone. After both depositions, the scattering occurring at the surface is examined and it is plausible that backscattering is indeed present. This is of interest because the combination of topological insulators with magnetic impurities is expected to yield interesting quantum phenomena.

List of abbreviations and symbols

Abbreviations

2D	two dimensional
3D	three dimensional
AES	Auger electron spectroscopy
ARPES	angle resolved photoemission spectroscopy
BCB	bulk conduction band
BVB	bulk valence band
BZ	Brillouin zone
CEC	constant energy contour
CITS	current imaging tunneling spectroscopy
DC	direct current
DFT	density functional theory
DOS	density of states
IMBL	ion and molecular beam laboratory
LDOS	local density of states
LEED	low-energy electron diffraction
QAHE	quantum anomalous Hall effect
QHE	quantum Hall effect
QL	quintiple layer
QPI	quasiparticle interference
QSHE	quantum spin Hall effect
STM	scanning tunneling microscopy
STS	scanning tunneling spectroscopy

TI	topological insulator
UHV	ultra high vacuum

Symbols

$\bar{\Gamma}$	high-symmetry point in the surface Brillouin zone
$\bar{\mathrm{K}}$	high-symmetry point in the surface Brillouin zone
$\bar{\mathrm{M}}$	high-symmetry point in the surface Brillouin zone
$\gamma_n[C]$	Berry phase acquired over a path C
$\mathbf{A}_n(\mathbf{R})$	Berry connection
$\mathbf{B}_n(\mathbf{R})$	Berry curvature
ν	Chern number
ω_c	cyclotron frequency
ϕ	work function
ψ	electron wavefunction
$\psi_\mu(\vec{k})$	Bloch eigenstate
ρ_s	local density of state of the sample surface
ρ_t	local density of state of the STM tip
σ_{xy}	Hall conductivity
$\mathrm{d}I/\mathrm{d}V$	tunneling conductance
$\vec{B}$	magnetic field
$\vec{E}$	electric field
$\vec{k}$	crystal momentum
$\vec{p}$	linear momentum
$\vec{q}$	scattering wavevector
$\vec{v}$	velocity
c	speed of light $299792458\ \mathrm{m/s}$
e	elementary charge $1.60218 \times 10^{-19}\ \mathrm{C}$
$E_\mu(\vec{k})$	Bloch eigenvalue
E_D	Dirac point energy

E_F	Fermi level energy	
$f(E)$	Fermi-Dirac distribution evaluated at an energy E	
g	genus	
H	Hamiltonian	
h	Plank's constant, equal to $2\pi\hbar$	6.62607×10^{-34} Js
I	tunneling current	
l_0	decay length for wave functions into a vacuum barrier	
N	TKKN invariant (Thouless, Kohmoto, Nightingale, de Nijs)	
$T(E, V, d)$	transmission coefficient	
V	bias voltage	
v_F	massless fermion group velocity	
Ag	silver	
Ar	argon	
Au	gold	
Bi_2Se_3	bismuth selenide	
Bi_2Te_3	bismuth telluride	
Co	cobalt	
Cr	chromium	
Fe	iron	
H	hydrogen	
He	helium	
HgTe	mercury telluride	
M	manganese	
Sb_2Te_3	antimony telluride	
V	vanadium	
W	tungsten	

Contents

Introduction

Topological insulators (TIs) are a new class of insulators with exotic properties, which exist in both 2D and 3D. Their bulk is insulating, but their boundaries host metallic states. These boundary states are due to a band inversion because of large spin orbit coupling. Moreover, the conducting states are protected by time reversal symmetry, leading to them being robust against nonmagnetic backscattering. Due to their intriguing properties, TIs have attracted much attention in the scientific community. They are interesting from both a fundamental and a practical point of view: it is a novel state of matter to be explored, but TIs are also promising materials for applications in spintronics and computational devices [1–4]. Spectroscopy measurements have shown that for 3D TIs the 2D energy-momentum relation forms a Dirac cone structure. One of these 3D TIs is bismuth telluride (Bi_2Te_3). It is among the most promising candidates for room temperature spintronics and quantum computational devices.

Furthermore, the topological boundary states may host exotic quantum phenomena like the quantum anomalous Hall effect (QAHE) when time reversal symmetry is broken [1]. In order to realize these phenomena experimentally, one needs intrinsic TIs. This means that the Fermi level should be inside the band gap so that the Dirac surface states dominate the transport phenomena. However, several TIs (including Bi_2Te_3) are always degenerately doped due to naturally occurring crystalline defects, which causes their transport properties to be heavily affected by bulk carriers [5]. A lot of effort has been put into suppressing this bulk conduction through various methods like nanostructuring, compensation by chemical doping or electric gating and band structure engineering by alloying or realizing p-n junctions [6–10]. The problem with these methods is that they either introduce additional disorder or potential fluctuations which negatively affect the TI surface state mobility [11]. Clear identification and understanding of native defects is thus an essential step in TI research.

To break time reversal symmetry, great efforts have been made in the magnetic doping of bulk TI materials. An opening of the energy gap at the Dirac point due to the broken time reversal symmetry has been directly observed in magnetically doped 3D TIs [12, 13]. Moreover, ferromagnetism has been achieved in 3D TIs through bulk doping: it has been found in V-, Cr- and Mn-doped single crystals of Sb_2Te_3 [14–18] and Fe- and Mn-doped single crystals of Bi_2Te_3 [18–20]. The QAHE was realized in a thin film of Bi_2Se_3 through chromium bulk doping [21]. Magnetic doping at the surface, which can be realized by the deposition of magnetic atoms, has however not been explored as thoroughly. It is particularly interesting to do so since it is expected to stronger influence the surface Dirac fermions than bulk doping [22]. Experimental studies of the interaction of surface mag-

netic moments with topological states have predominantly been performed using spatially averaging techniques [23–26]. While these techniques provide important contributions towards the understanding of the interaction of magnetic moments with topological states, they cannot probe local phenomena [27]. An investigation using local techniques like scanning tunneling microscopy is thus needed.

The first part of this work aims to characterize the Bi_2Te_3 surface and identify its native defects. This is done by using several techniques: low temperature ultra high vacuum scanning tunneling microscopy and spectroscopy (STM and STS) are the most important ones. Additional surface analysis is done through Auger electron spectroscopy (AES) and low-energy electron diffraction (LEED). Scattering events occurring at the surface are also examined by means of STS, to understand whether backscattering occurs. In the second part of this thesis, magnetic doping at the Bi_2Te_3 surface is studied. This is done by an examination of the surface by means of STM and STS after atomic deposition of the magnetic materials cobalt and chromium. To establish whether time reversal symmetry indeed gets broken, the scattering events at the surface are investigated.

Chapter overview

Chapter 1 gives an introduction to TIs. By introducing the concept of topological band theory, the difference between an ordinary insulator and a topological insulator is discussed. Using this concept, 2D TIs are described. A generalization to 3D TIs is made and the 3D TI bismuth telluride (Bi_2Te_3) is elaborated upon. The last part of the chapter focuses on the research aims of this thesis.

In chapter 2, the experimental techniques used in this work are discussed. The most important ones are scanning tunneling microscopy and spectroscopy (STM and STS). Auger electron spectroscopy (AES) and low-energy electron diffraction (LEED) are considered as well.

Chapter 3 presents work on the characterization of a Bi_2Te_3 crystal. STM and STS measurements are used to identify native defects of the crystal, as well as scattering events occurring at the sample surface. Further surface analysis is done using AES and LEED.

The aim of chapter 4 is to study the Bi_2Te_3 surface after cobalt is deposited on it. After depositing cobalt atoms at room temperature, the sample surface is studied using STM and STS. Both native defects and new features are studied. Scattering events at the surface are also looked at.

The focus of chapter 5 is examining the Bi_2Te_3 surface after atomic chromium deposition. As in the previous chapters, this is done by means of STM and STS. Native defects of the crystal and newly arising features are studied. The chapter ends with an investigation of the scattering events occurring at the surface.

The thesis ends with chapter 6, in which a summary of the findings is presented. Suggestions for further research are also discussed there.

Chapter 1

Topological insulators

Topological insulators (TIs) are materials or compounds which host a new electronic phase stemming from the topological character of their bulk wave functions. Unlike most other electronic states of matter, topological insulating phases were first proposed theoretically and then observed experimentally, although they can be found in common semiconductors and thermoelectric materials [4]. These electronic phases can be understood within the band theory of solids. In this framework, a band inversion due to a large spin-orbit interaction leads to insulating states in the bulk but conducting ones at the boundaries. These boundary states are quite exotic: they are protected by time reversal symmetry and the carriers at these states arrange in such a way that there is spin-momentum coupling. This means that the direction of the spin determines in which direction the carriers travel, making the states robust against nonmagnetic backscattering. These materials and their properties have interested the scientific community. This is because this novel state of matter is interesting from a fundamental point of view, while it also has potential in applications such as spintronic and quantum computing devices [1–3].

The first section 1.1 of this chapter introduces the concept of topological band theory and describes an important electronic state known as the quantum Hall state. Section 1.2 describes 2D TIs and section 1.3 extends the concepts from two to three dimensions. The last section 1.4 formulates the research aims of this thesis.

1.1 Topological band theory

In this part, a brief introduction into topological band theory can be found. This is done by looking at the insulating state (see subsection 1.1.1). As an example, the topological order in the quantum Hall state is studied (in subsection 1.1.2), along with the edge states associated with it (subsection 1.1.3).

1.1.1 The insulating state

In the 20^{th} century, one of the great successes of quantum mechanics was the successful description of electronic states using the newly developed band theory of solids [28]. Using this description, there is little difference between an insulator and a semiconductor: both show a gap between the valence and conduction band (even though the gap is much larger for an atomic insulator than for a semiconductor). One could deform the energy

bands from an insulator to a semiconductor (or the other way around) without closing the energy gap. The fact that this is possible, defines a topological equivalence between these different insulating states. Taking this classification scheme, all conventional insulators are equivalent. Moreover, they are equivalent to the vacuum: according to Dirac's relativistic quantum theory, the vacuum also has a conduction band (for electrons), a valence band (for positrons) and an energy gap (for pair production) in between [29].

One could wonder whether all electronic states with an energy gap are topologically equivalent to the vacuum. The answer is no. In fact, the counterexamples are very interesting states of matter [30]. The most famous counterexample is the integer quantum Hall state.

1.1.2 Integer quantum Hall state

To understand the states associated with the quantum Hall effect, an understanding of the classical Hall effect (illustrated in figure 1.1) is needed.

Consider a two dimensional electron gas in a perpendicular magnetic field. When a magnetic field $\vec{B} = (0, 0, B_z)$ is applied perpendicularly to a current I_x in the x-direction, the charge carriers are subjected to the Lorentz force $\vec{F} = q\vec{v} \times \vec{B}$ and their trajectories are deflected [31]. The Lorentz force is dependent on the velocity $\vec{v}$ of the charge carriers, which means that electrons moving in opposite directions will be deflected to opposing edges. This way, charges are accumulated at the edges and an electric field in the y-direction is built up. This field E_y exactly cancels the y-component of the Lorentz force on the carriers.

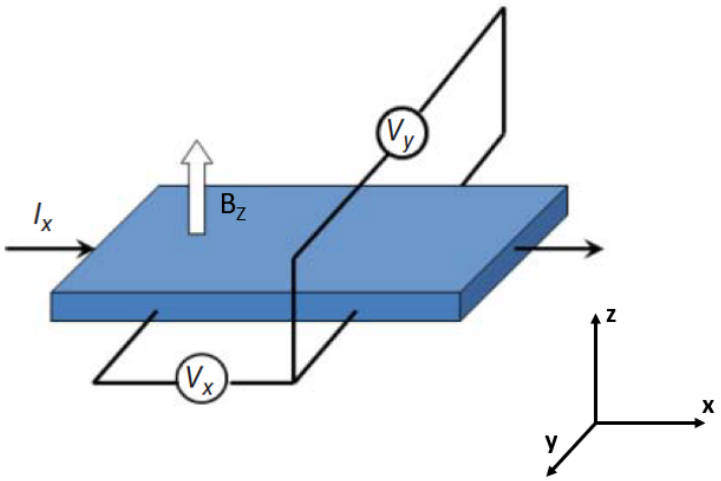

Figure 1.1: Geometry for the Hall effect experiment. Figure adapted from [1].

In 1980, Klaus von Klitzing observed that when electrons confined to two dimensions are placed in a strong magnetic field, the Hall conductivity σ_{xy} (the ratio of the electrical current to the voltage perpendicular to the current flow) becomes quantized [32]. It can only take values that are integers of e^2/h, which severely restricts the motion of the charge carriers. This quantization of σ_{xy} is known as the quantum Hall effect and has

been measured to 1 part in 10^9 [33]. An intuitive way to understand this is the following: because of the strong external magnetic field, the electrons are driven to move in circular orbits with a cyclotron frequency ω_c. Due to the quantum mechanical effects at low temperatures, the orbits are described by orbitals with quantized energy levels. These levels are also known as Landau levels and have energies $E_\mu = \hbar\omega_c\,(\mu + 1/2)$. When N of these Landau levels are filled and the rest are empty, there is an energy gap separating the filled and empty states, just as for a classical insulator. A comparison between the ordinary insulating state and the quantum Hall state and their band structure is shown in figure 1.2. What makes the quantum Hall state different from an atomic insulator is that an electric field can cause the cyclotron orbits to drift at the edges. These drifting orbits lead to a Hall current which is characterized by the quantized Hall conductivity [34].

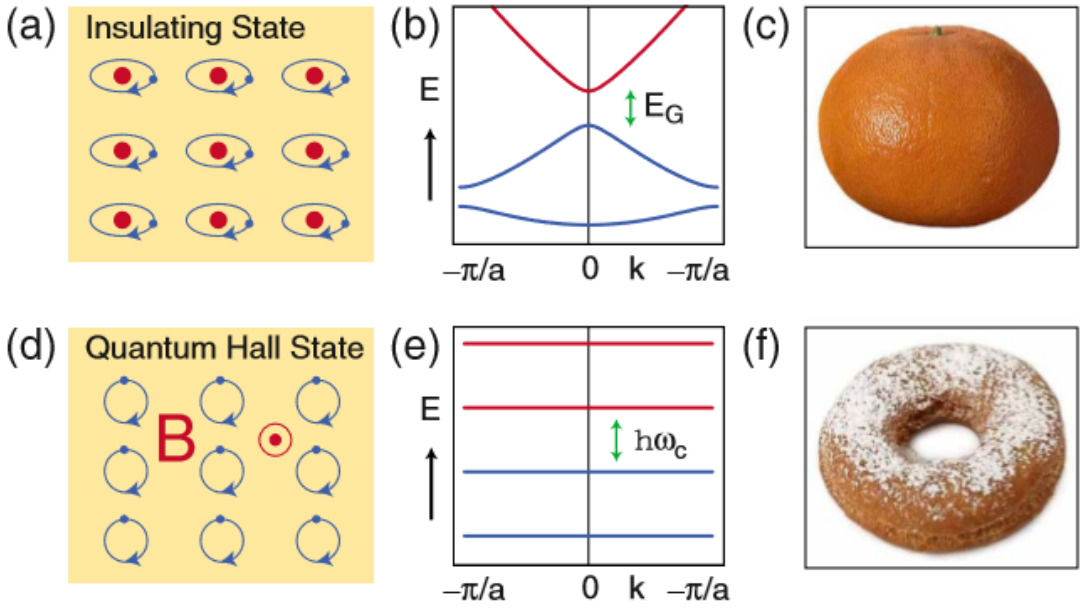

Figure 1.2: States of matter. (a)-(c) The insulating state. (a) An atomic insulator. (b) A simple model insulating band structure. (d)-(f) The quantum Hall state. (d) The cyclotron motion of electrons. (e) The Landau levels, which may be viewed as a band structure. (c) and (f) Two surfaces which differ in their genus, g. (c) $g = 0$ for the sphere and (f) $g = 1$ for the donut. The Chern number ν that distinguishes the two states is a topological invariant similar to the genus. Image taken from [30].

How is this difference between the quantum Hall state and the trivial insulating state classified? To answer this question, one must look at the field of topology. A band structure plot is in essence a mapping from the crystal momentum $\vec{k}$ to the Bloch Hamiltonian $H(\vec{k})$. It turns out that some mappings to different gapped band structures are equivalent: if one band structure can be deformed into another one without closing the energy gap, they belong to the same equivalence class. These different equivalence classes are distinguished from each other by means of an integer number ν. This number is a so-called topological invariant and is known as the Chern number [35]. It is a topological invariant in the sense that it cannot change when the Hamiltonian varies smoothly. This helps to explain the robust quantization of σ_{xy} [36].

To understand this notion of a topological invariant, one can compare the band structure mapping to simpler mappings. Take a map from two to three dimensions: this map describes surfaces. Two-dimensional surfaces can be classified by their genus g. This genus counts the number of holes: a sphere (figure 1.2(c)) has $g = 0$ while a donut (figure 1.2(d)) has $g = 1$. According to a mathematical theorem due to Gauss and Bonnet [37], the integral of the curvature over a closed surface is a quantized topological invariant, whose value is related to g. The Chern number ν is proportional to an integral of a related curvature, called the Berry curvature of the energy band over the boundary of the Brillouin zone [36]. This is zero for a usual energy band but unity for a Landau level. The Hall conductance $\sigma_{xy} = Ne^2/h$ is the sum of the Chern numbers of all the occupied bands in the unit of e^2/h [38]. A more thorough review can be found in the appendix, see also [36, 39].

1.1.3 Edge states

Gapped band structures are thus topologically classified. A fundamental consequence of this classification is the existence of gapless conducting interface states at interfaces where the topological invariant changes [30]. As an example, one can take the edge between the integer quantum Hall state (with Chern number $\nu = 1$) and a trivial insulator ($\nu = 0$). In the integer quantum Hall state, the electrons move in cyclotron orbits as discussed before. At the edge however, it is no longer possible for the electron to complete a full orbit: the electron orbits just bounce off the edge. These skipping orbits at the edge lead to perfect conduction along the edge (see figure 1.3). The electronic states responsible for this motion are chiral: they propagate in one direction only. Normally, when electrons encounter impurities they scatter back, but given that there are no backward-moving modes available, the electrons can only continue their trajectory forwards. So these surface states are robust, even in the presence of impurities [40].

The fact that these chiral edge states exist is related to the topology of the bulk quantum Hall state. One can imagine a crystal that has an interface that passes from the quantum Hall state to the trivial insulating state. Somewhere along the way, the energy gap should disappear - it is impossible for the topological invariant to change otherwise. Since the energy gap must close at some point, there will be low energy electronic states bound to the region where the energy gap passes through zero [30].

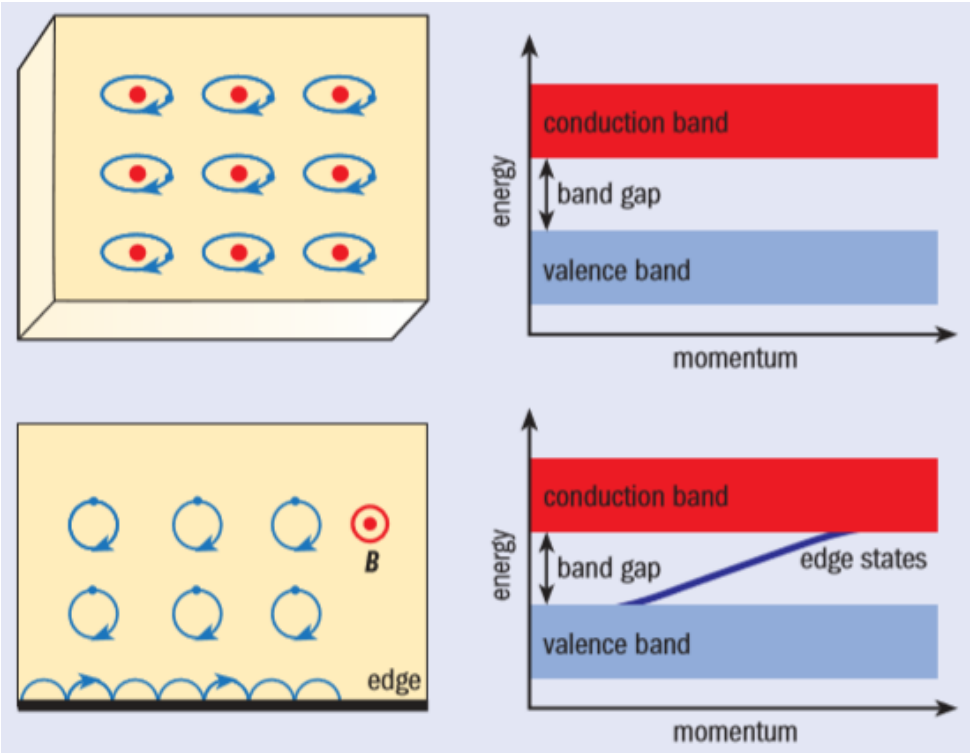

Figure 1.3: (top) An atomic insulator, in which the occupied and empty electronic states are separated by an energy gap due to the quantization of the energy of atomic orbitals. (bottom) In the quantum Hall effect, the circular motion of electrons in a magnetic field is interrupted by the sample boundary. At the edge, electrons execute skipping orbits as shown, ultimately leading to perfect conduction in one direction along the edge. This leads to conducting states at the edges, as seen in the energy diagram. Image taken from [40].

1.2 2D topological insulators

The quantum Hall edge states discussed in the previous section are interesting because of their protection against disorder and backscattering. They are however not the edge states of a TI. This is because in TIs, the boundary states are protected by time reversal symmetry, which is broken by the magnetic field applied to achieve the quantum Hall effect. This time reversal symmetry is the subject of subsection 1.2.1. An analogous phenomenon that does not break time reversal symmetry is the quantum *spin* Hall state. The states associated with this effect are 2D TI states and are discussed in subsection 1.2.2.

1.2.1 Time reversal symmetry

Time reversal symmetry is the symmetry of physical laws under the time reversal transformation:

$$T : t \mapsto -t. \tag{1.1}$$

This transformation plays an important role in the behaviour of TIs. When a system exhibits time reversal symmetry, its Hamiltonian H commutes with the time reversal operator T:

$$[H, T] = 0 \quad \text{or} \quad H(t) = H(-t). \tag{1.2}$$

The behaviour of physical systems depends on whether these systems are odd or even under time reversal symmetry, meaning $H(-t) \neq H(t)$ or $H(-t) = H(t)$ respectively. In systems where a magnetic field $\vec{B}$ field is applied to electrons, the electron trajectories are bent. By reversing the time direction, the system Hamiltonian is changed and the electrons will not retrace their motion: the applied magnetic field is odd under time reversal symmetry [41].

In TIs, the boundary states are protected by time reversal symmetry. Since a magnetic field is needed to induce the quantum Hall edge states, time reversal symmetry is broken and the quantum Hall state cannot be a TI state. There is however a very similar electronic state that is: the quantum spin Hall state. The 2D TI is indeed also known as a quantum spin Hall insulator.

1.2.2 Quantum spin Hall state

In order to see the quantum Hall effect and the states associated with it, a large magnetic field is needed, which will result in the breaking of time reversal symmetry. An analogous phenomenon that does not break this symmetry is the quantum spin Hall effect [42]. It is equivalent to the quantum Hall effect, but the cyclotron orbits are driven by spin-orbit coupling rather than an external magnetic field. This spin-orbit coupling is the interaction of an electron's intrinsic angular momentum, or spin, with the orbital motion of the electrons through space as shown in figure 1.4. When an electron orbits around a nucleus, one could say a magnetic field is generated by its movement. One could also look at what is happening from the electron viewpoint: the electron feels an effective magnetic field due to the movement of the nucleus. This effective field is $\vec{B}_{\text{eff}} = -\frac{\vec{p}\times\vec{E}}{mc^2}$, where $\vec{p}$ is the electron momentum, $\vec{E}$ is the electrostatic field the electron experiences due to the nucleus, m is the electron mass and c is the speed of light. This effective magnetic field is larger for heavier nuclei since the size of the electric field E is proportional to the atomic number Z.

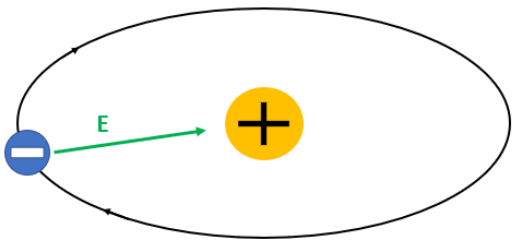

Figure 1.4: Schematic representation of an electron (blue) orbiting a nucleus (yellow). The electric field of the nucleus is indicated by the green arrow.

It is clear that the spin-orbit interaction is proportional to the orbital motion of the

electron, which is represented by the vector product of the electron momentum $\vec{p}$ and this electrostatic field $\vec{E}$. Of course, the spin-orbit interaction is also dependent on the electron spin $\vec{S}$, leading to the Hamiltonian

$$H_{SO} = \lambda_{SO} \vec{B}_{\text{eff}} \cdot \vec{S}, \tag{1.3}$$

where λ_{SO} is a parameter expressing the strength of the spin-orbit interaction [43, 44].

This effective magnetic field B_{eff} of the spin-orbit interaction is similar to the external magnetic field, but there is an important difference: the Hamiltonian of the system with spin-orbit coupling is even under time reversal symmetry. The alignment of the spin to the magnetic field B_{eff} generated in this way makes the scattering spin-dependent: because the orbital motion and the spin are coupled, the direction in which electrons leave a scattering center is spin-dependent. It is also possible to reverse this: the spin of the electrons determines the direction in which they move throughout the material. In the bulk, this does not lead to conducting states because atoms in the bulk also have magnetic moments and can thus change the spin of the electron. This way the electron can move in all possible directions, resulting in no net movement and so no conduction. At the edge however, the electrons are only influenced by the atoms on one side. This leads to electron movement and so to conduction. It should be noted that only a very specific spin-filtered kind of movement is allowed: spin up states propagate in one direction while spin down states propagate in the other. As illustrated in figure 1.5, the quantum spin Hall edge channels can be seen as two quantum Hall edge channels; one with spin up states and the other with spin down states. A system that exhibits a spin current like this is also called helical [45].

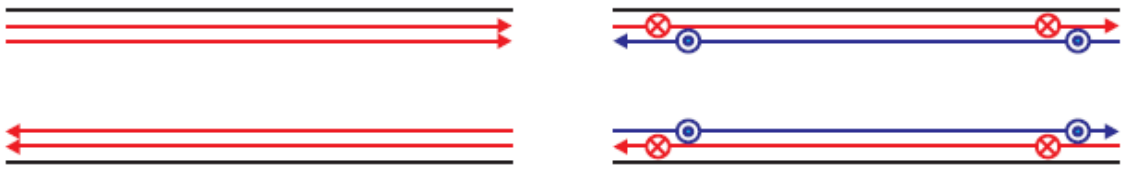

Figure 1.5: Edge channels for (left) the quantum Hall effect and (right) the quantum spin Hall effect. In the regime of the quantum Hall effect, chiral edge states move in one direction ($B \neq 0$). In the quantum spin Hall regime, a pair of counterpropagating edge states exists at one edge. The two edge states move in different directions with opposite spin polarization ($B = 0$). Image taken from [1].

These quantum spin Hall edge states form a 1D conductor which can be seen as half of a quantum wire which would have spin up and spin down electrons propagating in both directions. Ordinary conductors that have both spins propagating in both directions are fragile: the electronic states can be localized in the presence of weak disorder [46, 47]. The quantum spin Hall edge states on the contrary cannot be localized even for strong disorder, and hence are protected from backscattering - if the scattering defects are nonmagnetic and the electron's spin is preserved in the scattering event. The fact that the edge states propagate in two directions instead of one (as shown in figure 1.6) makes the origin of this protection a bit more complicated.

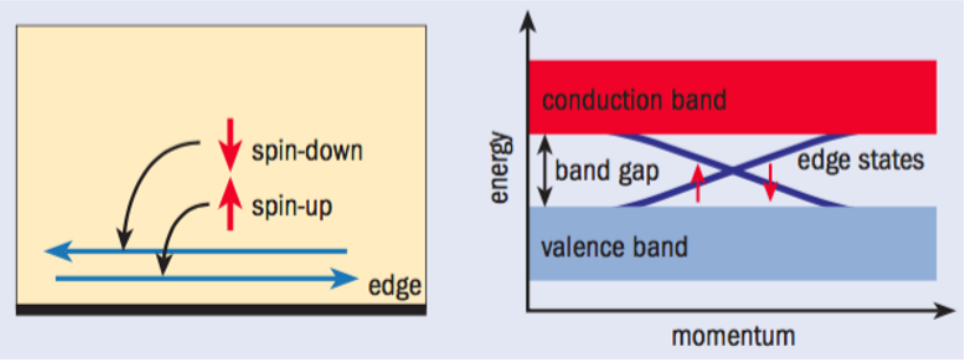

Figure 1.6: The edge of the quantum spin Hall effect state or 2D TI contains left-moving and right-moving modes that have opposite spin and are related by time-reversal symmetry. Image taken from [40].

Imagine an edge that is disordered within some finite region while it is perfectly ordered outside of that region. By relating the incoming waves to those reflected from and transmitted through the disordered region, the edge states can be determined. In 2005, Kane and Mele showed that the reflection amplitude is odd under time reversal symmetry since it requires changing the propagation direction and hence flipping the spin. This can be seen as just interchanging two counter-propagating nodes. Because of this, an incident electron is transmitted perfectly across the disordered region unless time reversal symmetry is broken [42]. Of course, this explanation only makes sense if the edge states occur in pairs. In fact, there is a theorem known as Kramers theorem that states that the edge pairs should occur in pairs in order not to break time reversal symmetry [48]. In the presence of spin-orbit interaction, the energy bands split and become degenerate. However, if there are edge states, they must remain degenerate at certain time reversal invariant points Γ_a and Γ_b in the Brillouin zone known as Kramers degenerate points, as shown in figure 1.7. There are two different ways in which the states in Γ_a and those in Γ_b can be connected.

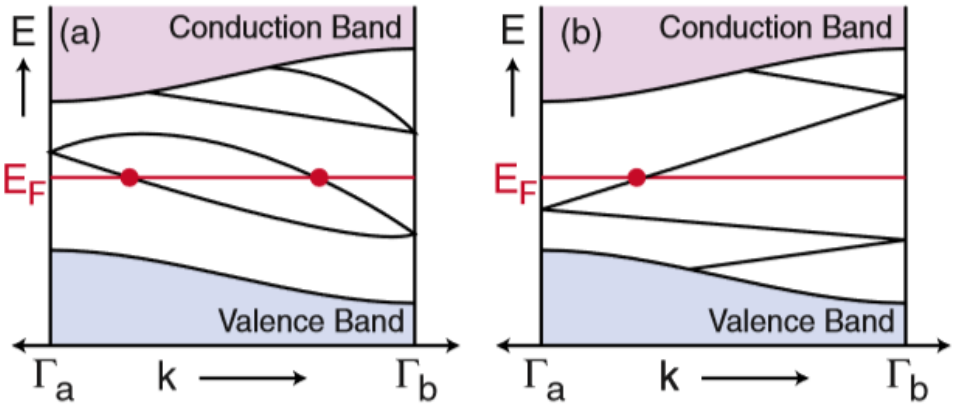

Figure 1.7: Electronic band diagram between two time reversal invariant points Γ_a and Γ_b. In (a) the number of edge states crossing through the Fermi energy E_F is even, while in (b) it is odd. Image taken from [30].

As shown in figure 1.7(a), they can connect pairwise. In this case the edge states can be eliminated by pushing all of the bound states out of the gap. An even number of band crossings at the Fermi energy E_F thus leads to a system behaving as a classical insulator. It is also possible to have an odd number of such crossings, as shown in figure 1.7(b). In this case, the conducting edge states cannot be pushed out of the gap. They are topologically protected. The possible outcome of these two alternatives depends on a bulk topological invariant known as a $\mathbb{Z}_2$ invariant [30].

So in order to be a TI, the number of pairs of edge states should be odd. This results in edge states that are topologically robust and protected against nonmagnetic backscattering of the electrons on the edge. The quantum spin Hall system satisfies this condition and thus is a 2D TI.

1.3 3D topological insulators

In this section, 3D TIs are discussed. In subsection 1.3.1, the generalization of the quantum spin Hall state to three dimensions is explained. The experimental verification of this 3D TI state is discussed in subsection 1.3.2 and subsection 1.3.3 introduces bismuth telluride, the 3D TI studied in this work.

1.3.1 Generalization of the quantum spin Hall state to three dimensions

The quantum spin Hall state, characterizing a 2D TI, has a natural generalization in three dimensions. This was independently discovered by three theoretical groups: Fu, Kane and Mele [49], Moore and Balents [50] and Roy [51]. In quantum spin Hall insulators, the topological order of the bulk is connected to the presence of unique conducting *edge states*. For 3D TIs, this bulk topological order is related to conducting *surface states*. These surface states support electronic motion in any direction along the surface, but present spin-orbit coupling again: the direction of the electron's motion is determined by its spin direction and vice versa. There is thus no spin-degeneracy for the 2D surface as in normal metals: states at momenta $\vec{k}$ and $-\vec{k}$ must have opposite spin and so the spin must rotate with $\vec{k}$ around the Fermi surface. However, analogously to the 2D TI, there are time reversal invariant points $\Gamma_{a,b,c,d}$ in the surface Brillouin zone where surface states - if present - must remain Kramers degenerate. Because of this, these Kramers degenerate points form 2D Dirac points in the surface band structure, as shown in figure 1.8. This structure helps explain why nonmagnetic backscattering is prohibited: in a backscattering process, the electron's momentum is flipped from $\vec{k}$ to $-\vec{k}$. If the scattering process is caused by a nonmagnetic defect, the spin of the electron should remain the same. In an ordinary metal, an electron can scatter into a state with momentum $-\vec{k}$ and the required spin. In the 2D surface of a 3D TI however, the only spin state available at $-\vec{k}$ is exactly opposite to the required one. Because of this, backscattering due to nonmagnetic impurities is not possible.

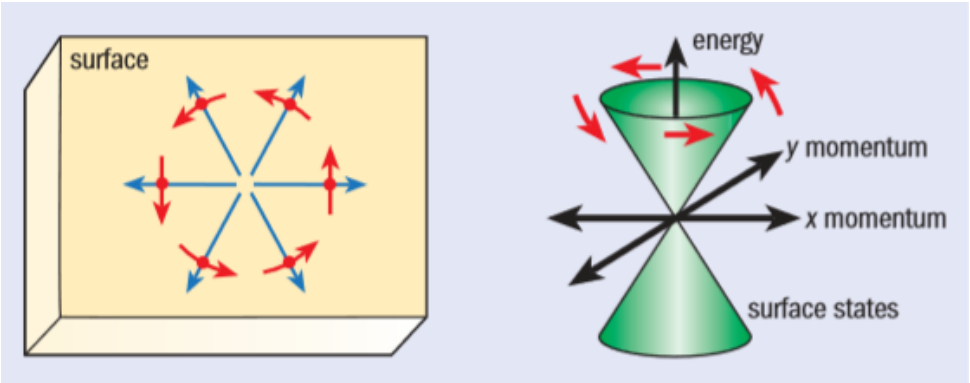

Figure 1.8: The surface of a 3D TI supports electronic motion in any direction along the surface, but the direction of the electrons motion uniquely determines its spin direction and vice versa. The 2D energy-momentum relation has a Dirac cone structure which is similar to that in graphene but is spin-split except for certain symmetry points. Image taken from [40].

Whether the material is an ordinary or a topological insulator then depends on how the Dirac points at the different time reversal invariant points connect to each other. As in the 2D case, the surface state structure between any pair Γ_i and Γ_j determines whether the Fermi surface intersects a line joining Γ_i to Γ_j an even or an odd number of times. If it is odd, then the surface states are topologically protected against nonmagnetic backscattering. Which of these alternatives occurs is determined by four $\mathbb{Z}_2$ topological invariants of the bulk [40].

1.3.2 Experimental verification

The 3D TI was predicted to exist in several real materials, such as $Bi_{1-x}Sb_x$, as well as strained HgTe and α-Sn [52]. In 2009, $Bi_{1-x}Sb_x$ became the first experimentally verified 3D TI. A Princeton University group led by Hasan realized this by mapping the semiconducting alloy's surface bands using angle resolved photoemission spectroscopy (ARPES) [53]. The ARPES technique is based on the photoelectric effect: a monochromatic beam of light (typically from a synchrotron radiation source) is incident on a sample and through photoexcitation, electrons are excited into the vacuum. Afterwards, these photoelectrons are collected in an analyzer, where their kinetic energy is measured as a function of their emission angle relative to the sample surface. Provided the energy of the incident beam is known, one can relate the measured kinetic energy of the photoelectrons to their in-plane crystal momentum by using energy-momentum conservation. One can thus visualize the energy band structure. If the photoemission process is spin-conserving, the spin of the initial state of an electrion in a solid can be determined as well by measuring its spin after photoemission [54].

Soon after this first discovery, so called second-generation 3D TIs, including Bi_2Se_3 and Bi_2Te_3 were identified experimentally. This second-generation 3D TIs has interesting properties such as relatively large bulk gaps (up to 0.3 eV in Bi_2Se_3) and simple surface Dirac cone structures [8, 55–57]. In figure 1.9, ARPES mappings of surface states of the doped TI $Bi_{2-\delta}Ca_\delta Se_3$ are shown. The 2D Dirac cone structure is clearly observed.

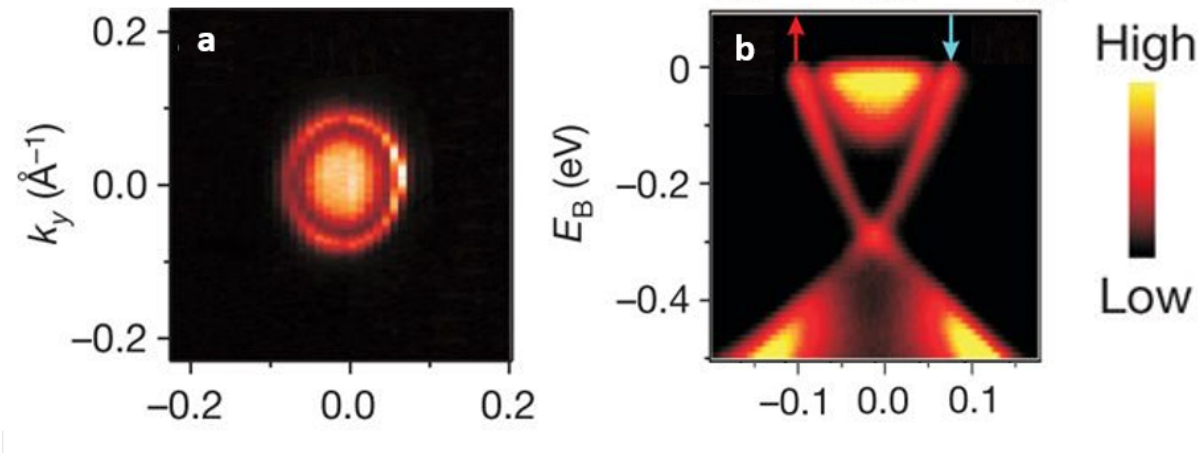

Figure 1.9: (a) A high resolution ARPES mapping of the topological surface Fermi surface near the $\overline{\Gamma}$-symmetry point of the (111)-surface of $Bi_{2-\delta}Ca_\delta Se_3$. (b) High resolution ARPES surface band dispersions through the $\overline{\Gamma}$-symmetry point. The arrows denote the topological spin polarization of the bands. The intensity scale is shown on the right. Image adapted from [8].

The band structure and the absence of backscattering have also been reported with scanning tunneling microscopy (STM) and spectroscopy (STS): more about this in section 2.1.3. STM and ARPES are complementary to each other since they offer high spatial and momentum resolution information on the electronic structure, respectively. In conventional ARPES, only filled-state electrons can be photoemitted, while both filled and empty states can be probed in STM. There are few experimental studies on 3D TIs that have been done with other techniques than ARPES or STM. This is because challenges posed due to native defects in the bulk of the TIs. These defects act as charge dopants and move the Fermi level out of the band gap. A such, chemical dopants are used to shift the Fermi level into the band gap, where the surface states of interest reside [58, 59]. It is also necessary to suppress bulk related effects (such as the remaining bulk conductivity induced by impurities) by increasing the surface-to-volume ratio [60].

1.3.3 Bismuth telluride

Before being discovered as a 3D TI, bismuth telluride (Bi_2Te_3) had already been thoroughly investigated due to its excellent thermoelectric properties [4]. It became even more interesting to the scientific community after its discovery as a 3D TI and is among the most promising candidates for room temperature spintronics and quantum computational devices [8, 57].

Bi_2Te_3 crystals have a rhombohedral structure: the crystal structure belongs to the space group $D^5_{3d}(R\overline{3}m)$, while the point group contains a binary axis (with twofold rotation symmetry), a bisectrix axis (appearing in the reflection plane), and a trigonal axis (with threefold rotation symmetry). In figure 1.10, the Brillouin zone of Bi_2Te_3 is shown. It has four inequivalent time-reversal-invariant points, called $\Gamma(0,0,0)$, $L(\pi,0,0)$, $F(\pi,\pi,0)$ and $Z(\pi,\pi,\pi)$. The blue hexagon shows the 2D Brillouin zone of the projected (111) surface, in which the high-symmetry $\vec{k}$ points $\bar{\Gamma}$, $\bar{K}$ and $\bar{M}$ are labelled.

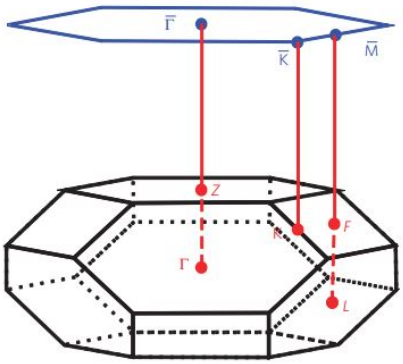

Figure 1.10: Brillouin zone for Bi_2Te_3 with space group ($R\bar{3}m$. . The four inequivalent time-reversal-invariant points are $\Gamma(0,0,0)$, $L(\pi,0,0)$, $F(\pi,\pi,0)$ and $Z(\pi,\pi,\pi)$. The blue hexagon shows the 2D Brillouin zone of the projected (111) surface in which the high-symmetry $\vec{k}$ points $\bar{\Gamma}$, $\bar{\mathrm{K}}$ and $\bar{\mathrm{M}}$ are labelled. Image taken from [2].

There are five atoms per unit cell, which is presented in figure 1.11. This unit cell is hexagonal with lattice parameters $a = b = 4.3835$Å, $c = 30.487$Å, and angle $\gamma = 120°$ [61]. Units of Te1-Bi-Te2-Bi-Te1 form quintuple layers (QLs) along the z-direction. Bonding between atomic planes within a QL is of covalent and ionic origin while bonding between adjacent QLs is predominantly of the van der Waals type. Due to this weak bonding between QLs, the crystal is easily cleaved along an inter-QL plane. The bulk structure consists of alternating hexagonal monoatomic crystal planes stacking in ABC order [61,62].

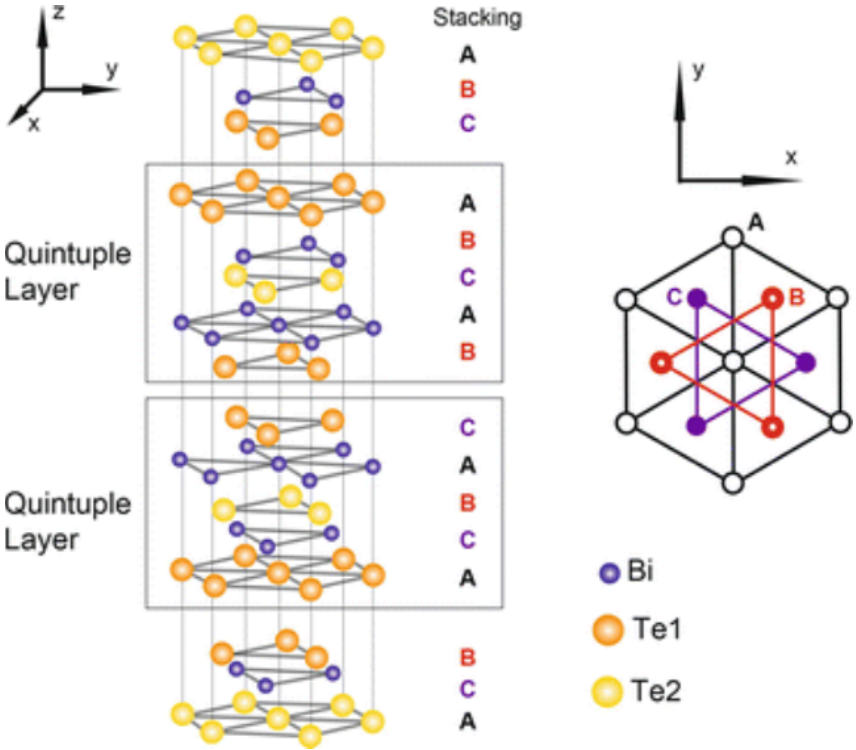

Figure 1.11: Crystal structure of Bi_2Te_3. Hexagonal unit cell of the crystal comprised of three QLs and belonging to the space group $R\bar{3}m$. The Te2 layer within each QL is a center of inversion symmetry. Image taken from [62].

The electronic structure of Bi_2Te_3 is shown in figure 1.12.

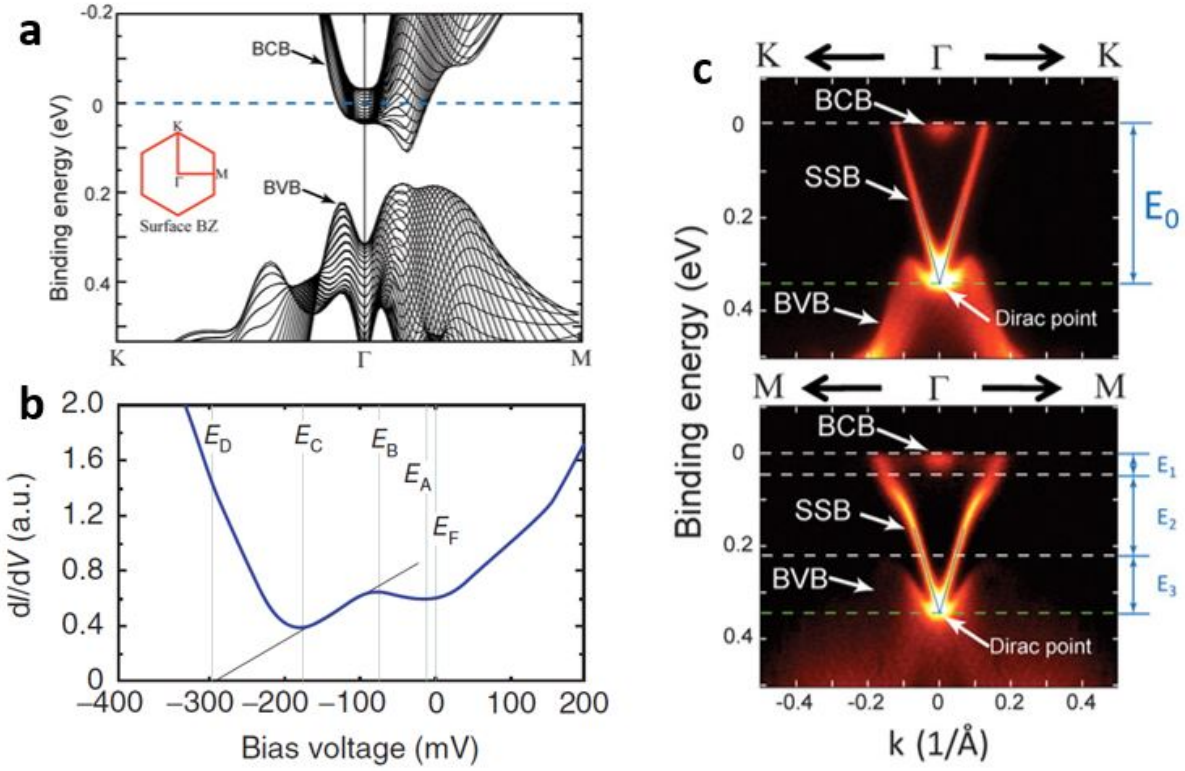

Figure 1.12: Electronic structures of Bi_2Te_3. (a) Calculated bulk conduction band (BCB) and bulk valance band (BVB) dispersions along high-symmetry directions of the surface Brillouin zone (see inset), with the chemical potential rigidly shifted to 45 meV above the BCB bottom at Γ to match the experimental result. (b) Density of states measured by STS. E_D is the Dirac point, E_F is the Fermi level, E_A is the bottom of the bulk conduction band, E_B is where the surface state band opens up and E_C is the top of the bulk valence band. (c) ARPES measurements of band dispersion along $\mathrm{K}-\Gamma-\mathrm{K}$ (top) and $\mathrm{M}-\Gamma-\mathrm{M}$ (bottom) directions. The broad bulk band (BCB and BVB) dispersions are similar to those in (a), whereas the sharp V-shape dispersion is from the surface state band (SSB). The apex of the V-shape dispersion is the Dirac point. Energy scales of the band structure are labeled as follows: E_0: binding energy of Dirac point (0.34 eV); E_1: BCB bottom binding energy (0.045 eV); E_2: bulk energy gap (0.165 eV) and E_3: energy separation between BVB top and Dirac point (0.13 eV). Images taken from [57, 63].

In figure 1.12(a), ab initio calculations for the band diagram are shown that predict that Bi_2Te_3 is an insulator. Figure 1.12(b) shows the density of states (DOS) measured by STS. The Dirac point in Bi_2Te_3 is buried under the valence band maximum, which is away from the Γ point in the reciprocal space. This results in a rise in the DOS at the Dirac point, because contributions from the surface states and the bulk valence band are mixed. Consequently, in a $\mathrm{d}I/\mathrm{d}V$ or conductance spectrum of Bi_2Te_3 (which is proportional to the DOS) the minimum point does not agree with the Dirac point. Instead, a linear part on the $\mathrm{d}I/\mathrm{d}V$ curve above its minimum point is extended to a point where the conductance is zero to estimate the Dirac point. Figure 1.12(c) shows band dispersions

measured by ARPES experiments along two high-symmetry directions. One can see the broad spectra of the bulk electron on top and the Mexican hat shape valence band at the bottom, as predicted in the ab initio calculation. There is also an extra sharp V-shape dispersion resulting from the surface states. The linear dispersion in the ARPES measurements indicates a massless Dirac fermion [57].

The surface states deviate from a simple Dirac cone due to a smaller band gap of about 0.15 eV and a strong trigonal potential [30]. The Dirac point is buried under the valence band maximum, which is away from the Γ point in the reciprocal space. Density-functional theory (DFT) calculations of the Bi_2Te_3 band structure made in the past reveal significant differences between the theoretically predicted and experimentally measured values for the bulk band gap (50-130 meV and 150-220 meV, respectively) [1].

1.4 Research aims

The surface states of 3D TIs are protected against nonmagnetic backscattering. This has been experimentally confirmed for the Bi_2Te_3 surface by Zhang *et al.* [64]. In their work, silver (Ag) impurities do not lead to backscattering: backscattering of the topological states by nonmagnetic impurities is completely suppressed.

Since this protection from backscattering is assured by time reversal symmetry, magnetic scattering is considered to have a pronounced impact on the allowed scattering processes of the helical surface states. Once an impurity acquires a magnetic moment it can spin-exchange with the incident Dirac particle and allow for spin-flip induced backscattering. Breaking time reversal symmetry in TIs is expected to create a host of exotic topological magnetoelectric effects. The most important prediction is that ferromagnetically ordered TIs are ideal systems for realizing the quantum anomalous Hall effect (QAHE) [21,65–68]. Because of this, magnetically doped TIs have attracted the interest of the scientific community.

An opening of the energy gap at the Dirac point due to the broken time reversal symmetry has been directly observed in magnetically bulk doped 3D TIs [12, 13]. Magnetic doping at the surface has been less intensively examined, while it is expected to also strongly influence the Dirac fermions of the surface states [22]. A study by Martínez-Velarte *et al.* [69] found that by depositing cobalt atoms at the Bi_2Te_3 surface, the protection against backscattering breaks down. Here, the atomic deposition was performed at a temperature below 5 K. A similar experiment was conducted at the KU Leuven [70]: cobalt atoms were deposited on a Bi_2Te_3 sample and investigated by means of scanning tunneling microscopy and spectroscopy. The deposition in this work occurred at room temperature. In this work, features appearing at the sample surface could be futher clarified with the help of density functional theory (DFT) calculations performed by Dr. Dmitry Muzychenko of Lomonosov Moscow State University. The features were identified as single-atom, two-atom and three-atom substitution of cobalt atoms at bismuth sites in the second atomic layer, as shown in figure 1.13. Since the deposition was performed at room temperature, the atoms were able to diffuse across the surface. It is not obvious why the atoms diffuse to the second atomic layer.

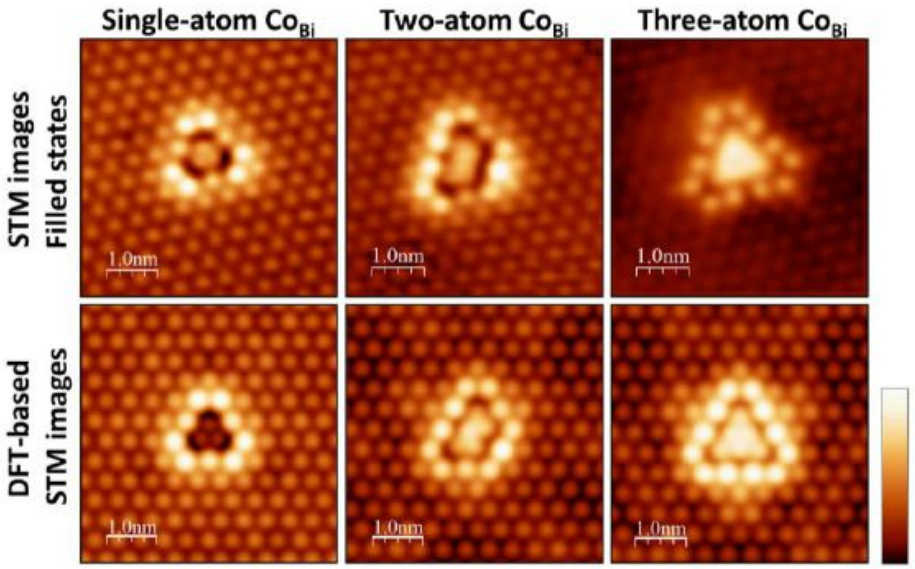

Figure 1.13: Atomically resolved STM images and the corresponding DFT based images. Upper images show the experimental features, which can be identified as single-atom, two-atom and three-atom Co_{Bi} substitution in the second atomic layer. Lower images show the DFT based STM images that support the experimental data. Image taken from [70].

The sample in the previously mentioned work had many impurities and defects. Because of this, it is interesting to repeat the performed experiments with a higher quality Bi_2Te_3 sample. This is the aim of this work.

In a first phase of the thesis, the sample quality is investigated. This is done by means of STM, STS, AES and LEED. To better understand the sample properties, the native defects of the sample are examined. The goal is to identify them, as this could help in understanding the role of native defects in doping of TIs. This could be achieved through comparison with the DFT based simulations of Dr. Muzychenko [71] and with other results reported in literature.

The second part of this work focuses on magnetic atom (cobalt and chromium) depositions. The sample surface after the depositions is investigated using STM and STS. It is interesting to see whether the higher quality sample will show the same features as the sample used in the previously performed work. Differences or similarities observed for different sample or different dopant properties might be useful in understanding the mechanism behind forming features resulting from the doping and ultimately in understanding the interaction between the TI surface and the magnetic dopants.

By investigating the scattering events at the surface, one can see whether backscattering occurs at the surface. At the bare sample surface, backscattering is expected to be prohibited. By depositing atoms with a magnetic moment, time reversal symmetry should be broken and backscattering allowed. These predictions are examined in this thesis. Apart from STM and STS imaging in real space we also rely on fast-Fourier transforms of the images to investigate how the $E(k)$ band structure dispersion relation near the Dirac point is affected by the magnetic scattering.

Chapter 2

Experimental techniques

This chapter describes the experimental techniques that were used for the work presented in this thesis. In section 2.1, scanning tunneling microscopy (STM) and scanning tunneling spectroscopy (STS), techniques which are used in all experimental chapters, are introduced. The techniques of Auger electron spectroscopy (AES) and low-energy electron diffraction (LEED) are explained in section 2.2. These techniques are employed in chapter 3.

2.1 Scanning tunneling microscopy

In order to understand and characterize the properties of materials at the atomic scale, appropriate measurement tools are needed. In this respect, STM is a suitable technique for realizing atomic scale studies [72]. It was the first technique that was able to generate real-space images of surfaces with atomic resolution [73] and so it is not very surprising that only five year after its invention in 1981, the Nobel Prize in Physics was awarded to Gerd Binnig and Heinrich Rohrer (who built the first scanning tunneling microscope at the IBM Research Laboratories in Zürich, Switzerland) [74]. In this section, physical principles underlying STM and how these are used to get topograhic information of the surface of a sample are discussed in subsection 2.1.1. In subsection 2.1.2, the spectroscopic variant STS and how it can be used to get information about the local density of states (LDOS) of the surface of a sample are discussed. Subsection 2.1.3 focuses on STM and STS as techniques suitable for investigating TIs. The last subsection (2.1.4) presents the low-temperature ultra high vacuum (UHV) STM setup used in this work.

2.1.1 Scanning tunneling microscopy

Scanning tunneling microscopy relies on two principles. The first principle is that the microscope uses a sharp tip or probe and that by bringing it close enough to the sample of interest, a tip-surface interaction can be detected. Second, one measures this interaction while moving the tip along the sample surface in a raster pattern. This tip-surface interaction is heavily dependent on the tip-surface distance, implying that it also depends strongly on the sample topography. The raster pattern of the recorded tip movement can thus be used to visualize the sample topography. The tip should be able to move with respect to the sample both in the lateral (x and y) and the vertical (z) direction. To achieve this, the sample (or the tip) is mounted on a piezoelectric scanner. When an

electric field is applied, this device can contract or extend locally, moving the sample by distances of only about 0.1 nm. The surface is scanned in a raster pattern and during this process, the local interaction between the tip and the sample is recorded and regulated through a feedback system. The tip interacts with the sample surface is through electron tunneling between them. According to classical physics, this is impossible since a current flow between two electrically conducting materials is only allowed when they are in mechanical contact. When taking a quantum mechanical approach, this changes. Due to the wave-particle duality, a small electron current is allowed if the two materials are not touching but are very close to each other (about 0.1 nm). At these small distances, the wave functions of the electrons at the apex of both electrodes overlap, leading to a finite probability of finding an electron beyond the barrier (which could be vacuum, air, liquid ...) when an external electric field is applied. Electrons prefer to tunnel through the barrier from one electrode to the other, which results in a net current flow: the tunneling current (see figure 2.1). The two electrodes are the STM tip and the sample and in the experiments, the externally applied bias voltages V are defined with respect to the sample, while the STM tip is virtually grounded. Electron tunneling can only occur when both the sample and tip are conductive or semi-conductive, which means that STM cannot be used on insulating materials.

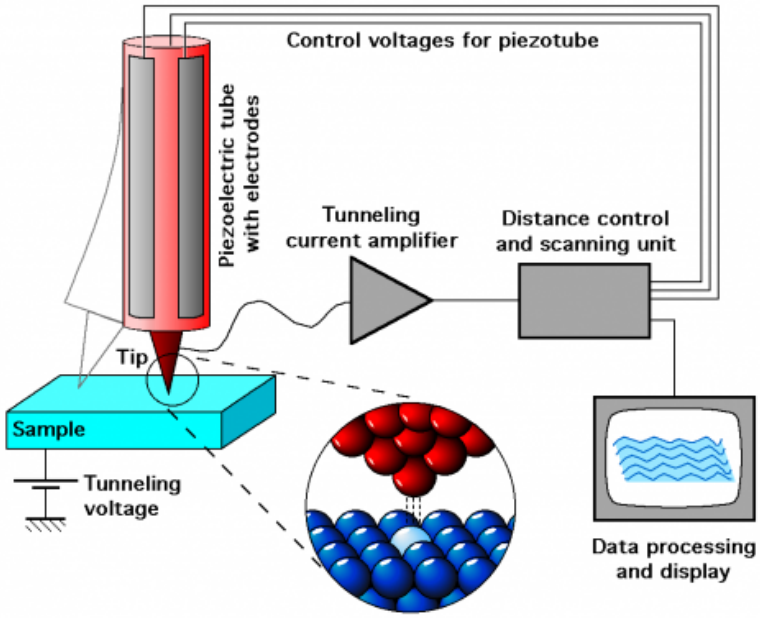

Figure 2.1: Schematic overview of a scanning tunneling microscope. The tip (red) and sample (blue) interact through a tunneling current. Image taken from [75].

The tunneling current I depends exponentially on the tip-sample distance d [76]. Because of this, the tunneling current is very sensitive to topographic height variations at the surface: changes of only 0.1 nm in the separation distance cause an order of magnitude difference in the tunneling current. The best results are achieved in ultra high vacuum and at very low temperatures, but it is also possible to achieve atomic resolution under ambient conditions. Using STM, there are two possible modes to image a sample surface: constant current mode and constant height mode. In *constant current* mode, a

feedback loop is responsible for adjusting the height of the tip by using the piezoelectric tube (closed feedback loop). This way, the tunneling current is always kept constant at a set-point value. By plotting the movements of the piezoelectric element that are needed to maintain a constant tunneling current at a certain bias voltage, one can image the surface topography. In *constant height* mode, the tip stays at a constant distance above the sample (open feedback loop). This way, the tunneling current will vary according to the topography and the local properties of the surface. By measuring this current at each location, one can form a topography image.

The exponential dependence of I on d implies that the tunneling current is mostly flowing via the outermost atoms at the tip apex. In this way, a very high lateral resolution is ensured: it can be as good as 0.01 nm for atomically flat surfaces. When the surface has some relatively profound features, with heights of 1 nm and more, the fact that the tip is not infinitely sharp comes into play: it has a radius of curvature R, which is typically a few nanometers. This finite bluntness of the tip determines (to a certain extent) the recorded size and shape of the surface features. This effect is known as the tip convolution effect. The vertical resolution is not affected by the tip apex an can be as good as 0.001 nm. Both the lateral and vertical resolution that can be achieved by STM imaging are far better than those of other techniques such as scanning electron microscopy, transmission electron microscopy or X-ray diffraction [77].

Not long after the invention of STM in 1981, Tersoff and Hamann developed a theory that could describe electron tunneling between a STM tip and a conducting surface. They built up their theory starting from Bardeen's perturbation formalism for the tunneling current flow between two metals separated by a thin insulating layer [78, 79]:

$$I = \frac{2e^2}{h} \sum_{\mu,\nu} (2\pi)^2 f(E_\mu) \left[1 - f(E_\nu) + eV\right] |M_{\mu,\nu}|^2 \delta(E_\mu - E_\nu), \tag{2.1}$$

where $2e^2/h$ is the quantum of conductance, $f(E)$ is the Fermi-Dirac distribution (the probability that the electronic state at energy E is occupied), V is the applied voltage and $M_{\mu,\nu}$ is the tunneling matrix element between the μ-th eigenstate ψ_μ of the first electrode (let's say the STM tip) and the ν-th eigenstate ψ_ν of the second electrode (the sample surface). E_μ and E_ν are the energies of the eigenstates ψ_μ and ψ_ν in the absence of tunneling. The delta distribution at the end ensures that energy is conserved. In order to evaluate equation 2.1, Tersoff and Hamann modeled the density of states of the tip apex as a locally spherical potential well with radius R. By using this model and some approximations valid after assuming the system to be in a limit of small externally applied voltages (of the order of meV) and moderate temperatures (room temperature or below), Tersoff and Hamann found that the electronic wave functions extend beyond the mechanical boundaries of the electrodes. Moreover, the surface wave functions ψ_ν decay exponentially outside of the metal, in the direction normal to the surface:

$$|\psi_\nu(r)|^2 \propto |\psi_\nu(0)|^2 \exp\left(-\frac{2r}{l_0}\right). \tag{2.2}$$

In this expression, $l_0 = \hbar/\sqrt{2m\phi}$ (with $\phi = \frac{\phi_T + \phi_S}{2}$ the average work function of the tip and the sample and m the electron mass) is the decay length for wave functions into the

vacuum barrier. The authors also demonstrated that the tunneling current I depends on the tip-sample distance d by $I \propto \exp(-2d/l_0)$. As mentioned before, this exponential $I(d)$-dependence is a very important result since it implies that the tunneling current is very sensitive to topographic height variations of the sample surface.

The Tersoff-Hamann model is very valuable in understanding the physical principles of STM. However, the low-voltage approximation is not valid in practice: many STM experiments are performed at bias voltages of up to 1 V and more, that is, the voltage is comparable to the barrier height ϕ. At these higher voltages the tunneling current does not arise from one state at the Fermi level, but from a range of states that lie within an energy eV of the Fermi level. This is illustrated in figure 2.2: energy diagrams for different conditions of the tunneling of electrons between the STM tip and sample are shown for the simplified case of a constant tip LDOS ρ_t. Since the sample under investigation has a finite size, the sample LDOS ρ_s is assumed to have some broadened energy states. When the tip and sample are not close enough for tunneling to occur, there is of course no net current (figure 2.2(a)). If they are close enough to allow a tunneling current, but there is no externally applied bias voltage V, the tip-to-sample and the sample-to-tip tunneling probability are the same and there is no net tunneling current (figure 2.2(b)). In this case, the Fermi levels of the tip and sample are aligned. Since the metal work functions ϕ_T and ϕ_S are different, the energy barrier is a non-rectangular trapezoid. When an external bias voltage V is applied, the sample LDOS is shifted either downward (figure 2.2(c)) or upward (figure 2.2(d)) with respect to the tip LDOS, with the direction of the shift depending on the polarity of the applied voltage V to the sample (positive or negative, respectively). Because of this shift, electrons tunnel in an energy window $[0, eV]$ either from the tip to unoccupied samples states or from occupied sample states to the tip.

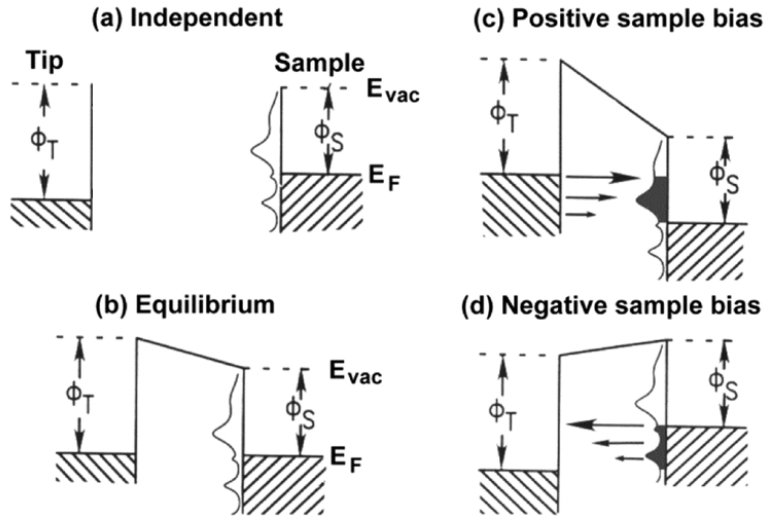

Figure 2.2: Energy diagrams of an STM tip and a sample in tunnel contact at different tunneling conditions. E_F is the Fermi level of the tip and surface, ϕ_T and ϕ_S are the work functions of the tip and surface. (a) The tip and sample are not close enough for tunneling to occur. (b) Energetic equilibrium at zero bias. (c) Net tunneling current from tip to sample at positive sample bias $V > 0$. Here, the empty states are probed. (d) Net tunneling current from sample to tip at negative sample bias $V < 0$. The filled states are probed. Image taken from [80].

The tunneling current at larger bias voltages can be obtained by taking the integral over the energies of the involved tip and sample states [81], yielding

$$I(V) \propto \int_0^{eV} \rho_t \left(E_F - eV + E\right) \rho_s \left(\vec{r}_o, E_F + E\right) \mathrm{d}E, \tag{2.3}$$

in which $\rho_t(E)$ is the LDOS of the STM tip. $\rho_s\left(\vec{r}_o, E\right)$ is the sample LDOS evaluated at the center of curvature of the tip $\vec{r}_o$. It can be related to the LDOS of the sample evaluated at the surface according to

$$\rho_s\left(\vec{r}_o, E\right) \propto \rho_s(E) T(E, V, d), \tag{2.4}$$

where $T(E, V, d)$ is a generalized version of the transmission coefficient based on the WKB-formula (Wentzel, Kramers and Brillouin) for electron tunneling through a one-dimensional potential barrier of arbitrary shape [43]:

$$T(E, V, d) = \exp\left[-2(R+d)\left[\frac{2m}{\hbar^2}\left(\phi + \frac{eV}{2} - \left(E - E_{\|}\right)\right)\right]^{1/2}\right]. \tag{2.5}$$

Here E is the total electron energy and $E_{\|}$ is the electron energy component parallel to the sample surface [81]. The voltage dependence of the transmission coefficient is illustrated by the length of the arrows in figure 2.2: higher energy electrons experience a smaller effective barrier height and so have a higher tunneling probability. Through equation 2.3, this in turn implies that they also have a larger contribution to the tunneling current I.

2.1.2 Scanning tunneling spectroscopy

Single point tunneling spectroscopy

By now it is clear that the exponential dependence of the tunneling current I on the applied bias voltage V is very useful as it can provide high-resolution topography images of the sample surface. When taking a closer look at equation 2.3, it becomes clear that the tunneling current can give us even more physical insight. I also depends on the sample LDOS ρ_s, where the range of contributing energy states is determined by the applied bias voltage V (see figure 2.2). To find this sample LDOS, one takes the first derivative of I with respect to V in equation 2.3. This gives the following expression for the differential conductance:

$$\begin{aligned}\frac{\mathrm{d}I}{\mathrm{d}V}(V, d) \propto{}& \rho_t\left(E_F\right) \rho_s\left(E_F + eV\right) T\left(E = E_F + eV, V, d\right) \\ &+ \int_0^{eV} \rho_t\left(E_F - eV + E\right) \rho_s\left(E_F + E\right) \frac{d}{dV}\left[T\left(E, V, d\right)\right] \mathrm{d}E \\ &+ \int_0^{eV} \frac{d}{dV}\left[\rho_t\left(E_F - eV + E\right)\right] \rho_s\left(E_F + E\right) T\left(E, V, d\right) \mathrm{d}E.\end{aligned} \tag{2.6}$$

In order to do this, local $\mathrm{d}I/\mathrm{d}V$ data are needed. They can be obtained in two different ways, both of which are used in this work. A first method is to position the tip above the location of interest, disable the feedback loop and record the tunneling current I while

linearly ramping the bias voltage. The result of this is a local $I(V)$-curve which can then be numerically differentiated to obtain the sample LDOS $\rho_s(E)$ at $E = E_F + eV$. Another method records the $\frac{dI}{dV}(V)$-spectrum directly by harmonic detection using a lock-in amplifier. This STS technique was first applied by Binnig *et al.* [82]. A small sinusoidal modulation voltage V_{mod} (10 - 40 mV) with frequency ω_L (300 - 7000 Hz) is superimposed on the linearly ramped DC bias voltage V_{DC}. Because of this modulation voltage, the recorded tunneling current $I\left(V_{\text{DC}} + V_{\text{mod}} \cos\left(\omega_L t\right)\right)$ shows an oscillating behaviour with frequency ω_L. This signal goes through a lock-in amplifier, where it is multiplied by a lock-in reference signal with frequency ω_L. This results in an output signal that is proportional to $\frac{\mathrm{d}I}{\mathrm{d}V}\big|_{V=V_{\text{DC}}}$, which is the first harmonic of $I\left(V_{\text{DC}} + V_{\text{mod}} \cos\left(\omega_L t\right)\right)$. The sample LDOS $\rho_s(E)$ obtained by this method is averaged over the energy region $[eV - eV_{\text{mod}}, eV + eV_{\text{mod}}]$.

Mapping the local density of states

As discussed in the previous section, the LDOS at a specific location on the sample surface can be determined by measuring the $\mathrm{d}I/\mathrm{d}V$-signal as a function of the applied voltage V. Sometimes it is useful to have the LDOS not only at a specific point, but at several places on the sample surface. One then visualizes the LDOS in differential conductance images $\frac{\mathrm{d}I}{\mathrm{d}V}(x, y)$ across the surface. These images are also referred to as LDOS maps and can be obtained in two different ways. Both are used in this thesis.

In a first method, LDOS maps are extracted from local $I(V)$-curves measured with open feedback loop, possibly combined with topographic imaging with closed feedback loop. From these data sets, the LDOS at a certain electron energy $E_F + eV$ is extracted in the same way as for single point spectroscopy. The spatial variation of the $\mathrm{d}I/\mathrm{d}V$ data that are obtained this way at the bias voltage V is plotted. This method is often referred to as current imaging tunneling spectroscopy (CITS) [81].

A second way to acquire differential conductance images is by using a closed feedback loop by means of harmonic detection with a lock-in amplifier. Here, a modulation voltage V_{mod} is added to the DC bias voltage V that is applied to the sample. As discussed in the previous section, the lock-in amplifier extracts the tunneling conductance $\mathrm{d}I/\mathrm{d}V$ from the tunneling current I that is recorded while raster scanning the sample surface in constant current mode, thereby providing a map of the sample LDOS at energy $E_F + eV$.

2.1.3 Visualizing topological insulators using STM and STS

As briefly mentioned in subsection 1.3.2, STM is a commonly used technique for studying TIs. Because of its surface sensitivity, STM has a clear advantage when trying to probe the conductance of the surface states. STM experiments have played a key role in directly visualizing 2D surface states in 3D TIs and in recognizing some of their novel properties. These experiments have provided insight into how bulk defects may be limiting the mobility of these states because of their modulation of background bulk electronic states. The LDOS measured by STS cannot directly provide the band structure of TI materials, but it can be examined by using the corresponding energy-momentum dispersion relation from ARPES measurements. In addition to the linear Dirac dispersion and Landau quantization, the absence of backscattering from nonmagnetic defects for topological surface

states has also been confirmed by STM and STS experiments [1, 83, 84].

Within the context of this thesis, this last item (the absence of backscattering) is particularly relevant. These experiments are performed through STS measurements. Energy-resolved spectroscopic maps display modulations that are the result of scattering of the surface electronic states. A surface state is uniquely characterized by a 2D Bloch wave vector $\vec{k}$ within the surface Brillouin zone. During elastic scattering, a defect scatters the incident wave with wavevector $\vec{k}_i$ into $\vec{k}_f = \vec{k}_i + \vec{q}$, where $\vec{k}_i$ and $\vec{k}_f$ lie on the same constant energy contour (CEC) of the Dirac cone. The quantum interference between the initial and final states results in a standing wave pattern of the LDOS with wavelength $\lambda = 2\pi/q$. These standing wave patterns or modulations are known as *quasiparticle interference patterns* or QPIs. The Fourier transforms of the STS maps show rich patterns, which display the allowed wavevectors $\vec{q}$ and the relative intensities for the various scattering processes experienced by the surface state electrons [64, 85, 86]. The tunneling of the electrons from the STM tip is predominantly into the surface states, as no consideration of tunneling to the bulk is required to explain the observed intricate QPIs due to scattering of surface states from dopants. A schematic depiction of QPI is shown in figure 2.3.

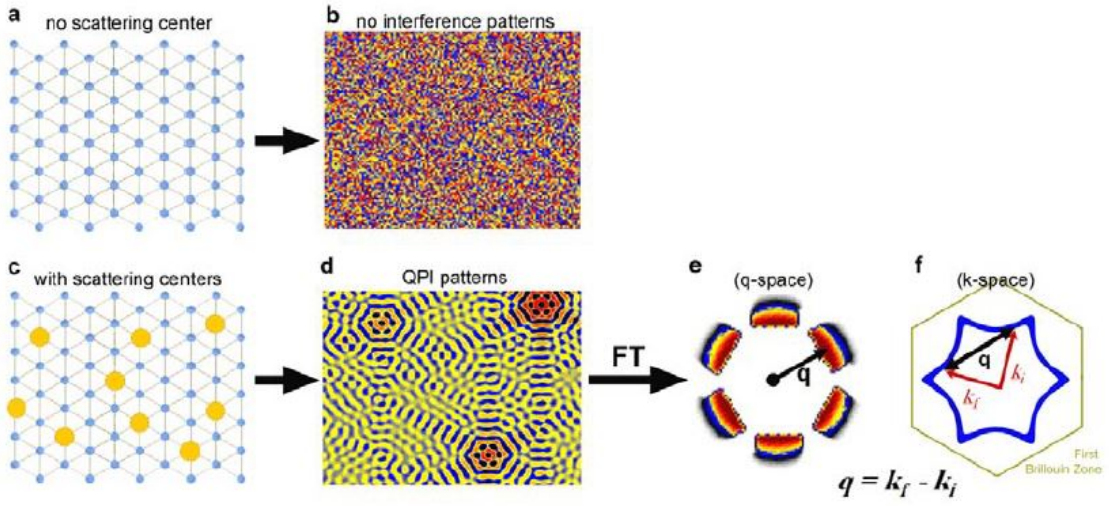

Figure 2.3: Schematic demonstration of QPI. Surface scattering events provide a way to study the electronic surface states. (a) In the absence of any scattering centers, there is no interference pattern, as can be seen in (b). In this case there is no spatial pattern to the conductance. (c) The scattering of surface states from defects leads to an interference pattern (d). (e) The Fourier transform of the interference patterns leads to a map of all scattering wavevectors (q's) and their intensities. (f) The q's are related to initial ($\vec{k}_i$) and final states ($\vec{k}_f$) of scattering by a simple relation, $\vec{q} = \vec{k}_f - \vec{k}_i$. The blue curves represent a contour of constant energy. Image taken from [83].

Experiments performed on 3D TIs using this QPI principle reported a significant suppression of the scattering intensity along directions equivalent to the $\bar{\Gamma} - \bar{\mathrm{K}}$ direction in the hexagonal first Brillouin zone, while backscattering should give rise to a continuous range of scattering wavevectors along the $\bar{\Gamma} - \bar{\mathrm{K}}$ direction. This discrepancy is explained by the

helical spin texture of the TIs: spin rules are limiting the backscattering events [83]. The technique of QPIs will be applied in the experimental chapters of this work when studying scattering events at the surface in subsections 3.5, 4.4 and 5.4.

2.1.4 The low-temperature UHV STM

STM and STS measurements in this work were performed with a commercial scanning tunneling microscope (Omicron Nanotechnology). The setup consists of two chambers, the actual STM chamber and a sample preparation chamber, that are independently pumped by means of an ion pump and an additional titanium sublimation pump, ensuring operation under ultra high vacuum (UHV) in both chambers. The base pressure of the STM chamber is 5×10^{-11} mbar, while that in the preparation chamber is 5×10^{-10} mbar. The setup is shown in figure 2.4. The inset gives a zoomed-in view of the scanner and the sample stage.

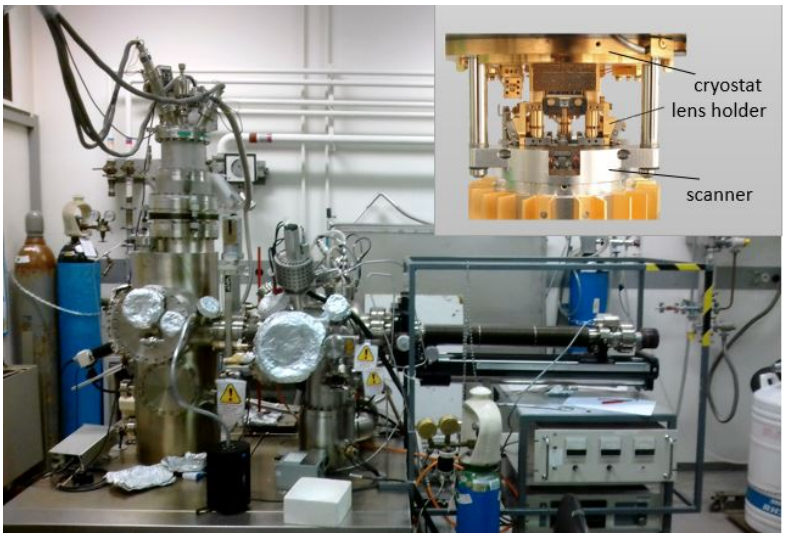

Figure 2.4: The low-temperature ultra high vacuum STM setup, consisting of the STM measurement chamber and the preparation chamber. Inset (taken from Scienta Omicron Nanotechnology [87]): in the STM chamber the scanner and the sample stage are present. The sample can be brought in contact with the cryostat for cooling to low temperatures.

Samples are inserted through a separate load-lock chamber, that can be pumped and vented separately from the STM and preparation chamber. They are then mounted on a large rotational transfer arm that transports them to the preparation chamber first and from there to the STM chamber. The microscope is located in a thermally shielded compartment that is directly attached to a cryostat. The cryostat has an inner and outer part, which allows for measurements both at room temperature and at low temperatures. For working at low temperatures, the outer part is filled with liquid nitrogen while the inner part is filled with either liquid nitrogen (78 K) or liquid helium (4.5 K). The best topography and energy resolution is achieved at the lowest temperatures, so the sample temperature of 4.5 K is used in the measurements. The time available for STM measurements at liquid helium temperatures without refilling the cryostat is around 24 hours. To minimize the effect of external vibrations, there is a spring suspension system with Eddy current damping. The bias voltages V given in the text and figure captions are always

with respect to the sample, while the STM tip is virtually grounded. Image processing is performed by Nanotec WSxM [88].

Preparation of STM tips

Electrochemically etched tungsten (W) tips (Omicron Nanotechnology) were used for the STM experiments. They were cleaned in-situ by repeated flashing well above 1000 K in order to remove the surface oxide layer and any other surface contamination. To test the quality of the tip before use, topography and spectroscopic measurements on the known Au(111) surface were performed.

Sample preparation for STM and STS

Most samples are typically cleaned by sputtering by an argon gun which this setup is equipped with or by annealing at a certain temperature. The Bi_2Te_3 sample however, is not sputtered or annealed because the annealing induces the formation of a Bi bilayer atop the Bi_2Te_3 surface [89]. Instead, it is cleaved using the scotch-tape method. Because the Bi_2Te_3 surface is drastically modified upon exposure to ambient [90], the cleaving is performed in-situ inside the UHV STM chamber, using UHV-compatible carbon tape. The equipment used in the cleaving process is shown in figure 2.5. The van der Waals gap between the QLs yields a preferential cleavage between adjacent Te layers, but cleavage within a QL rather than between two successive QLs may also occur.

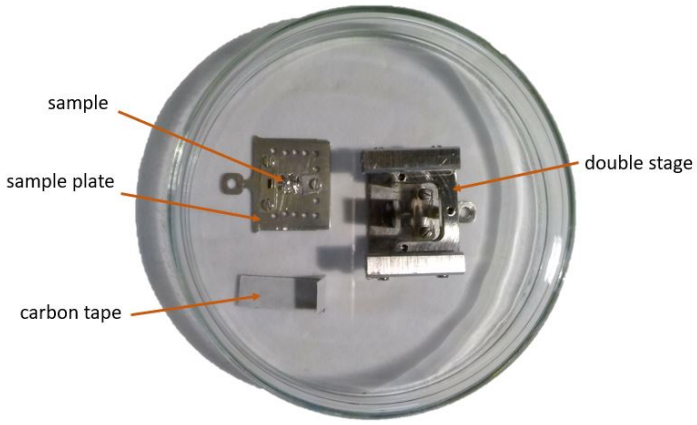

Figure 2.5: The sample is clamped into a sample holder. This sample holder is put into a double stage and the carbon tape is used to attach the sample to the double stage. When the sample plate is pulled out of the double stage again inside of the STM setup, the carbon tape takes away some of the material, effectively cleaving the surface.

Deposition of cobalt and chromium atoms

In this work, cobalt (Co) and chromium (Cr) atoms are deposited on the Bi_2Te_3 surface at room temperature. This is done by physical vapor deposition in two separate e-beam evaporation cells, which the preparation chamber is equipped with, at pressures below 10^{-9} mbar and with low deposition rates in the range of $0.01 - 0.05$ nm/minute. Atoms are vaporized from a high purity rod of cobalt (2.0 mm diameter, 99.995 % purity) or from chromium granules (99.999 % purity) inside a molybdenum crucible by means of an

electron gun (this is needed because of the high melting temperatures of these elements). In both cases, the evaporated atoms then exist in the gaseous phase and cover the sample surface.

2.2 Additional surface analysis techniques

This section discusses two surface analysis techniques. A first one is Auger electron spectroscopy (AES), a technique widely used for determining the chemical composition of surface layers of a sample. Its working principle is based on the Auger effect, which was discovered independently by both Lise Meitner and Pierre Auger in the first half of the 1920s [91, 92]. This process is the subject of subsection 2.2.1. The other technique discussed is low-energy electron diffraction (LEED), which is used in order to determine the surface structure of single-crystalline materials. It is the subject of subsection 2.2.2. The setup used for AES and LEED in this work is presented in subsection 2.2.3.

2.2.1 Auger electron spectroscopy

Auger electron spectroscopy is based on the analysis of energetic electrons emitted from an excited atom after a series of internal relaxation events. When a high-energy electron beam (1-30 keV) is incident on a sample it will knock out core electrons from the atoms inside. The created vacancy will be filled immediately with an electron from the upper shells and the energy released in this transition is carried away by a characteristic X-ray or alternatively, by another electron from the upper shells which is emitted: the Auger electron. The energy of the transition is transferred to the Auger electron and so the kinetic energy of this electron corresponds to the energy difference of the initial electronic transition. The Auger transitions are labelled by the energy levels of the electrons involved. The first character labels the energy level of the initial core hole. The second and third correspond to the other energy levels involved. If one of the levels involved is the valence band of the solid, one usually writes the letter V instead of the X-ray spectroscopy label of the shell. An example of such an Auger transition is shown in figure 2.6.

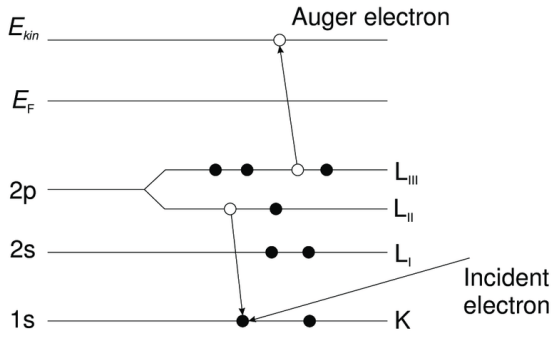

Figure 2.6: An initial process, like an incident high energy electron, removes a K shell electron. A second electron neutralizes the hole state and transfers the energy gained in the process to a third electron. This transition is a $KL_{II}L_{III}$, or simply KLL, transition. Image adapted from [93].

A scheme of the setup is shown in figure 2.7. Electrons from an electron gun are incident on the sample, after which Auger electrons are emitted. The emitted Auger electrons (as well as all the other electrons) are detected with an electron analyzer and filtered with respect to their kinetic energy. The electron analyzer in this setup is a Thermo Alpha 110 hemispherical analyzer [94]. This results in a spectrum with intensity as a function of kinetic energy. From the spectrum, conclusions can be drawn about the stoichiometry as well as the chemical state of surface atoms in the sample. Because no two elements have the same binding energy for all electronic levels, the kinetic energy of the Auger electron can be used to identify elemental species. Additional information can be gained from the peak shape and, to limited extent, from the peak position of the Auger peaks. Since only the electrons from the surface layers can leave the sample without energy loss, AES is a surface sensitive technique. Because there are three electrons involved in the Auger process it is however impossible to detect H or He [93, 95].

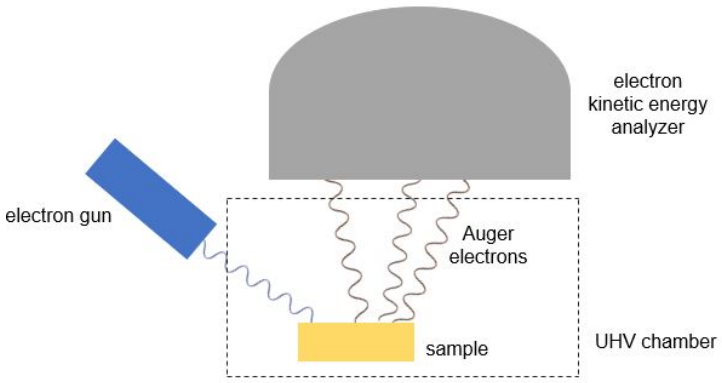

Figure 2.7: Auger electrons spectroscopy setup. Using an electron gun, a high-energy electron beam is incident on a sample. Auger transitions happen and the outgoing Auger electrons are detected by an electron analyzer.

2.2.2 Low-energy electron diffraction

Low-energy electron diffraction (LEED) is a technique for the structural investigation of crystalline surfaces based on the diffraction of electrons with low kinetic energy. Electron diffraction is based on the wavelike nature of a beam of electrons when passing near matter. A beam of electrons has a characteristic wavelength known as the De Broglie wavelength, which is inversely proportional to the momentum of the beam: $\lambda_B = h/p$. When the speed of the electron beam (and hence p) is high enough, the electron wavelength becomes as small as the spacing between atomic layers in crystals. The crystal structure then acts as a grating: electrons passing through the atomic planes interfere with each other before reflecting, which results in a diffraction pattern that shows the crystal structure [96].

In the setup used in this work, which is pictured in figure 2.8, a low-energy electron beam (up to 1 keV) is incident on a sample. The wavelength of these electrons is around 1 - 2 Å, which is less than the interatomic distance, making atomic diffraction possible. The mean free path of these low energy electrons is of the order of a few atomic layers. Because of this, most collisions occur in the very top layers of the sample, which makes

it a surface sensitive technique. After being diffracted, the electron beams are incident on a fluorescent screen, revealing diffraction patterns. The surface structure can then be deduced from the analysis of the elastically scattered particles in the crystal. The intensity of the diffracted beams yields information on the atomic arrangement within a unit cell while the spatial distribution of the diffracted beams contains information on the surface structure [97]. LEED is a very suitable technique for structural surface analysis because it combines extremely high surface sensitivity with the possibility of determining atomic structure.

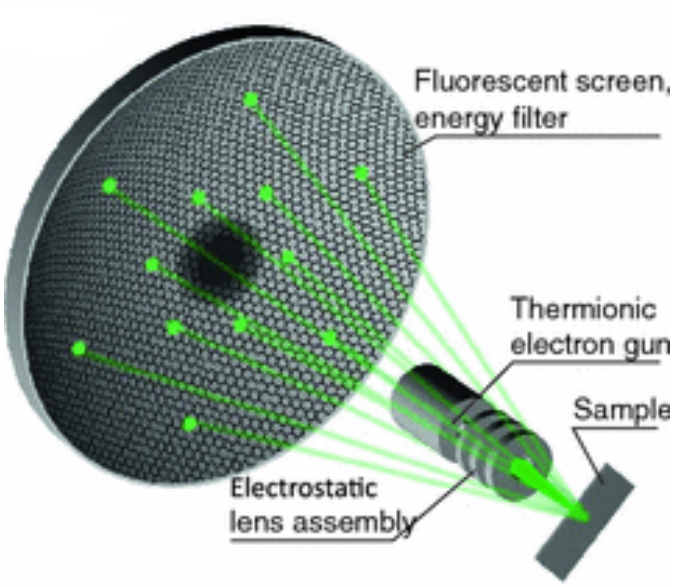

Figure 2.8: Schematic diagram of a LEED setup. Image taken from [97].

2.2.3 Surface analysis at the Ion and Molecular Beam Laboratory

The setup used for AES and LEED in this work is part of the Ion and Molecular Beam Lab (IMBL) at the KU Leuven. AES and LEED are implemented into the same setup, which makes it possible to retrieve chemical and structural information about the surface at the same time [98]. The IMBL offers several material analysis techniques [99], but for this work only AES and LEED are used. Both are part of the surface analysis chamber, which is in turn part of the UHV system of the IMBL.

Sample preparation for AES and LEED

Firstly, the sample is cleaved in ambient at a wet bench. Afterwards it is inserted into the UHV system. There a ion gun is used to remove atomic layers (and hence contamination) by sputtering Ar^+. The sputtering beam has an energy of 500 eV and a current of 1.5 μA. Sputtering is done with an incident angle of 60 °.

Chapter 3

Characterization of the Bi_2Te_3 surface

As detailed in chapter 1, TIs are fascinating materials hosting robust spin-polarized surface states with a linear dispersion. Furthermore, the topological surface states may host exotic quantum phenomena like the QAHE when time reversal symmetry is broken. In order to realize these phenomena experimentally, one needs intrinsic TIs. However, crystalline defects cause doping in several TIs (including Bi_2Te_3), which causes their transport properties to be heavily affected by bulk carriers [5]. Clear identification and understanding of these native defects is thus an essential step in TI research.

In this chapter, the bare surface of a Bi_2Te_3 sample is characterized. Information about the growth of the sample can be found in section 3.1. In section 3.2, the surface is studied using STM and STS on a large scale, while section 3.3 focuses on specific defects using the same methods. Where possible, the native defects are identified through comparing STM images of them with both density functional theory (DFT) calculations performed by Dr. Dmitry Muzychenko of the Scanning Probe and Nanoelectronics Laboratory at Lomonosov Moscow State University [71] and results reported in literature [100]. Subsection 3.3.2 entails a statistical analysis to get a better view on the relative frequencies of the defects and their density. Section 3.4 of this chapter entails an additional analysis of the surface through Auger electron spectroscopy (AES) and low-energy electron diffraction (LEED), techniques described in section 2.2. In the last section 3.5 of this chapter, the scattering events at the sample surface are examined through quasiparticle interference patterns (QPIs), which were discussed in subsection 2.1.3.

3.1 Sample growth

The sample used in this work is a 5×3 mm^2 crystal grown at the company 2D Semiconductors using the flux method [101]. In this method, a flux of elements and raw materials for target compounds are mixed using a mortar and put into a crucible. There are two kinds of flux methods. The flux can either have the elements in the desired products as components or consist of other elements. The mixed powder is then heated for the solution-growth process, thereby obtaining single crystals. Non-oxide materials (like Bi_2Te_3) are heated in a closed atmosphere, for example vacuum sealed in a quartz

tube [102].

3.2 Overview

In this section, the Bi_2Te_3 surface is studied on a larger scale of about 150×80 nm^2 and on a typical scale of 70×70 nm^2 with atomic resolution. Subsection 3.2.1 entails the determination of the height of one quintuple layer, overview STM topography scans and the calculation of the interatomic distance. In subsection 3.2.2, the density of states is investigated by means of tunneling spectroscopy experiments.

3.2.1 Topography

A larger scale STM topography image is shown in figure 3.1. A height profile taken along the blue line in the figure reveals a step of 1.0 ± 0.1 nm in height, which is approximately the height of one QL. A smaller substep can be seen, which is probably a sub-QL. It is characteristic of in-situ cleaving.

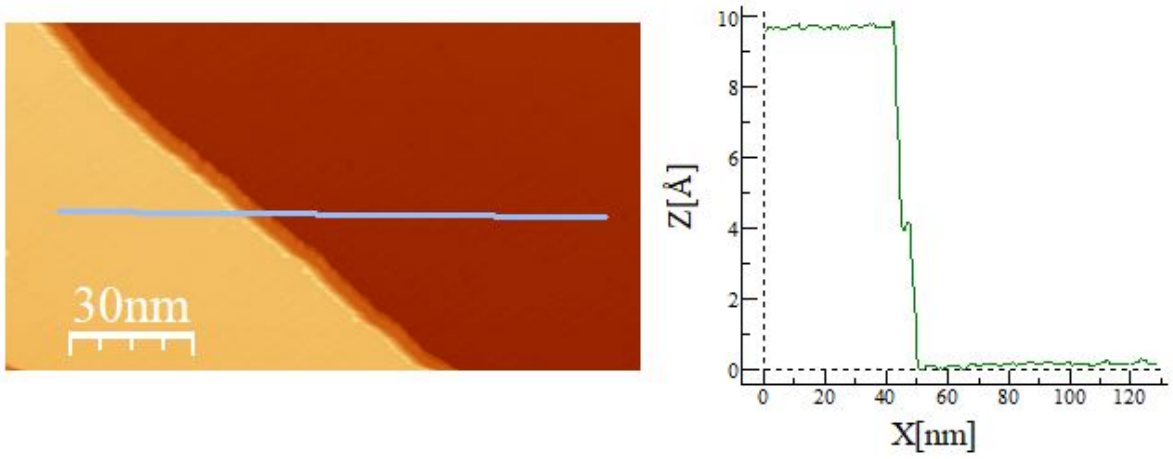

Figure 3.1: (left) STM topography image of about 150×8 nm^2 of the Bi_2Te_3 surface at $I = 0.2$ nA and $V = -1$ V. (right) Height profile taken along the blue line indicated in the topography image. The blue arrow indicates a substep.

An overview of the topography of the sample surface at a scale of 70×70 nm^2 is shown in the figures below. In this thesis, empty states are always imaged in blue, while filled states are represented in orange. Figure 3.2 shows a 70×70 nm^2 topography scan at a tunnelling current $I = 1$ nA and voltage $V = \pm 700$ mV. Figure 3.3 shows a topography image of the same size but at $I = 0.3$ nA and $V = \pm 100$ mV. These two images show different structural defects, which are examined in depth in section 3.3. The most frequent among them are depressions or holes and triangularly shaped protrusions. These scans illustrate that a difference in measurement settings allows to probe different defects and also that the same defects may look different when using different settings. These settings, as introduced in chapter 2, are used in such a way that by changing the bias voltage one probes different energy states.

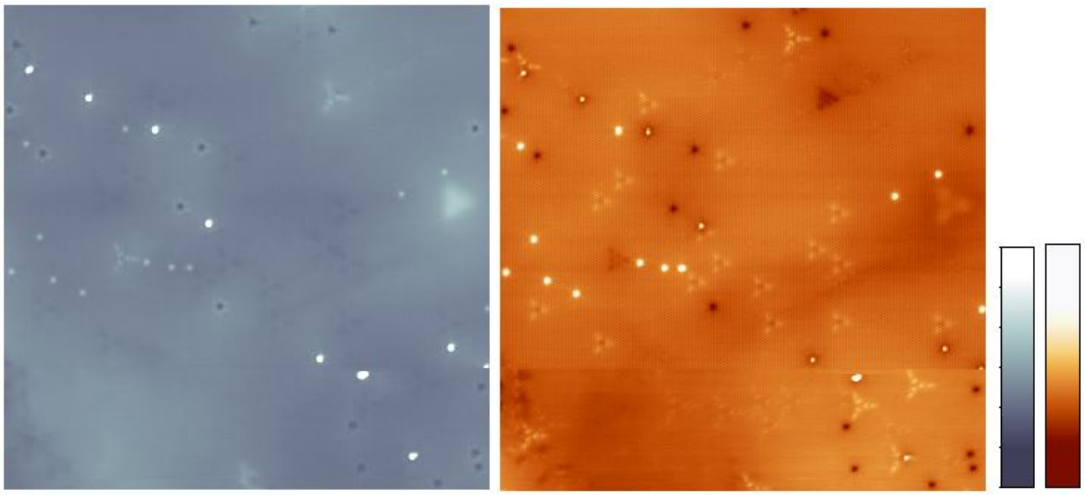

Figure 3.2: 70×70 nm^2 STM topography image of the Bi_2Te_3 surface at $I = 1$ nA and (left) $V = +700$ mV (right) $V = -700$ mV. The two bars show the color scale which is used throughout this work: brighter corresponds to higher points of the surface.

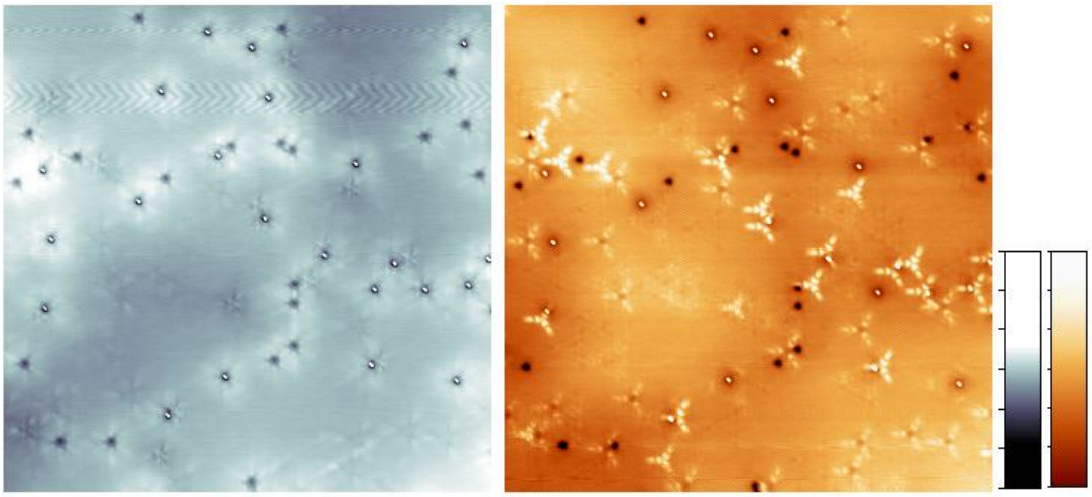

Figure 3.3: 70×70 nm^2 STM topography image of the Bi_2Te_3 surface at $I = 0.3$ nA and (left) $V = +100$ mV (right) $V = -100$ mV.

In figure 3.4, an atomic resolution image of the surface is shown. The hexagonal order of the Bi_2Te_3 crystal is clearly visible. Using several ($N = 12$) height profiles along the atoms, the interatomic distance d was measured several times. Two of these profiles are shown at the right side of the figure. By taking the average $\bar{d}$, the interatomic distance is found to be $d = 0.45 \pm 0.01$ nm $= 4.5 \pm 0.1$ Å. This error has a 68 % confidence level, and was determined by the standard deviation with the following formula:

$$d = \bar{d} \pm \sqrt{\frac{\sum_i^N (d_i - \bar{d})^2}{N(N-1)}}. \tag{3.1}$$

While this value does not match the literature value of 4.3835 Å [61] exactly, it is very close. This is explained by non-linear response of the piezo scanner. To measure more

accurate distances, the piezo scanner should be recalibrated using a reference sample, for example graphite.

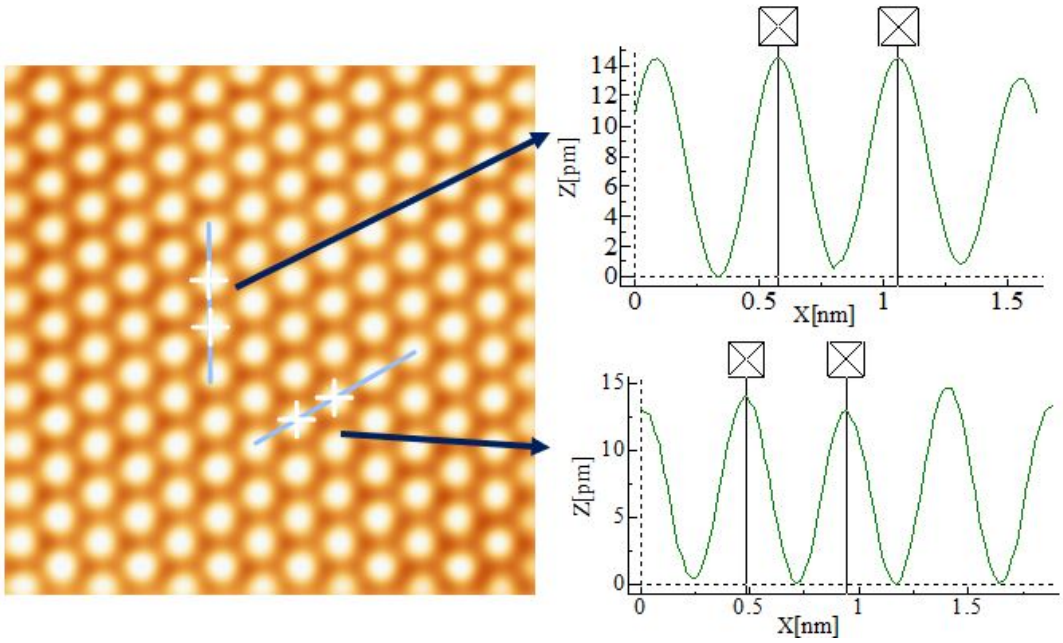

Figure 3.4: 5.4×5.4 nm^2 STM topography image of the Bi_2Te_3 surface at $I = 2$ nA and $V = -300$ mV. Two height profiles which are taken across the blue lines along the surface are shown on the right.

3.2.2 Spectroscopy

Having examined the surface topography, the density of states is investigated by means of tunneling spectroscopy: figure 3.5 shows the average curve of the tunneling current as a function of the bias voltage and a conductance spectrum averaged over a surface area of about 60×50 nm^2.

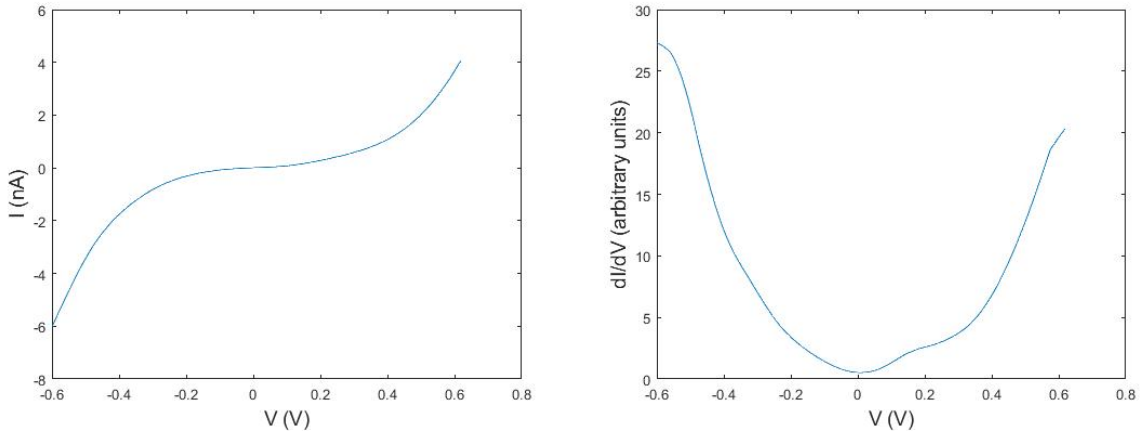

Figure 3.5: (left) $I(V)$ curve and (right) $\mathrm{d}I/\mathrm{d}V$ spectrum, both averaged over an area of about 60×50 nm^2 of the surface.

The energy and hence also the bias voltage is referenced with respect to the Fermi level: $E_F = 0$ eV. The $\mathrm{d}I/\mathrm{d}V$ curve shows a general suppression of the density of states near the Fermi level. The presence of conducting surface states makes the spectrum different from that seen on the surface of ordinary insulators: in normal band insulators, the conductance becomes zero for the energies corresponding to the energy bandgap, while here the local density of states (LDOS) remains finite for energies inside the gap due to the contribution of the surface states to the LDOS. The Fermi level (corresponding to zero bias) is seen to lie inside the band gap. The sample is either intrinsic or slightly p-doped. Other Bi_2Te_3 crystals have also shown n-type conductivity [63] (see figure 1.12b for example).

This intrinsic or p-doped character of the sample can be understood through the formation energy of native defects calculated by Wang *et al.* [103], shown in figure 3.6.

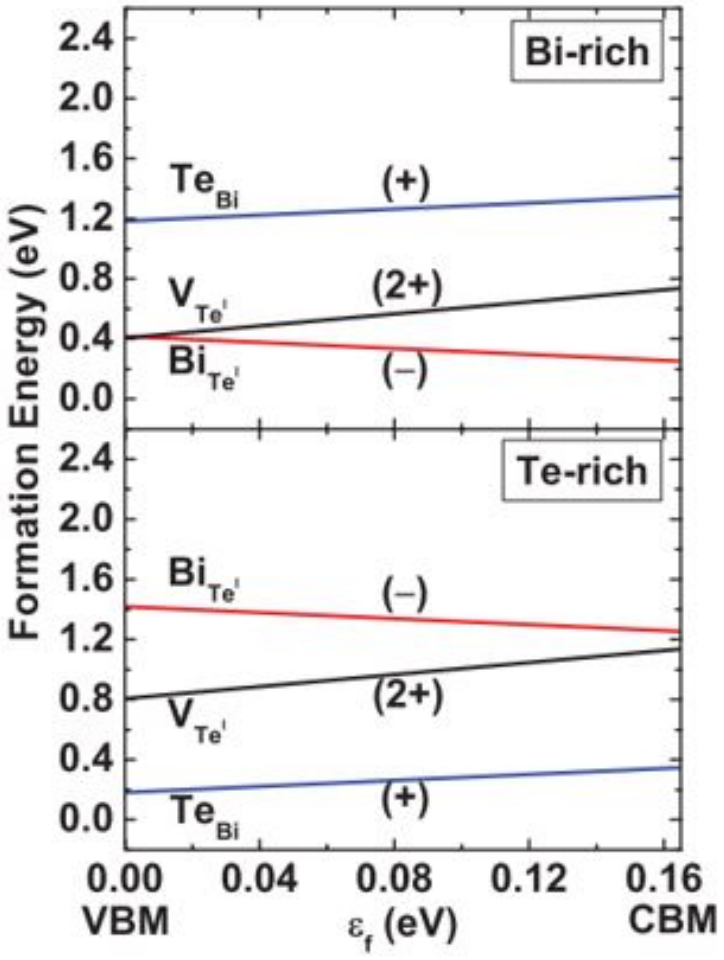

Figure 3.6: Defect formation energy as a function of the Fermi level in Bi_2Te_3, in a range from the valence band maximum (VBM) to the conduction band minimum (CBM). The top panel is for Bi rich conditions, the bottom one for Te rich conditions. Image taken from [103].

Three types of defects are considered: a bismuth atom substituting a tellurium atom which is singly negatively charged (Bi_{Te}), a tellurium vacancy which is doubly positively charged (V_{Te}) and a tellurium atom substituting a bismuth atom which is singly positively charged (Te_{Bi}). For Bi_2Te_3 grown under Te rich conditions (bottom panel of figure 3.6), Te_{Bi} has the lowest formation energy and acts as a shallow donor. The other two defects that are considered have a higher formation energy. Bi_{Te} acts as a shallow acceptor. Due to the low formation energy of Te_{Bi}, Bi_2Te_3 behaves as n-type under Te rich conditions. For Bi_2Te_3 under Bi rich conditions (top panel of figure 3.6), the formation energy of Te_{Bi} becomes higher due to changes in the chemical potential, while the formation energy of Bi_{Te} drops to below that of V_{Te}. This results in Bi_{Te}, a singly charged acceptor, becoming the dominant effect. Under Bi rich conditions, Bi_2Te_3 thus behaves as p-type. The crystal changes from n-type to p-type from Te to Bi rich conditions [103, 104]. Since the sample studied in this work is intrinsic or p-doped, it is probable that the sample was grown under Bi rich conditions (or at the transition between Bi rich and Te rich conditions) and that Bi_{Te} and V_{Te} are frequently occurring native defects. This hypothesis will be explored further in section 3.3.

3.3 Examining native defects

The topological surface states of 3D TIs may host exotic quantum phenomena when time reversal symmetry is broken [1]. A necessary condition for experimentally realizing these phenomena is that the TI material is intrinsic, meaning that the Fermi level should be inside the band gap. This way, the Dirac surface states dominate the transport phenomena. However, many TIs (among which Bi_2Te_3) are degenerately doped due to naturally occurring crystalline defects. This causes their transport properties to be heavily affected by bulk carriers [5]. Various methods, including nanostructuring, compensation by chemical doping or electric gating and band structure engineering by alloying or realizing p-n junctions [6–10], have been studied as a way to suppress this bulk conduction. The problem with these methods is that they either introduce additional disorder or potential fluctuations which negatively affect the TI surface state mobility [11]. Clear identification and understanding of native defects is thus an essential step in TI research.

Unfortunately, it is difficult to directly visualize and identify individual defects experimentally. Often, one needs a combination of first principles calculations and experiments to understand the material properties [105–107]. By making first principles calculations of the formation energies of native defects, one can construct plausible thermodynamic models of defects. The calculated structural and electronic properties can also be compared with available experimental data. However, the experimental evidence supporting a defect model is usually indirect and can be interpreted in different ways. STM is one of the few techniques which can directly address this issue [11, 108, 109]: one can unambiguously identify the defects in samples by directly comparing atomically resolved STM images to simulated STM images of defect models.

This section is dedicated to examining the native defects of the Bi_2Te_3 sample using STM and STS. In subsection 3.3.1, native defects are catalogued and information about them is gathered through STM and STS. Where possible, the features are identified through comparing STM images of them with both density functional theory (DFT) based simulations performed by Dr. Dmitry Muzychenko of the Scanning Probe and Nanoelectronics Laboratory at Lomonosov Moscow State University [71] and results reported in literature [100]. Subsection 3.3.2 entails a statistical analysis to get a better view on the relative frequencies of the defects and their density.

3.3.1 Identifying the native defects of Bi_2Te_3

The first step in identifying these native defects is distinguishing them on topography scans of a typical scale and cataloguing them. In figure 3.7, a STM topography scan of a 70×70 nm^2 area of the sample surface taken at $I = 1$ nA and $V = \pm 700$ mV is shown. The left side of the figure shows imaging of the empty surface states, while the right side depicts the filled surface states. On this scan, seven separate defect types are visible and labelled. Another scan of the same size at $I = 0.5$ nA and $V = \pm 700$ mV (see figure 3.8) reveals three more defects. There are two defects that are only resolved at lower energies. They are marked in figure 3.9, which also has an area of 70×70 nm^2 and measurement parameters of $I = 0.8$ nA and $V = \pm 200$ mV. From the measurements performed for this work, twelve native defects can be distinguished. Having categorized these defects, the rest of this subsection focuses on trying to identify their origin.

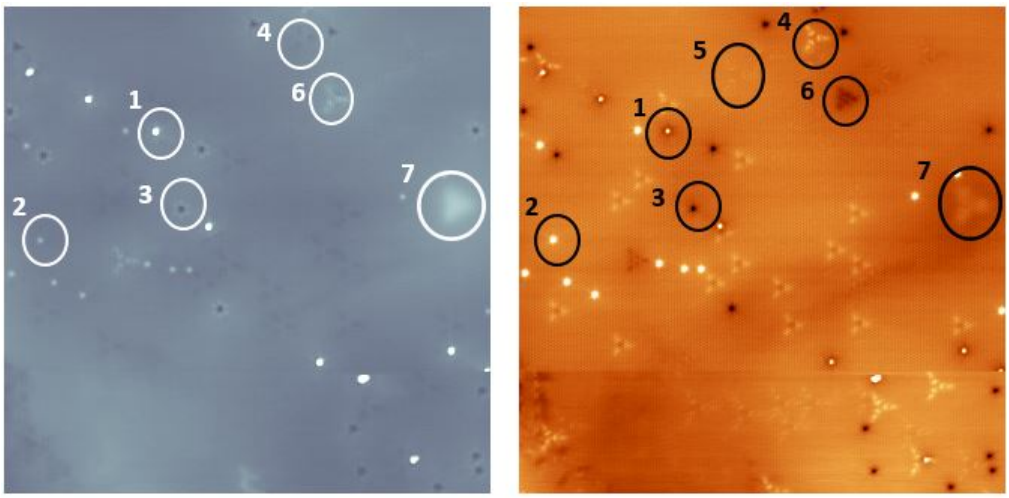

Figure 3.7: 70×70 nm^2 STM topography image of the Bi_2Te_3 surface at $I = 1$ nA and (left) $V = +700$ mV (right) $V = -700$ mV. There are seven separate visible defects.

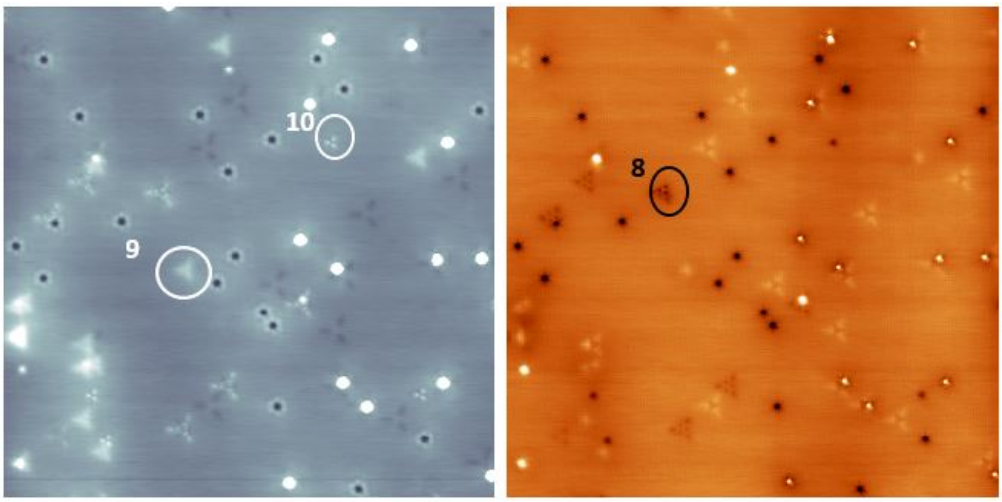

Figure 3.8: 70×70 nm^2 STM topography image of the Bi_2Te_3 surface at $I = 0.5$ nA and (left) $V = +700$ mV (right) $V = -700$ mV. Three more defects can be distinguished.

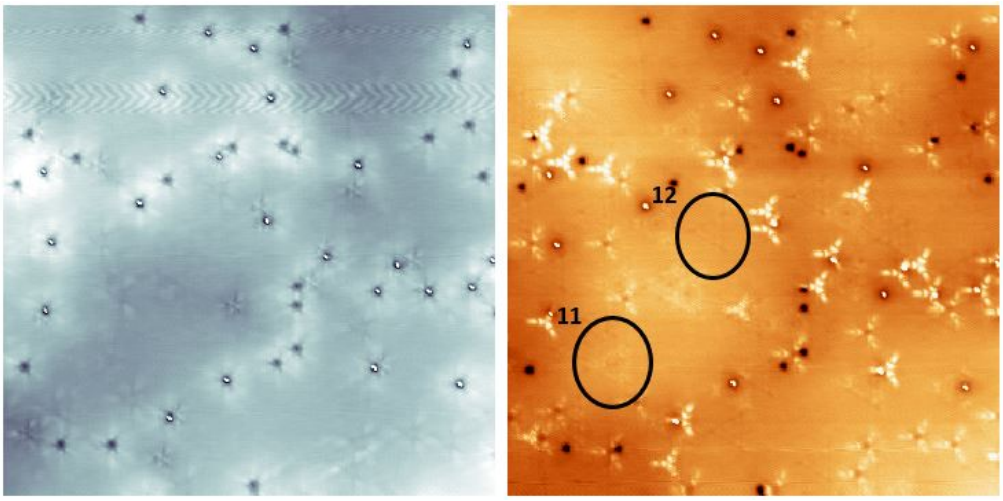

Figure 3.9: 70×70 nm^2 STM topography image of the Bi_2Te_3 surface at $I = 0.8$ nA and (left) $V = +200$ mV (right) $V = -200$ mV. Two more defects are distinguished.

Native defect 1

Native defect 1 is a protrusion on the surface, as seen from atomic-scale imaging shown in figure 3.10. By taking height profiles (see figure 3.11), the height of the defect in the empty and filled states is determined to be 2.3 ± 0.1 Å and 70 ± 3 pm respectively. None of the images simulated using DFT seem to match this defect topography and so the defect is examined further.

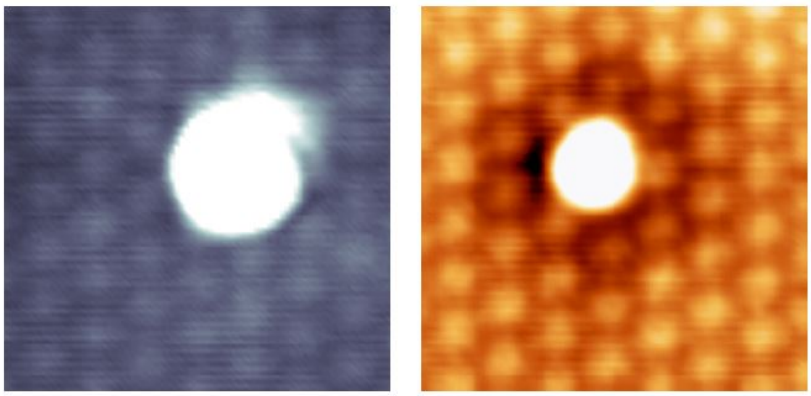

Figure 3.10: 3.2×3.3 nm^2 STM topography image of the Bi_2Te_3 surface at $I = 1$ nA. The left image was taken at $V = +700$ mV while the right one was taken at $V = -700$ mV.

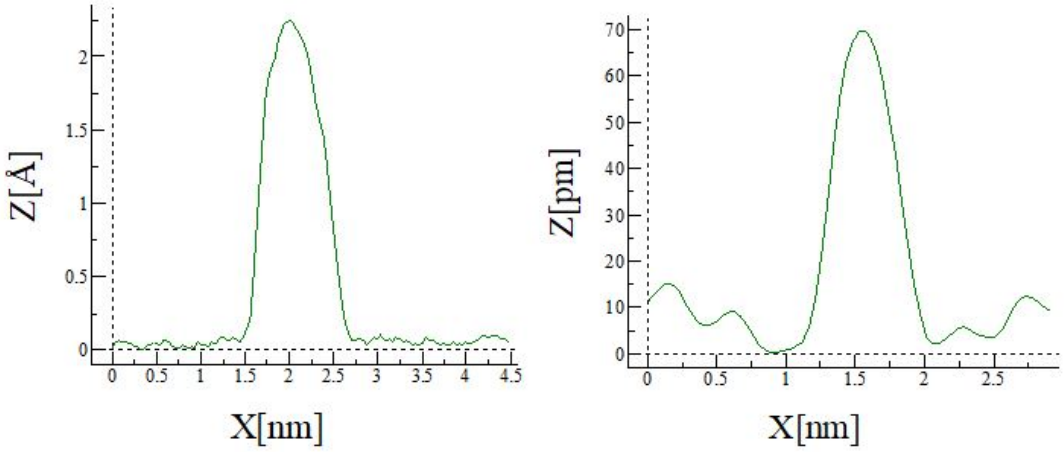

Figure 3.11: Height profile along defect 1 taken at $I = 1$ nA for (left) the empty states with $V = +700$ mV and (right) the filled states with $V = -700$ mV.

To gain more information about this defect, spectroscopy measurements in different bias ranges are performed. Single point spectroscopy taken on top of defect 1 reveals a peak in the LDOS at a voltage of 0.39 V (see figure 3.12c). The conductance at this defect is much larger than at the background of the bare surface (see figure 3.12b). This is confirmed by $\mathrm{d}I/\mathrm{d}V$ spectra recorded along the blue dotted line along defect 1, over a distance of 8.2 nm in figure 3.12a, shown in figure 3.12d. Figure 3.12e presents a 2D visualization of these spectra, where whiter regions correspond to a higher LDOS, while darker regions correspond to a lower LDOS. Single point spectroscopy for a larger bias range (1 to 6 V) is shown in figure 3.13. The LDOS spectra are measured as $\mathrm{d}Z/\mathrm{d}V$ instead of $\mathrm{d}I/\mathrm{d}V$ since these measurements were performed with a closed feedback loop, resulting in a constant current I. The points where spectroscopy is taken are indicated with crosses; two green crosses for defect 1, blue crosses for everything else. From this figure, it is clear that the

spectroscopy of defect 1 shows an additional peak around $V = 1.25$ V and a shift in the vacuum level.

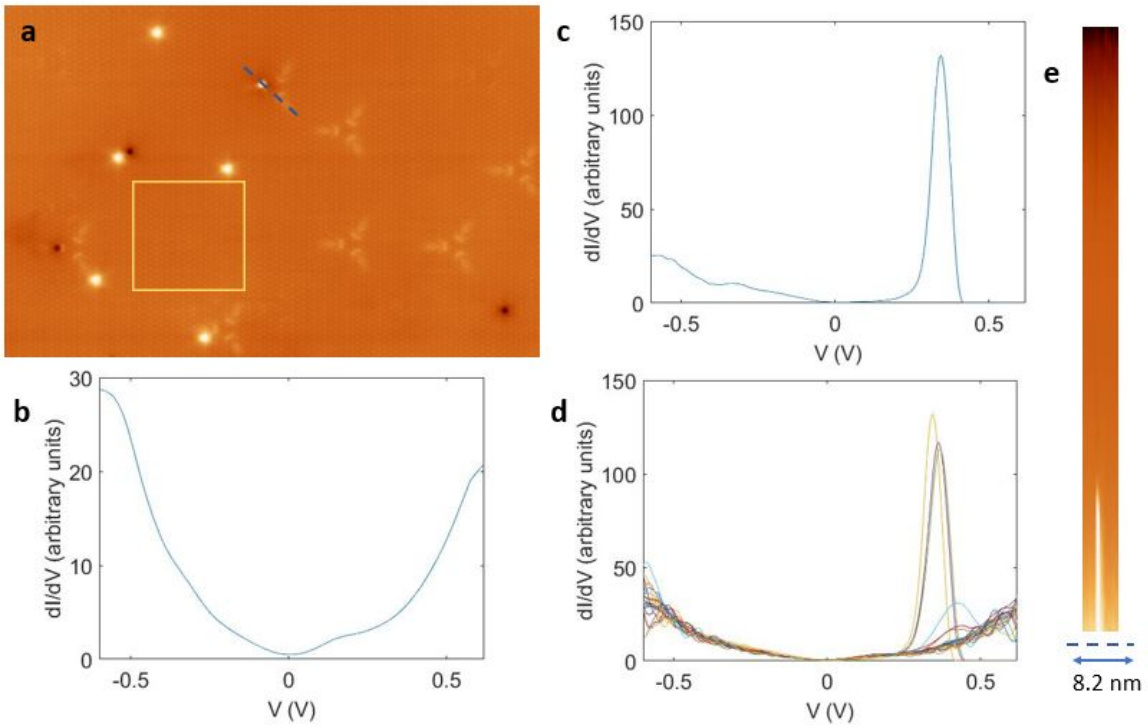

Figure 3.12: (a) Topography image of size about 40×25 nm^2 at $I = 1.2$ nA and $V = -500$ mV. (b) $\mathrm{d}I/\mathrm{d}V$ spectrum, averaged over the area indicated with a yellow rectangle in (a), which has dimensions 10×10 nm^2. (c) Single point spectroscopy taken on top of defect 1. (d) Numerical $\mathrm{d}I/\mathrm{d}V$ spectra recorded along the blue dotted line in (a), which is 8.2 nm long. (e) 2D representation of the $\mathrm{d}I/\mathrm{d}V(V)$ spectra taken along the blue line.

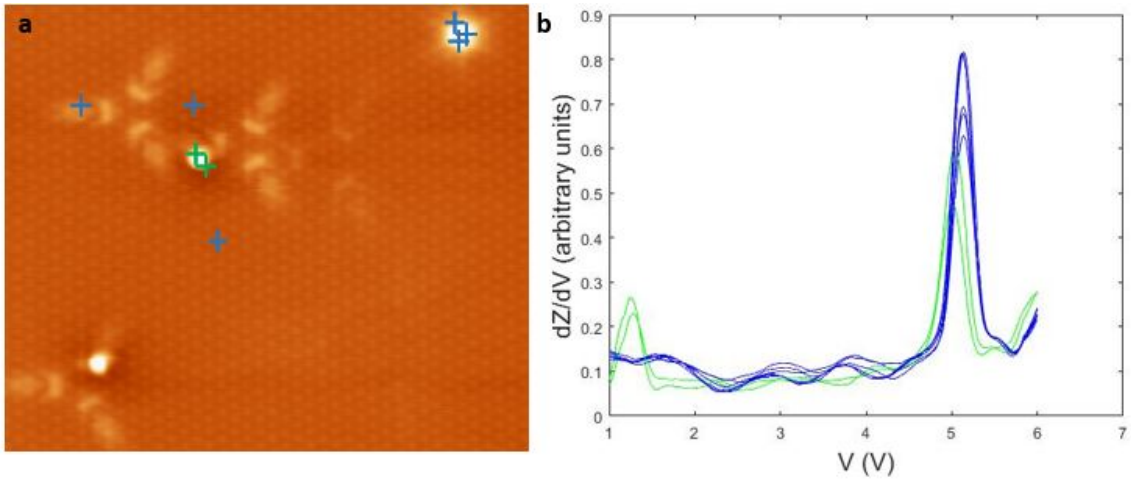

Figure 3.13: (a) Topography image of size about 20×15 nm^2 at $I = 1$ nA and $V = -350$ mV. (b) Single point spectroscopy taken at the points indicated by crosses in (a). Green crosses are on top of defect 1, blue crosses are not.

Moreover, sequential STM images (shown in figure 3.14) show that feature 1 is mobile

and can be removed by the STM tip. The images at bias voltages of $V = \pm 550$, ± 500 and ± 450 mV follow each other directly. In the following scans at $V = \pm 400$ and ± 350 mV, the STM tip interacts with the defect. This tip-defect interaction thus happens at the biases at which a discrete peak occurs in the spectroscopy of this defect. After the interaction, the image at $V = \pm 300$ mV is recorded. In this image, defect 1 is no longer visible: it has been removed by the STM tip. This demonstrates that this defect is a surface adatom.

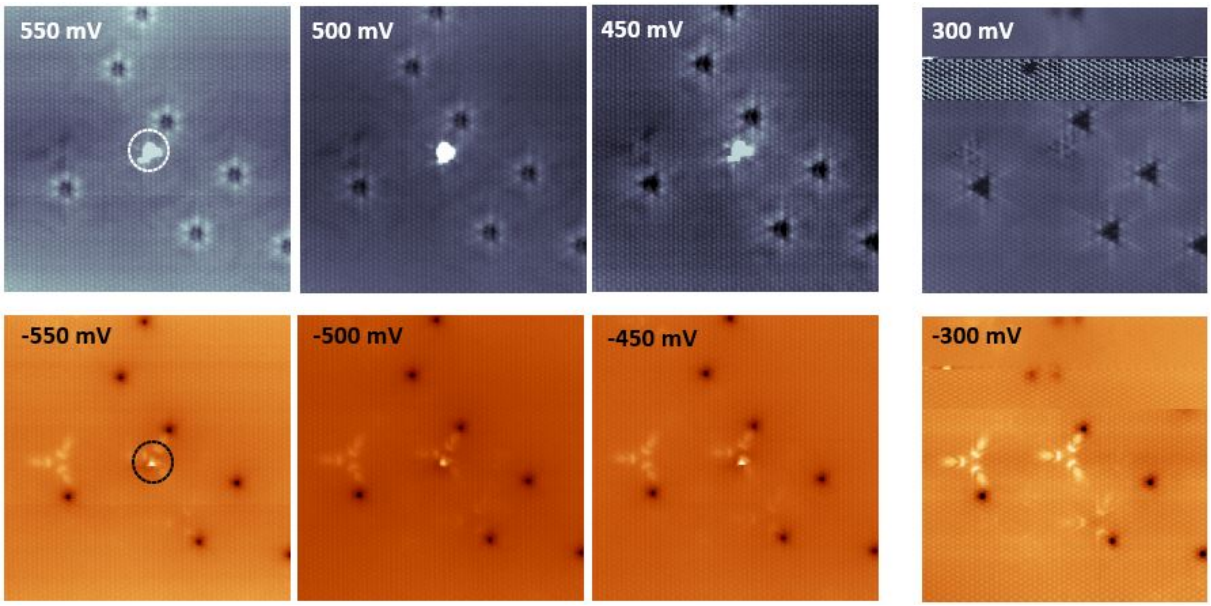

Figure 3.14: Sequential 24×24 nm^2 STM topography images of the Bi_2Te_3 surface at ± 550 mV, ± 500 mV and ± 450 mV. Feature 1 (indicated in the first image by a circle) is seen to be mobile. Then the tip interacts with the feature and a few scans later, the image at $V = \pm 300$ mV is recorded. It appears to be the case that the tip moves the feature and is being modified in the process. The last image reveals that the removal of the feature results in an unperturbed surface.

The origin of the defect is not obvious. One possibility is that this feature is an impurity. Another is that feature 1 is an intercalated tellurium atom which is exposed after cleavage. If this second hypothesis is correct, feature 1 would be a tellurium interstitial between QLs. To shed light on the origin of this defect, Auger electron spectroscopy is performed. These results are discussed in subsection 3.4.1.

Native defect 2

As illustrated by height profiles taken along it (figure 3.15), the second defect also appears higher than its surroundings. The defect height in the empty states is 36 ± 1 pm, while it is 93 ± 1 pm in the filled states. Defect 1 and 2 can thus be distinguished from each other by their different heights and electronic properties. This defect is not mobile and so it is not unreasonable to assume the defect could be explained as a bismuth atom substituting a tellurium atom at the first atomic layer. To further examine this hypothesis, STM images of this defect are compared with images simulated by DFT calculations for a bismuth atom substituting a tellurium atom in the first atomic layer (the top atomic layer of the

top QL), and this for both empty and filled states. The comparison is shown in figure 3.16. Calculation and experiment seem to agree rather well and so defect 2 can be identified as **a bismuth atom substituting a tellurium atom at the first atomic layer**.

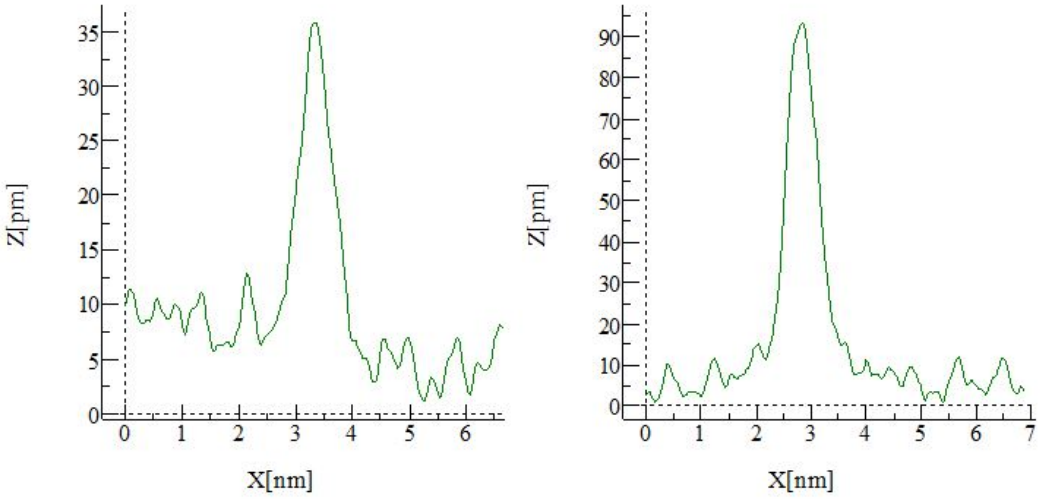

Figure 3.15: Height profile along feature 2 taken at $I = 1$ nA for (left) the empty states with $V = +700$ mV and (right) the filled states with $V = -700$ mV.

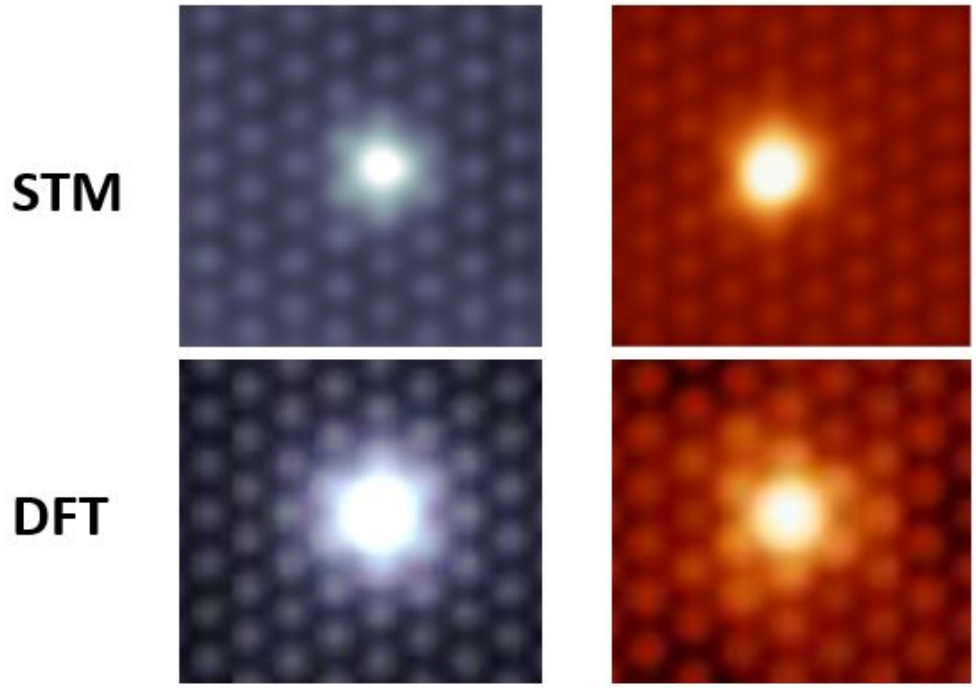

Figure 3.16: (top) 3.4×3.3 nm^2 STM topography image of the Bi_2Te_3 surface at $I = 1$ nA. The blue image is taken at $V = +700$ mV while the orange one is measured at $V = -700$ mV. (bottom) DFT simulations of a bismuth atom sitting at a tellurium site at the first atomic layer, with empty states in blue and filled states in orange color [71].

Native defect 3

Native defect 3 on the other hand, is a depression of the surface. It is thus not unreasonable to consider a tellurium vacancy in the first atomic layer as possible identification of this defect. In figure 3.17, the comparison between atomic resolution STM images of this defect and images of a tellurium vacancy at the first atomic layer simulated using DFT calculations is shown for both empty and filled states. The agreement in the filled states is excellent while that in the empty states is quite close.

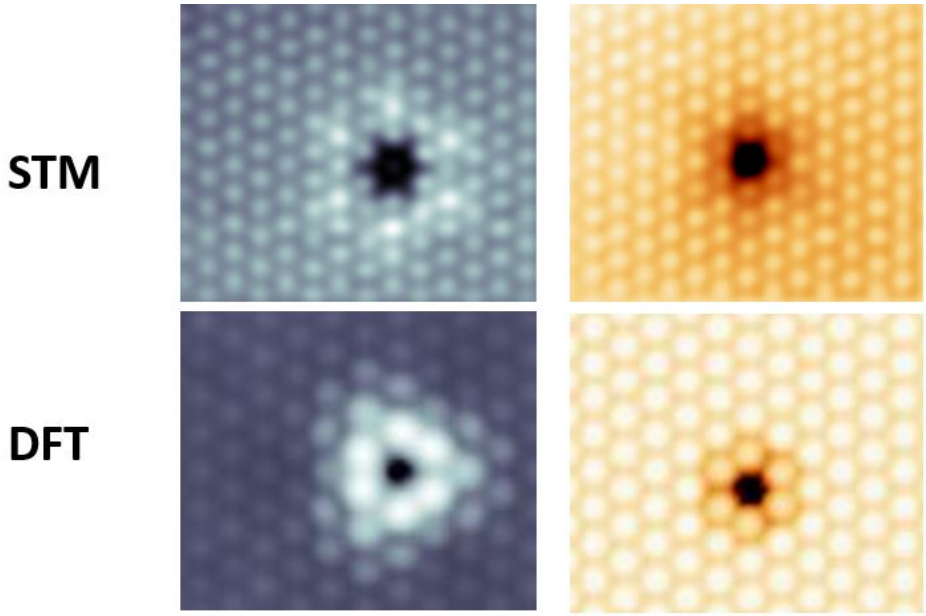

Figure 3.17: (top) 5.4×4.6 nm^2 STM topography image of the Bi_2Te_3 surface at $I = 1$ nA. The blue image is measured at $V = +700$ mV while the orange one is taken at $V = -700$ mV. (bottom) DFT simulations of a tellurium vacancy at the first atomic layer, with empty states in blue and filled states in orange color [71].

In order to gain a better understanding, the empty states of the defect are studied for different applied voltages. In figure 3.18, STM images of feature 3 at $V = 500$ mV, $V = 300$ mV and $V = 100$ mV are compared to simulations of a tellurium vacancy at the first atomic layer. This information from other energies makes it possible to say feature 3 is **a tellurium vacancy at the first atomic layer**.

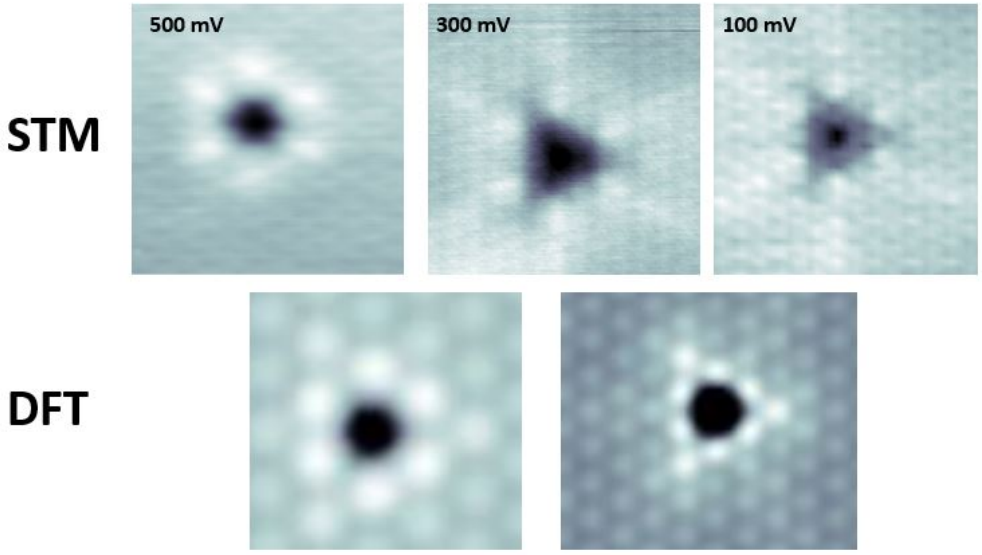

Figure 3.18: (top) STM topography image of the Bi_2Te_3 surface of size (left) 5.3×5.6 nm^2 at $I = 2$ nA and $V = 500$ mV, (middle) 5.2×5.3 nm^2 at $I = 1.5$ nA and $V = 300$ mV and (right) 5.7×5.9 nm^2 at $I = 15$ nA and $V = 100$ mV. (bottom) DFT simulations of a tellurium vacancy at the first atomic layer [71].

Native defect 4

Native defect 4 is one of several triangular defects. Atomic resolution images of it are shown in figure 3.19, for empty (blue) and filled (orange) states.

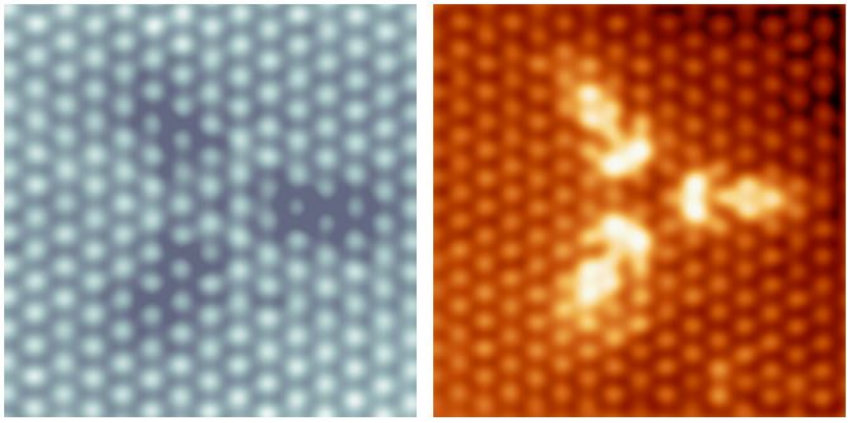

Figure 3.19: 6.4×6.4 nm^2 STM topography image of the Bi_2Te_3 surface at $I = 1.2$ nA. The blue image is measured $V = +700$ mV while the orange one is measured at $V = -700$ mV.

For this defect, none of the simulations matched the STM images. There has been however a work by Dai *et al.*, which was successful in classifying several native defects in Bi_2Se_3 [100]. Since Bi_2Te_3 and Bi_2Se_3 have the same QL structure, it is reasonable to assume both crystals have similar defects. In figure 3.20, the STM scan of defect 4 in the filled states is compared to both experimental and simulated STM images of a selenium vacancy at the

fifth atomic layer measured at $V = -600$ mV from this work. The agreement between these images suggests that native defect 4 is **a bismuth atom substituting a tellurium atom at the fifth atomic layer**.

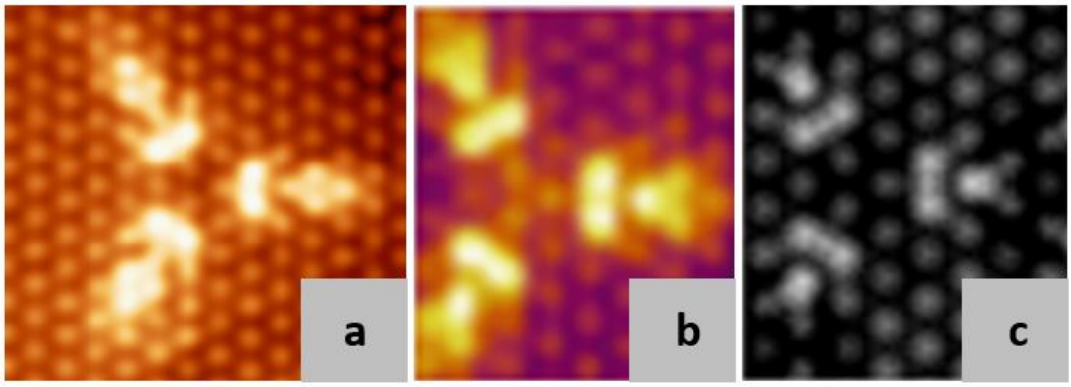

Figure 3.20: (a) 6.4×6.4 nm^2 STM topography image of the Bi_2Te_3 surface at $I = 1$ nA and $V = -700$ mV. (b) and (c) Experimental (b) and simulated (c) STM images of a native defect in Bi_2Se_3: a bismuth atom substituting at selenium atom at the fifth atomic layer measured at $V = -600$ mV. Images (b) and (c) are taken from [100].

Native defect 5

Native defect 5 is also a triangular defect, but is more difficult to resolve than native defect 4, especially in the empty states. Topography images of this defect at $V = \pm 700$ mV, $V = \pm 500$ mV and $V = \pm 300$ mV are shown in figure 3.21 for both filled and empty states. The resolution at the filled states is better than that at the empty states.

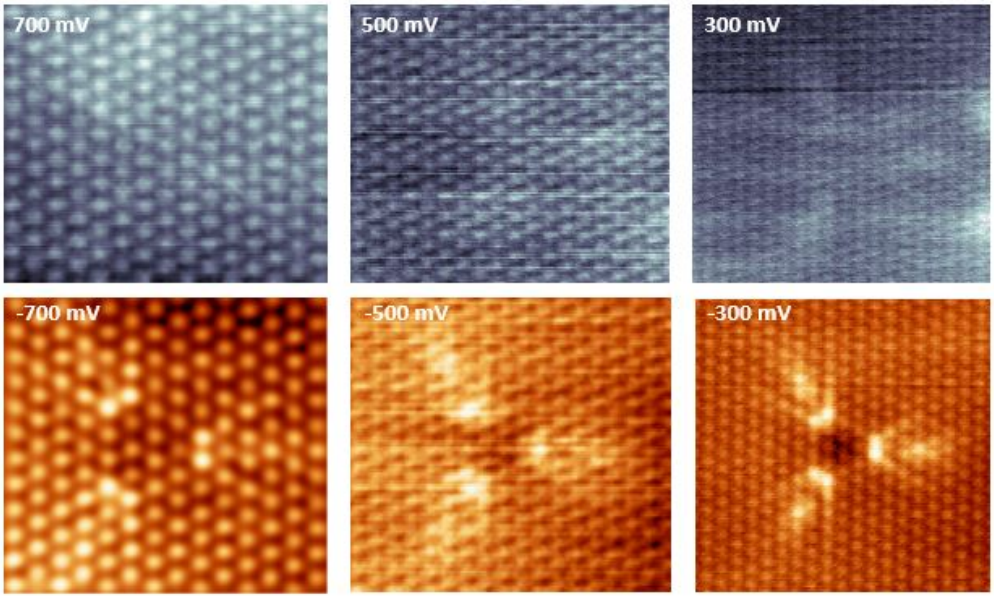

Figure 3.21: STM topography images of the Bi_2Te_3 surface (left) of size 5.2×5.6 nm^2 at $I = 1$ nA and $V = \pm 700$ mV, (middle) of size 7.4×6.4 nm^2 at $I = 2$ nA and $V = \pm 500$ mV, (right) of size 7.9×7.9 nm^2 at $I = 1.5$ nA and $V = \pm 300$ mV.

These STM images do not form a match with any of the DFT based simulated images. Because of this, the work on Bi_2Se_3 by Dai *et al.* is consulted again. In figure 3.22, the comparison of the STM scan of defect 5 at $V = -700$ mV with both experimental and simulated STM images of a bismuth atom at a selenium site at the sixth atomic layer (this is the first atomic layer of the second QL) at $V = -600$ mV from this work is shown. These three images look similar and so one can suggest that defect 5 is **a bismuth atom substituting a tellurium atom in the sixth atomic layer** (this is the first atomic layer of the second QL).

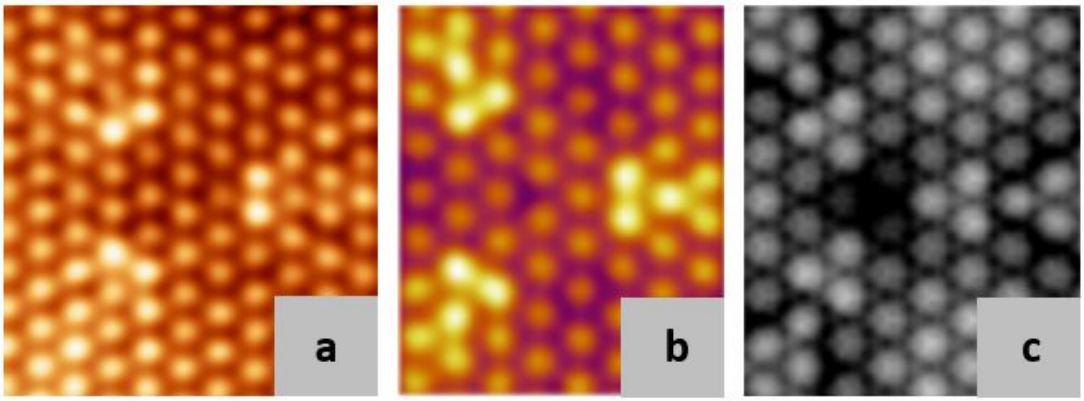

Figure 3.22: (a) 5.2×5.2 nm^2 STM topography image of the Bi_2Te_3 surface at $I = 1$ nA and $V = -700$ mV. (b) and (c) Experimental (b) and simulated (c) STM images of a native defect in Bi_2Se_3: a bismuth atom substituting at selenium atom at the sixth atomic layer measured at $V = -600$ mV. Images (b) and (c) are taken from [100].

Native defect 6

Figure 3.23 shows atomic resolution STM images of native defect 6 for both empty (blue) and filled (orange) states.

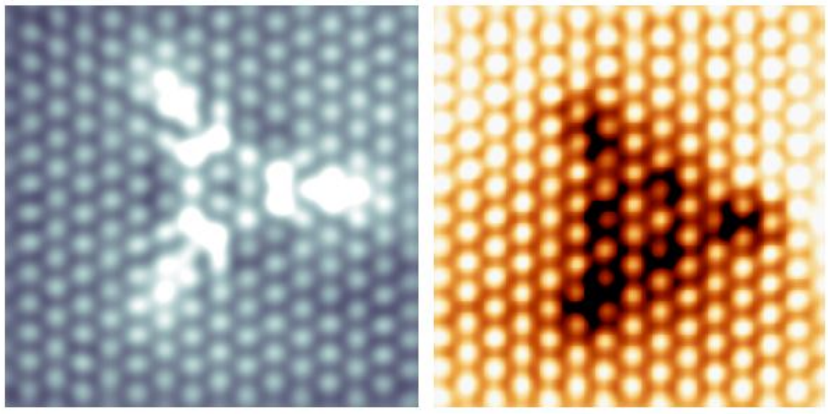

Figure 3.23: 6.2×6 nm^2 STM topography image of the Bi_2Te_3 surface at $I = 1$ nA. The blue image is measured at $V = +700$ mV while the orange one is measured at $V = -700$ mV.

These STM images do not correspond to any of the simulated images. Because of this, native defect 6 is compared with the results of Dai *et al.* once again. In figure 3.24, the

STM scan of defect 6 in the filled states is compared to both experimental and simulated STM images of a selenium vacancy at the fifth atomic layer measured at $V = -700$ mV from this work. These three images look similar and so one can suggest that defect 6 is **a tellurium vacancy at the fifth atomic layer**.

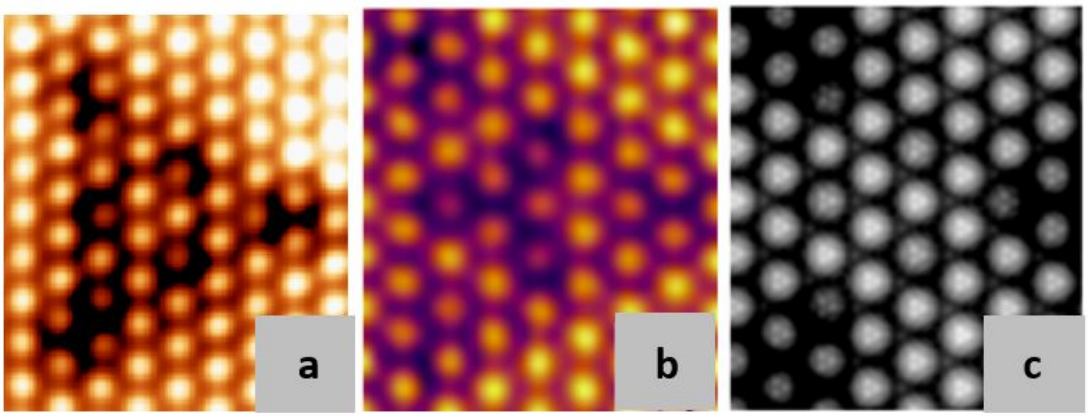

Figure 3.24: (a) 6.2×6 nm^2 STM topography image of the Bi_2Te_3 surface at $I = 1$ nA and $V = -700$ mV. (b) and (c) Experimental (b) and simulated (c) STM images of a native defect in Bi_2Se_3: a selenium vacancy at the fifth atomic layer measured at $V = -700$ mV. Images (b) and (c) are taken from [100].

Native defect 7

In figure 3.25, one can see atomic resolution STM images of native defect 7 for both empty (blue) and filled (orange) states. For this defect no match with DFT simulations was found (yet) and to the best of our knowledge, there is no work in literature which could shed light on this defect's origins. This defect remains unidentified.

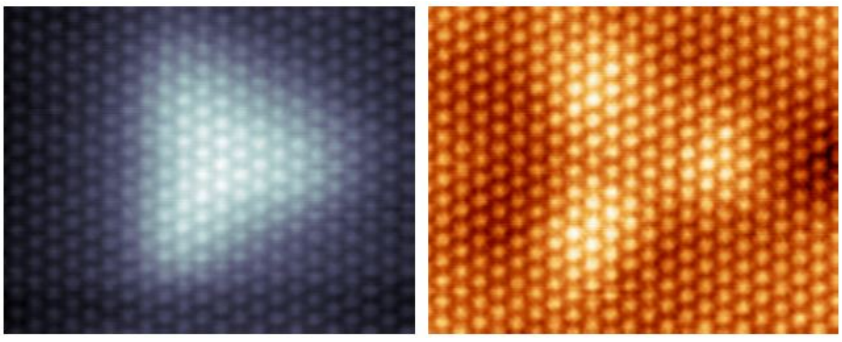

Figure 3.25: 8.9×7.1 nm^2 STM topography image of the Bi_2Te_3 surface at $I = 1$ nA. The blue image is measured at $V = +700$ mV while the orange one is measured at $V = -700$ mV.

Native defect 8

STM images of native defect 8 are shown together with images simulated by DFT calculations for a tellurium vacancy at the third atomic layer in figure 3.26. From the excellent agreement between experiment and calculation, native defect 8 can be concluded to be **a tellurium vacancy at the third atomic layer**.

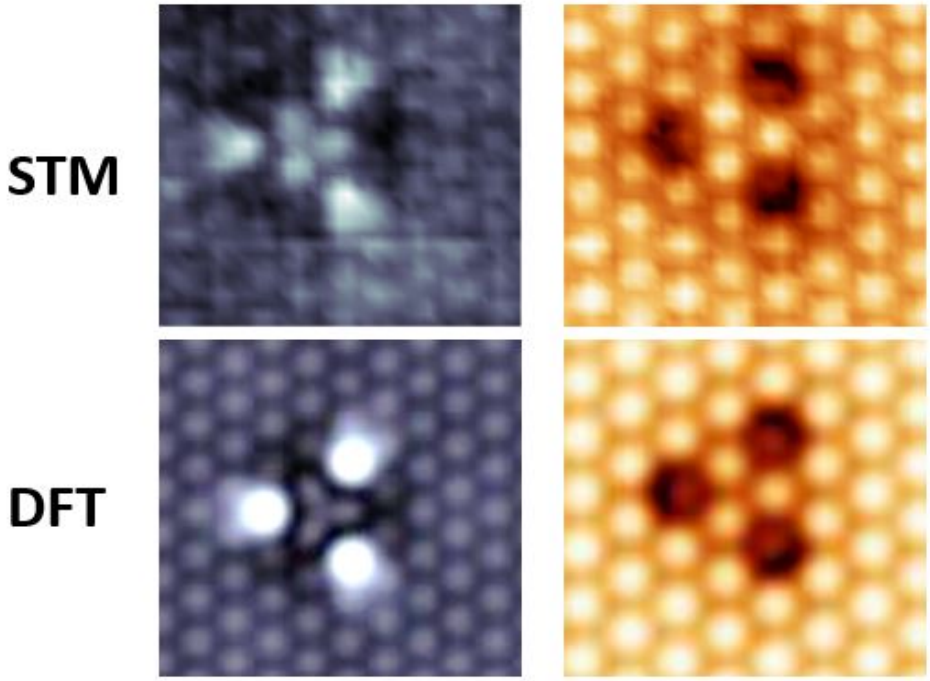

Figure 3.26: (top) 3.9×3.1 nm^2 STM topography image of the Bi_2Te_3 surface at $I = 1.5$ nA. The blue image is measured at $V = +500$ mV while the orange one is measured at $V = -500$ mV. (bottom) DFT simulations of a tellurium vacancy at the third atomic layer, with empty states in blue and filled states in orange color.

Native defect 9

Figure 3.27 shows atomic resolution STM images of defect 9 for both empty (blue) and filled (orange) states. No match between these STM images and any of the simulated images was found. Due to this, the work performed by Dai *et al.* is consulted once more. In figure 3.28, the STM scan of defect 9 in the empty states is compared to both experimental and simulated STM images of an intercalated selenium atom between the fifth and sixth atomic layer measured at $V = 500$ mV from this work. These three images look similar and so one can suggest that native defect 9 is **an interstitial tellurium atom in the van der Waals gap between the first and second quintuple layer**. One of the hypotheses for the origin of defect 1 is that defect 1 could be an interstitial like this which appears on the top of the first atomic layer after cleaving.

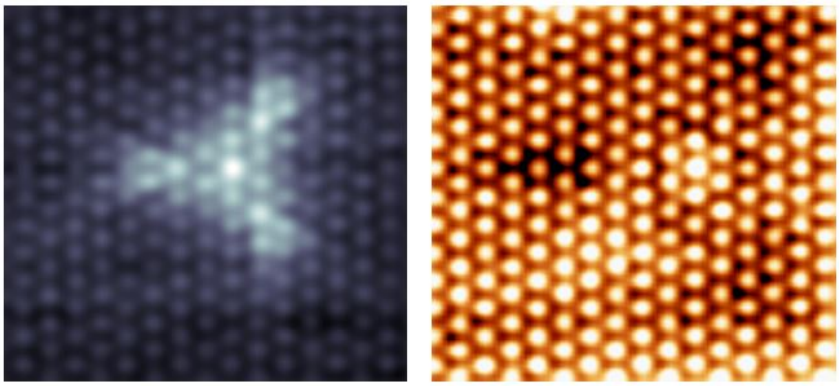

Figure 3.27: 5.3×5.9 nm^2 STM topography image of the Bi_2Te_3 surface at $I = 1.2$ nA. The blue image is measured at $V = +500$ mV while the orange one is measured at $V = -500$ mV.

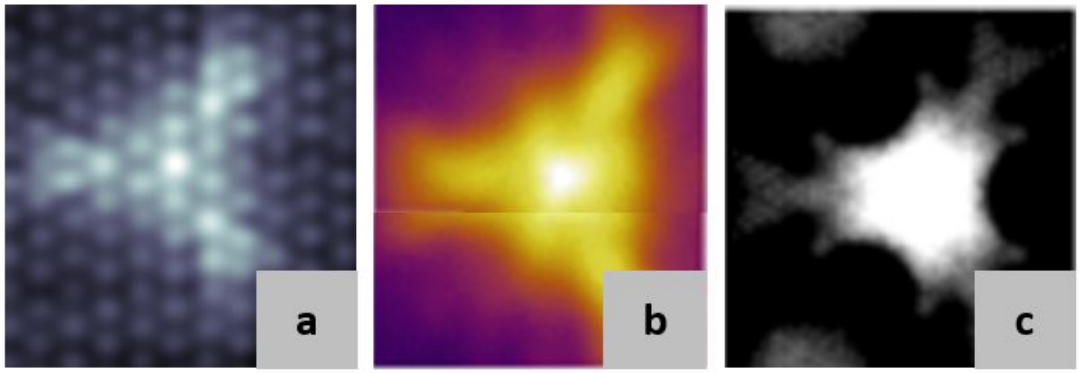

Figure 3.28: (a) 5.3×5.9 nm^2 STM topography image of the Bi_2Te_3 surface at $I = 1.2$ nA and $V = 500$ mV. (b) and (c) Experimental (b) and simulated (c) STM images of a native defect in Bi_2Se_3: an intercalated selenium atom between the fifth and sixth atomic layer measured at $V = 500$ mV. Images (b) and (c) are taken from [100].

Native defect 10

Figure 3.29 shows STM images of native defect 10 and images simulated by DFT calculations for a tellurium atom sitting at a bismuth site at the second atomic layer. The experiment and simulation are very similar: defect 10 can be concluded to be **a tellurium atom substituting a bismuth atom at the second atomic layer**.

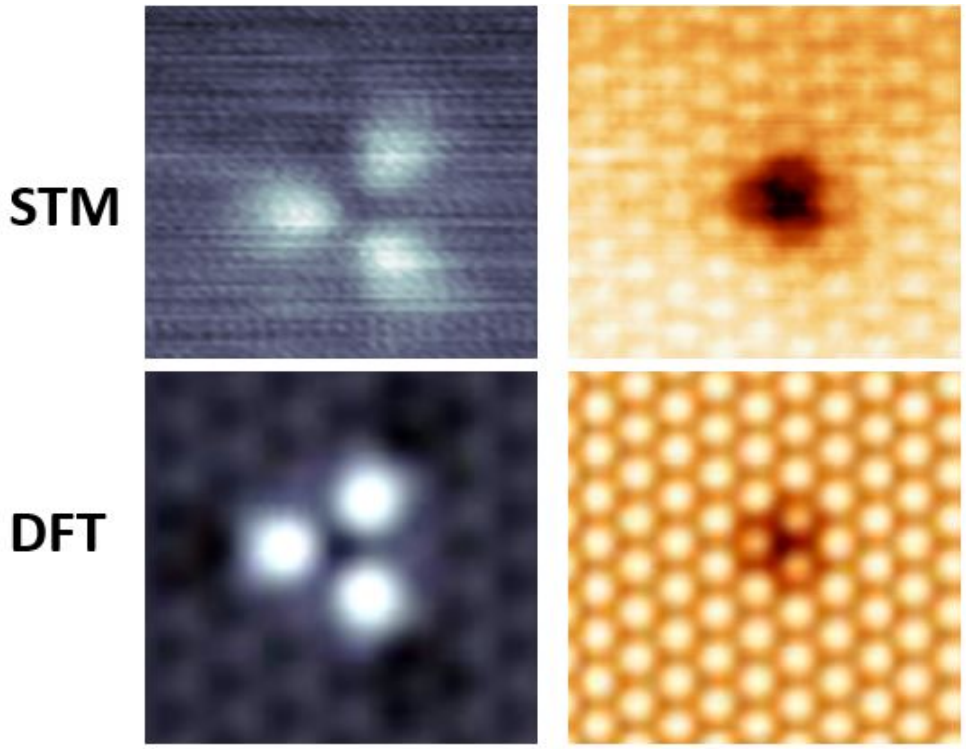

Figure 3.29: (top) 3.6×3.2 nm^2 STM topography image of the Bi_2Te_3 surface at $I = 0.5$ nA. The blue image is taken at $V = +700$ mV while the orange one is measured at $V = -700$ mV. (bottom) DFT simulations of a tellurium atom substituting a bismuth atom at the second atomic layer, with empty states in blue and filled states in orange color.

Native defect 11

Native defect 11 is only visible at voltages with magnitude of $V = 200$ mV or below. It is resolved at the filled states, but not visible in the empty states, as shown in figure 3.30. This defect's topography does not match any of the simulated images and as far as we know, there is no work in literature that can shed light on its origins. This defect remains unidentified.

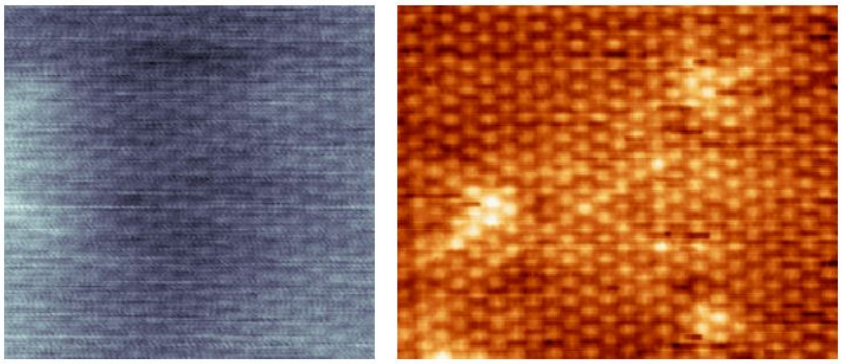

Figure 3.30: 6.4×7.6 nm^2 STM topography image of the Bi_2Te_3 surface at $I = 0.5$ nA. The blue image is taken at $V = +100$ mV while the orange one is taken at $V = -100$ mV.

Native defect 12

Native defect 12 is only visible at voltages with magnitude of $V = 300$ mV or below. Like defect 11, it is resolved at the filled states, but not visible in the empty states (see figure 3.31). No agreement with any of the simulated images was found and as far as we know, this defect cannot be identified from literature. This defect remains unidentified.

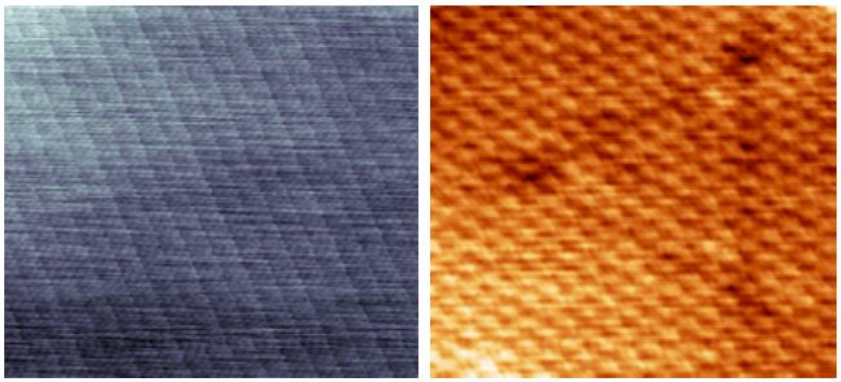

Figure 3.31: 8.3×7.6 nm^2 STM topography image of the Bi_2Te_3 surface at $I = 0.8$ nA. The blue image is measured at $V = +200$ mV while the orange one is measured at $V = -200$ mV.

Summary of the identifications

In table 3.1 below, a recapitulation of the identification process is shown. Vacancies of element A at atomic layer j are annotated as $V_{A,j}$. An atom of element A substituting one of element B at atomic layer j is represented by $A_{B,j}$. An interstitial of element A between layers j and j+1 is represented as $A_{i,j+0.5}$. Defects that are not (yet) identified are shown as question marks. In subsection 3.2.2, it was predicted that tellurium vacancies (V_{Te}) and bismuth atoms substituting tellurium atoms (Bi_{Te}) would be the most frequently occurring native defects because they have the lowest formation energies. This appears to be the case when looking at the identification of the defects. However, one should take into account the relative frequencies of these defects to make this claim. This is done through a statistical analysis.

Table 3.1: Identification of the native defects. The first row denotes the native defects by their labels. In the second and third row, small STM topography images of the defects in the empty and filled states are shown. The last row summarizes the origins of the defects.

1	**2**	**3**	**4**	**5**	**6**	**7**	**8**	**9**	**10**	**11**	**12**
											
											
?	$Bi_{Te,1}$	$V_{Te,1}$	$Bi_{Te,5}$	$Bi_{Te,6}$	$V_{Te,5}$	?	$V_{Te,3}$	$Te_{i,5.5}$	$Te_{Bi,2}$	?	?

3.3.2 Statistical analysis

In order to estimate the relative frequency of the native defects, the number of occurrences of each defect is counted for several STM topography scans of the same size (70×70 nm^2). The results are shown in table 3.2, where a / means that the particular defect does not appear in that scan of the topography. It is necessary to use data from multiple scans since differing resolution of scans can cause one to not count a defect that is there. Scans at different bias voltages are used. Not all defects are equally frequent: only the first five occur regularly.

Table 3.2: The frequency of the different defects on 15 different scans of size 70×70 nm^2 for different bias voltages.

	1	**2**	**3**	**4**	**5**	**6**	**7**	**8**	**9**	**10**	**11**	**12**
700 mV	13	4	19	8	/	5	8	1	1	4	/	1
	9	12	13	22	10	/	2	1	/	/	/	/
	24	4	22	20	/	/	/	2	/	/	/	/
	18	2	27	15	/	/	/	/	/	/	/	/
	9	8	21	22	/	/	/	/	/	/	/	/
500 mV	11	3	15	19	14	2	3	/	1	/	3	/
	26	3	27	20	11	/	/	/	/	/	/	/
	26	/	19	18	/	/	/	/	/	/	/	/
400 mV	16	/	25	20	6	/	/	/	/	/	1	/
	17	3	28	18	/	/	/	/	/	/	2	/
300 mV	11	1	21	23	27	/	/	/	/	/	/	/
	21	/	18	24	10	/	/	/	/	/	/	/
200 mV	22	/	20	25	14	5	/	/	/	/	/	/
	11	1	21	22	23	/	/	/	/	/	/	/
100 mV	13	5	19	29	/	5	8	1	6	1	/	2

It is of course possible that some defects were overlooked in the counting process. Moreover, the resolution of scans differs and different energies allow to probe different defects. All of this introduces some uncertainty on the counted frequencies. To get a more accurate estimate, the average of these frequencies $\bar{f}$ is taken. This is done for the first five defects only, since the other ones are not as frequent and so there is not enough data for reliable statistics. The error on the average has a 68 % confidence interval and is given by the standard deviation, calculated through

$$f = \bar{f} \pm \sqrt{\frac{\sum_i^N (f_i - \bar{f})^2}{N(N-1)}}, \tag{3.2}$$

where f_i is one of the frequencies of a certain defect out of table 3.2, $\bar{f}$ is the average frequency for this defect and $N = 15$. The result is shown in table 3.3.

Table 3.3: The average frequency in number per scan of 70×70 nm^2 for the five most abundant defects (defect 1 - defect 5).

defect	**1**	**2**	**3**	**4**	**5**
average	16 ± 2	3 ± 1	21 ± 1	20 ± 1	8 ± 2

From this, one can see that native defect 3 (a tellurium vacancy at the first atomic layer) and 4 (a bismuth atom substituting a tellurium atom at the fifth atomic layer) are the most frequent. One can conclude that V_{Te} and Bi_{Te} are the most frequently occurring defects. This was predicted in subsection 3.2.2 based on their formation energies.

3.4 Additional surface analysis

This section describes surface analysis used to further characterize the sample. The STM and STS data concerning defect 1 were not sufficient to identify it. One possible hypothesis is that the defect is an impurity. To check this, Auger electron spectroscopy (AES) measurements were performed. The results are discussed in subsection 3.4.1. During the AES measurements, the surface order was also investigated using low energy electron diffraction (LEED). Subsection 3.4.2 shows the findings of these measurements.

3.4.1 Auger electron spectroscopy analysis

As mentioned in subsection 2.2.3, the Bi_2Te_3 sample is cleaved in ambient. A first series of Auger measurements is performed before the sample is sputtered. The resulting spectrum is shown in figure 3.32.

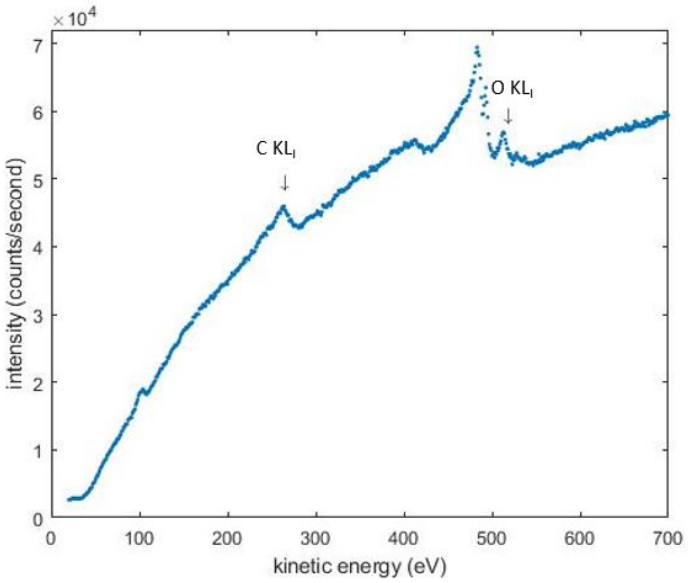

Figure 3.32: Auger spectrum of the Bi_2Te_3 sample after cleaving, but before sputtering. Peaks due to carbon and oxygen are identifiable, indicating that the surface is contaminated due to air exposure.

The most prominent peak around 480 eV is attributed to tellurium core transitions. Peaks due to carbon and oxygen are identified. This is explained by the short exposure to air of the crystal after being cleaved, which results in the formation of oxide layers [110]. This oxidation process degrades the sample surface, which makes it difficult to characterize ex-situ. Due to this, different methods have been proposed to protect the crystal surface for ex-situ experiments. One of these methods is removing the oxidized layer (and other contaminants) by using Ar^+ ion sputtering [111]. This is implemented in the setup used in this work. Another Auger spectrum was obtained after sputtering and is shown in figure 3.33. In it, peaks attributed to the core levels of bismuth and tellurium are distinguishable. No other elements are detected. From this, no real conclusions can be made about the origin of defect 1. It is possible that it is an impurity, but that the Auger setup detection limit for this element is not sensitive enough to detect it, especially when the defect has a low density. From table 3.3, it is known that there are on average 16 ± 2 defects per area of 70×70 nm^2. From this, one can estimate the number surface density as $(33 \pm 4) \times 10^2$ defects of this kind per square micron. However, it is also possible that this defect 1 is indeed an intrinsic defect. This scenario could point to the defect being a tellurium interstitial between QLs, which finds itself at the surface after cleaving.

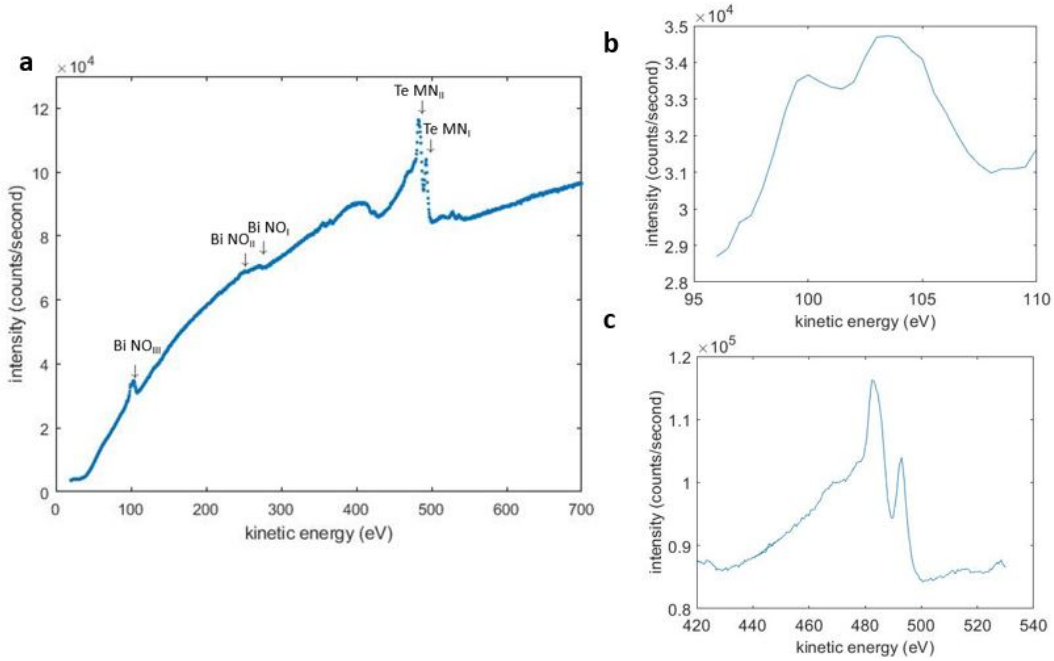

Figure 3.33: (a) Auger spectrum of the Bi_2Te_3 sample after cleaving and sputtering. Peaks due to bismuth and tellurium are identifiable, but no other element is detected. (b) A zoomed in view of the Auger peaks due to bismuth core transitions around 100 eV. (c) A zoomed in view of the Auger peaks due to tellurium core transitions around 480 eV.

To investigate further, one could try examining the sample using a scanning Auger microscope (SAM). Scanning Auger microscopy produces elemental maps of the surface by scanning the electron beam over the sample and selecting specific Auger peaks. It provides the spatial distribution of each element at the sample surface with high lateral resolution ($\sim$ 50 nm) and is thus a suitable technique for this problem [112].

3.4.2 Low-energy electron diffraction analysis

While the sputtering technique is effective in removing contaminants, the process usually leads to rough or damaged surfaces [113]. This is not really a problem when doing AES because one is interested in the chemical composition rather than the surface roughness. Even so, it is possible to monitor the surface structure using LEED. Figure 3.34a shows a LEED pattern of the Bi_2Te_3 sample acquired at 61 eV, after sputtering. The pattern in it is similar to the one in figure 3.34b, which is the Fourier transform of the sample surface topography measured by STM. In both images, the hexagonal pattern characteristic of the crystal surface threefold symmetry is clearly visible. Since the STM image was measured after cleaving in UHV (so without damaging the surface order) while the LEED pattern was taken after sputtering, this demonstrates that an intact Bi_2Te_3 surface is exposed after sputtering. After being damaged by the sputtering process, the surface order is restored.

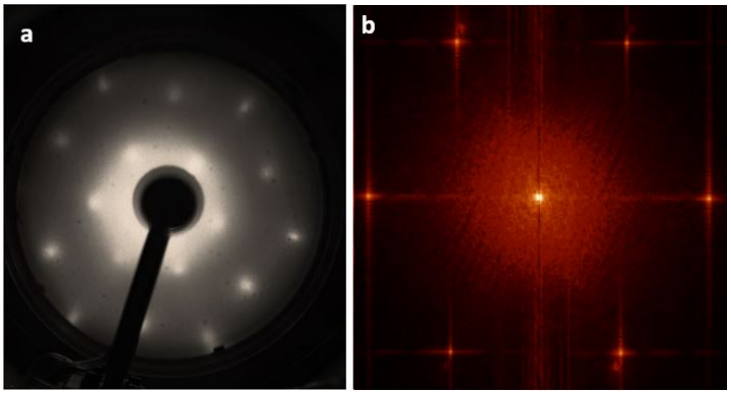

Figure 3.34: (a) LEED pattern of Bi_2Te_3 (61 eV) after sputtering. (b) Fourier transform of the topography of the bare sample surface measured by STS at $V = 700$ mV. Both show the six-fold rotational symmetry of the crystal lattice.

3.5 Scattering events

The aim of this section is to study the scattering events at the surface of the Bi_2Te_3 crystal through quasiparticle interference patterns (QPIs) (see subsection 2.1.3). Subsection 3.5.1 discusses Fourier transforms for several conductance maps measured through STS for different energies. In subsection 3.5.2, the information gathered from these Fourier transforms is used to obtain the linear dispersion of the massless Dirac fermions of the surface states. Using this dispersion, the fermion velocity v_F and the Dirac point energy E_D are estimated.

3.5.1 Quasiparticle interference patterns

Figure 3.35 shows a 70×70 nm^2 STM topography image of the surface and its corresponding $\mathrm{d}I/\mathrm{d}V$ map, obtained in the manner discussed in subsection 2.1.2. The conductance map shows spatial modulations known as QPIs, resulting from scattering of the surface electronic states. The QPIs deviate from the underlying atomic structure because of the defect distribution at the surface. The patterns are dominated by modulations with a

wavelength of ~ 3 nm when measuring at $V = 400$ mV. From this figure, it is clear that defect 1 and defect 3 (a tellurium vacancy) are the main scattering centres. This is not very surprising since these defects occur at or on the top atomic layer.

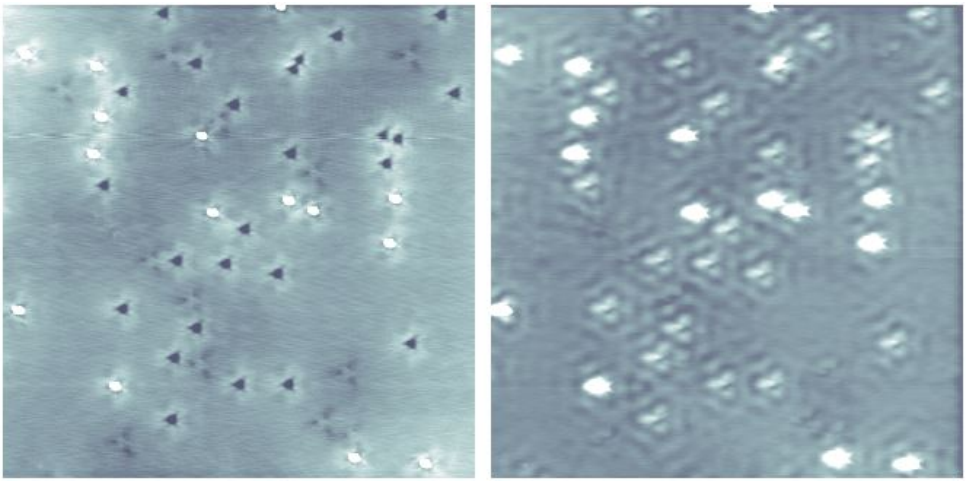

Figure 3.35: (left) 70×70 nm^2 STM topography image of the Bi_2Te_3 surface at $I = 2$ nA and $V = 400$ mV. (right) The corresponding conductance map, showing the formation of standing waves on the surface.

Since the QPIs are highly periodic, they are better resolved in the Fourier transformed image. The Fourier transforms of conductance maps like the one in figure 3.35 display rich patterns, which have the six-fold rotational symmetry of the underlying lattice and evolve as a function of energy. Moreover, if the size of the triangularly shaped defects is close to the wavelength of the incident electronic wave, this can result in scattering dominated by the defect shape in real space and six-fold symmetry in reciprocal space. These patterns display the allowed scattering wave vectors $\vec{q}$ and the relative intensities for the various scattering processes experienced by the surface state electrons. To gain better understanding about these scattering processes, the conductance map and corresponding Fourier transforms are measured for different bias voltages (and hence different energies). The resulting Fourier transforms are shown in figure 3.36. They appear quite diffuse: this might be explained by relatively few scattering events occurring, resulting in low intensities in the Fourier transforms or by contribution to the standing waves formation from states originating in the bulk. Even so, it is clear that scattering events in the $\bar{\Gamma} - \bar{\mathrm{M}}$ directions are more intense that those in the $\bar{\Gamma} - \bar{\mathrm{K}}$ directions in the bias range from 250 to 400 mV, indicating that the surface states are indeed protected from backscattering, as explained in chapter 1. This might also be the case for other voltages, but the Fourier images at these biases are not clear enough to conclude that. In higher energy ($V = 250$ mV and above) Fourier images, the hexagonal pattern is somewhat warped. This can be understood through the surface band structure of Bi_2Te_3. Constant energy contours (CECs) of the Dirac cone present significant warping caused by a k^3 term originating from cubic Dresselhaus spin-orbit coupling at the surface of rhombohedral crystal systems like Bi_2Te_3 [114]. These CECs can be measured using ARPES, as shown in figure 3.37. Since the Fourier transformation of the conductance map is approximately given by the convolution of the ARPES spectral function at wave vector $\vec{k}$ with that at $\vec{k} + \vec{q}$ averaged over $\vec{k}$ [115], the warping seen in Fourier transforms of conductance maps can be considered

equivalent to those seen in ARPES-measured CECs and thus originating from the band structure.

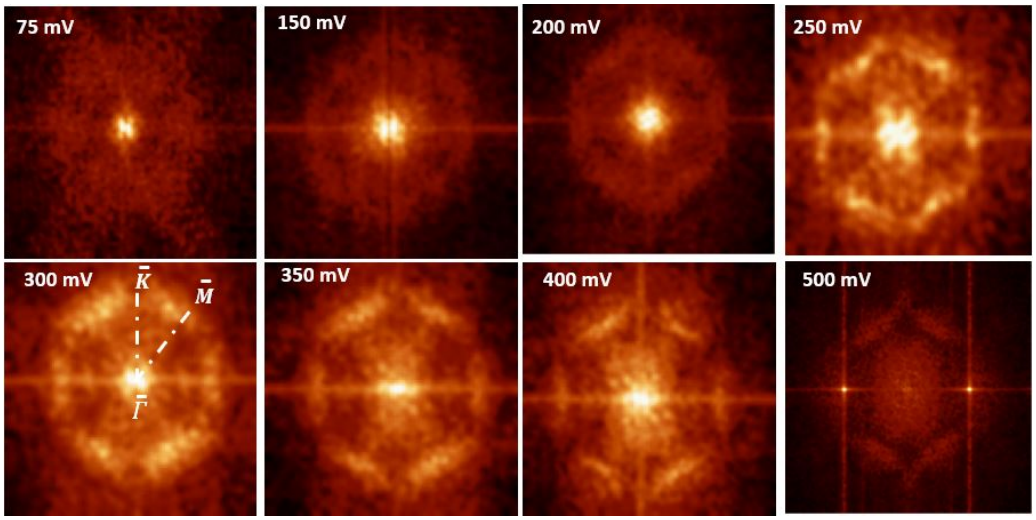

Figure 3.36: The Fourier transforms of conductance maps measured at $V = 75$, 150, 200, 250, 300, 350, 400 and 500 mV. The size of the images is about 1×1 1/nm^2. At $V = 75$, 150 and 200 mV, the Fourier images are quite diffuse and it is difficult to make definite statements. At $V = 250$, 300, 350 and 400 mV, it is clear that scattering in the $\bar{\Gamma} - \bar{\mathrm{M}}$ direction dominates over scattering in the $\bar{\Gamma} - \bar{\mathrm{K}}$ direction, indicating the suppression of backscattering. At voltages at or above $V = 250$ mV, the warped band structure of Bi_2Te_3 is visible.

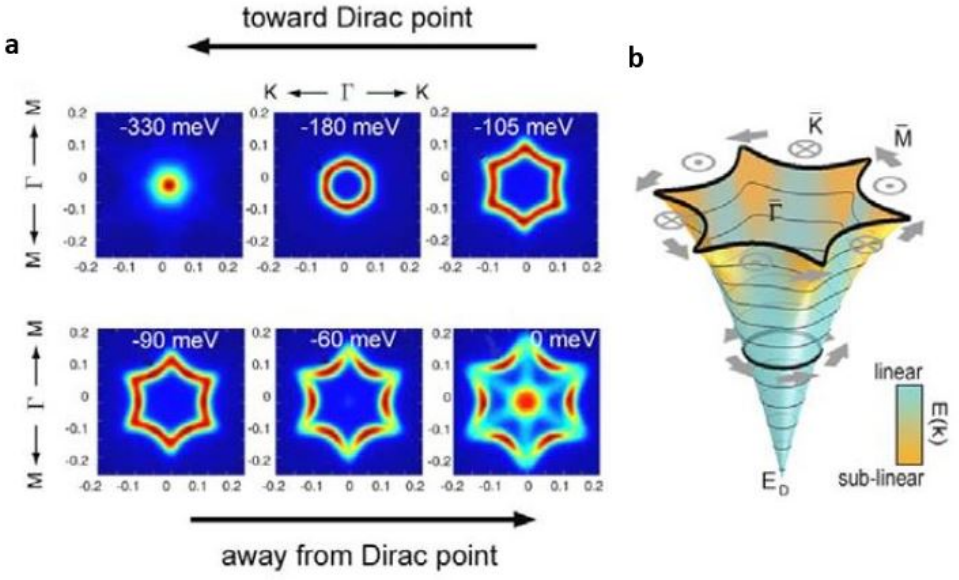

Figure 3.37: (a) ARPES-measured constant energy contours of the surface bands. The energies are with respect to the Fermi energy, and the Dirac point E_D lies at -340 meV. (b) A schematic representation of the surface bands and spin texture of Bi_2Te_3. At $E \sim E_D$+250 meV, the bands turn from conic to hexagonally warped. Figures taken from [57, 83].

3.5.2 Energy dispersion relation of the surface states

From the Fourier transform maps in figure 3.36, one can measure the intensity in the $\bar{\Gamma}-\bar{\mathrm{M}}$ direction. One can determine the component of the scattering wave vector q parallel to the surface by measuring the wavelengths associated with the scattering events in reciprocal space. By doing this for each of the measured Fourier transforms, the energy dispersion of the surface states as a function of q in the $\bar{\Gamma}-\bar{\mathrm{M}}$ direction can be obtained. The result is shown in figure 3.38. The errors on the q-values are determined by the resolution of the Fourier transform images. The best fit to the data (shown as a red line on the figure) demonstrates that the dispersion is indeed linear, as expected for massless Dirac fermions. The dispersion relation is given by

$$E = aq + b,$$

where $a = 230 \pm 42$ meV nm and $b = -260 \pm 90$ meV. The quality of the fit is quantified by an R^2-value of 0.9754.

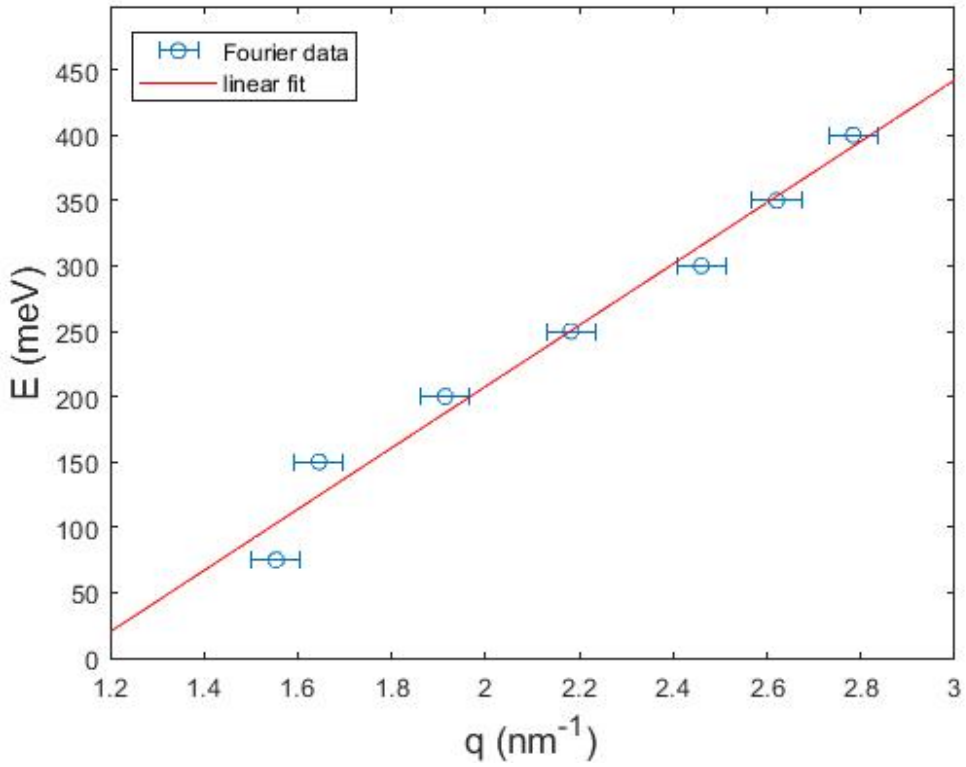

Figure 3.38: The $E(q)$-dispersion in the $\bar{\Gamma}-\bar{\mathrm{M}}$ direction for the bare surface of Bi_2Te_3.

It can be derived from the scattering geometry that $q = \sqrt{3}k$ [64], and so the slope a of the fit can be used to determine the Dirac fermion velocity v_F and the intercept b to estimate the energy of Dirac point E_D.

$$v_F = \frac{1}{\hbar}\frac{\mathrm{d}E}{\mathrm{d}k} = \frac{1}{\sqrt{3}\hbar}\frac{\mathrm{d}E}{\mathrm{d}q} = \frac{1}{\sqrt{3}\hbar}a = (2.1 \pm 0.4) \times 10^5 \text{ m/s},$$
$$E_D = b = -260 \pm 90 \text{ meV}.$$

The retrieved fermion velocity is of the same order of magnitude as that observed by ARPES [57]. Based on the calculated energy dispersion, the native defects of the crystal can influence the electronic band structure by bringing the Fermi level within the energy gap but do not bring the Dirac point out of the valence band, as the $E_D = -260$ meV indicates. This negative value is in agreement with ARPES measurements, which show that even for intrinsic samples the Dirac point still remains buried in the valence band [57]. To make a more reliable estimate, more data of the scattering vector q should be obtained at various energies.

3.6 Chapter summary

This chapter presents the results of the surface characterization of the topological insulator Bi_2Te_3 using STM, STS, AES and LEED.

Topography of the sample surface reveals several defects. The interatomic distance is determined to be $d = 4.5 \pm 0.1$ Å, while the height of a quintuple layer is measured as 1.0 ± 0.1 nm. Upon studying the density of states by area-averaged spectroscopy, one can see the surface state conductance in a $\mathrm{d}I/\mathrm{d}V$ spectrum. The sample appears to be either undoped or slightly p-doped.

When studying the native defects more closely, one can distinguish twelve defect types. Various defects are identified as tellurium vacancies V_{Te}, Bi_{Te} antisites, Te_{Bi} antisites and tellurium interstitial defects Te_i. The most frequent of these defects are tellurium vacancies at the first atomic layer ($V_{Te,1}$) and bismuth atoms substituting tellurium atoms at the fifth atomic layer ($Bi_{Te,5}$). Four native defects could not be identified (yet). One of these unidentified native defects, labelled as defect 1 shows discrete peaks in its density of states and a shift in the vacuum level. This defect is also mobile. To gain more information about defect 1, AES is performed. After sputtering to remove contamination, the resulting spectrum only shows peaks due to transitions in bismuth and tellurium atoms. There are two possible interpretations. In a first interpretation, defect 1 is a defect with a density that is too low to be detected by the Auger setup. In the second interpretation, defect 1 is an intrinsic defect of the crystal. If it is a native defect, it might be a tellurium interstitial (like defect 9) between QLs which finds itself at the surface after cleaving. Further studies with a scanning Auger microscope, as well as DFT based calculations might help in understanding this defect's origins. LEED measurements reveal that after being treated with Ar^+ sputtering, the surface order is restored. The restored surface has the same structure as the in-situ (UHV) cleaved surface measured by STM.

The scattering events occuring at the bare are due to the native defects, with the main scattering centers being ($V_{Te,1}$) and the unidentified defect 1. Scattering in the $\bar{\Gamma} - \bar{\mathrm{M}}$ direction of the surface Brillouin zone dominates over scattering in the $\bar{\Gamma} - \bar{\mathrm{K}}$ direction at some voltages, indicating a suppression of backscattering. At higher energies, the Fourier transforms of the conductance maps are warped, which is attributed to the surface band structure of Bi_2Te_3, which is warped due to a spin-orbit coupling term at the surface. The dispersion relation for the surface states along the $\bar{\Gamma} - \bar{\mathrm{M}}$ direction is linear at the bare surface, as expected for massless Dirac fermions. From the dispersion relation, the Dirac

fermion velocity and the energy of the Dirac point are be estimated. The fermion velocity is in agreement with values determined from ARPES measurements. The negative Dirac point energy at the bare surface indicates that the native defects do not act to bring the Dirac point out of the valence band.

Chapter 4

Cobalt deposition

The surface states of TIs are protected by time reversal symmetry: they are protected from backscattering even in the presence of nonmagnetic disorder. When introducing magnetic impurities, this protection breaks down: since the partial protection from scattering is assured by time reversal symmetry, introducing magnetic impurities is believed to have a notable impact on the allowed scattering processes of the helical surface states. Once the impurity acquires a magnetic moment it can spin-exchange with the incident Dirac particle, and allow for spin-flip induced backscattering. When ferromagnetism can be developed in TIs, this can lead to interesting quantum phenomena like the QAHE, which may result in the development of promising spintronics applications. It is thus not very surprising that magnetically doped TIs have been on the forefront of TI research. While many studies examining magnetic bulk-doping of topological insulators have been performed, magnetic doping at the surface has not been explored as thoroughly, even though it is expected to stronger influence the surface Dirac fermions than the bulk doping [22]. For this reason, atoms of magnetic materials are deposited at the undoped crystal studied in chapter 3 and studied by means of STM and STS.

In this chapter, the deposition of single magnetic cobalt (Co) atoms on the surface of Bi_2Te_3 is investigated by means of low-temperature STM and STS. In the first section 4.1, the deposition itself is described. An overview of the sample surface topography is discussed in section 4.2, after which individual features (native defects or features due to the cobalt atoms) are discussed in section 4.3. Section 4.4 examines scattering events at the sample surface using QPIs.

4.1 Deposition

The cobalt atoms are deposited at room temperature using one of the evaporation cells described in section 2.1.4 for a time of 2 seconds with a flux of 2.5 nA. It is not straightforward to quantify the surface coverage. One could try formulating it in terms of monolayers, but this is difficult since there is no layer by layer growth. Another possibility is to express it using surface number density. This poses its own challenges; one needs to count the deposited atoms, but this is complicated as it is unclear whether observed features are individual atoms or small clusters (this is discussed in section 4.3.1). One can only say that the deposited amount is certainly smaller than one monolayer and otherwise too small to quantify in a reliable way.

4.2 Overview

In this section, the surface after the cobalt deposition is studied on a typical scale of 70×70 nm^2. A STM topography image of the Bi_2Te_3 surface before the atomic cobalt deposition at $I = 1$ nA and $V = \pm 500$ mV is shown in figure 4.1 below. The surface looks comparable to the surface after the atomic deposition (see figure 3.2): the native defects of the bare surface are visible, while new chromium features are also seen.

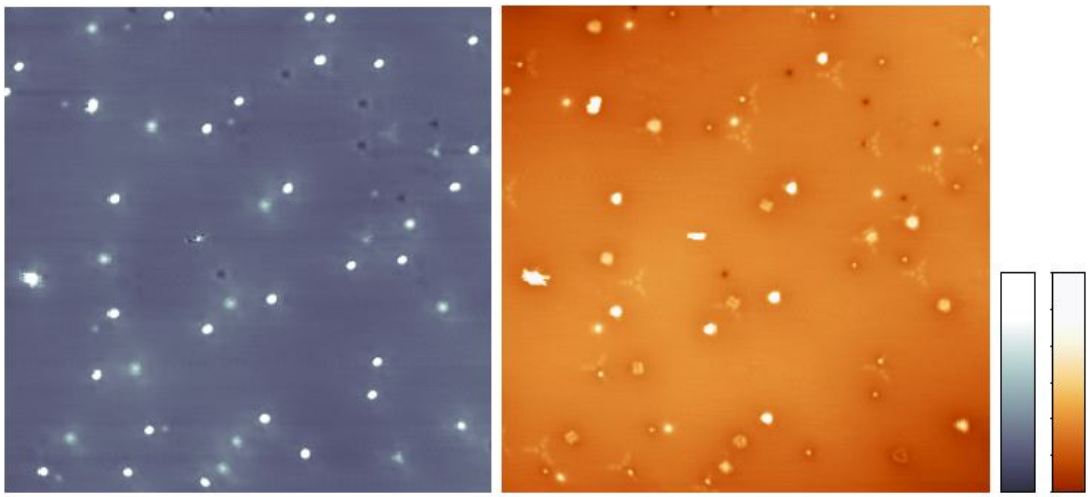

Figure 4.1: 70×70 nm^2 STM topography image of the Bi_2Te_3 surface after atomic cobalt deposition at $I = 1$ nA and (left) $V = +500$ mV (right) $V = -500$ mV.

4.3 Examining native defects and cobalt features

The aim of this section is to study the impact of the atomic cobalt deposition on the surface features using STM and STS. This impact can be twofold: the deposited atoms can interact with the native defects of the bare surface and new features due to the cobalt atoms can arise. Subsection 4.3.1 focuses on features that were not seen on the bare surface. In subsection 4.3.2 a statistical analysis of the most occurring native defects is made and compared with the results from the bare surface.

4.3.1 Cobalt features

After the atomic cobalt deposition, features differing from the native defects can be distinguished. The new features can be divided into two categories. Features in the first category are protrusions on the surface with a spherical shape, while those in the second category are more geometric in structure. This subsection aims to gather more information about them using STM and STS.

Atom and cluster features

Features in the first category are protrusions on the surface with a spherical shape. A small scale topography image of one of these features is shown in figure 4.2.

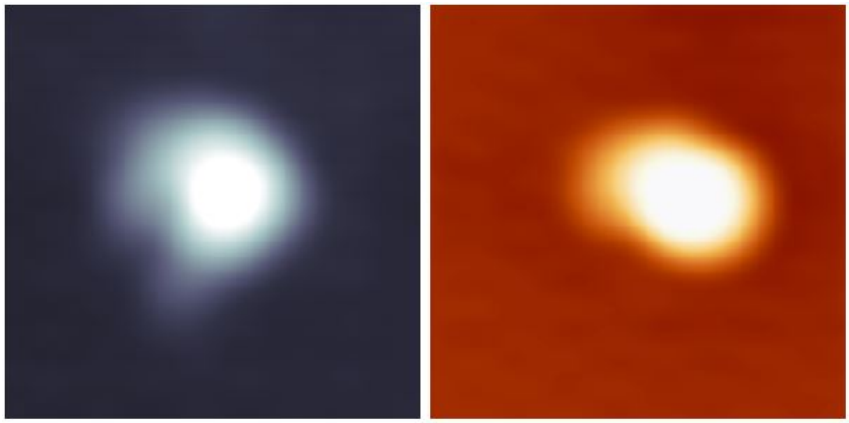

Figure 4.2: 3×3 nm^2 STM topography image of the Bi_2Te_3 surface after atomic cobalt deposition at $I = 2$ nA and (left) $V = +500$ mV (right) $V = -500$ mV.

Imaging after the deposition (see figure 4.3) shows that this kind of feature occurs with different sizes. This is also confirmed by height profiles taken along different features, shown in figure 4.4.

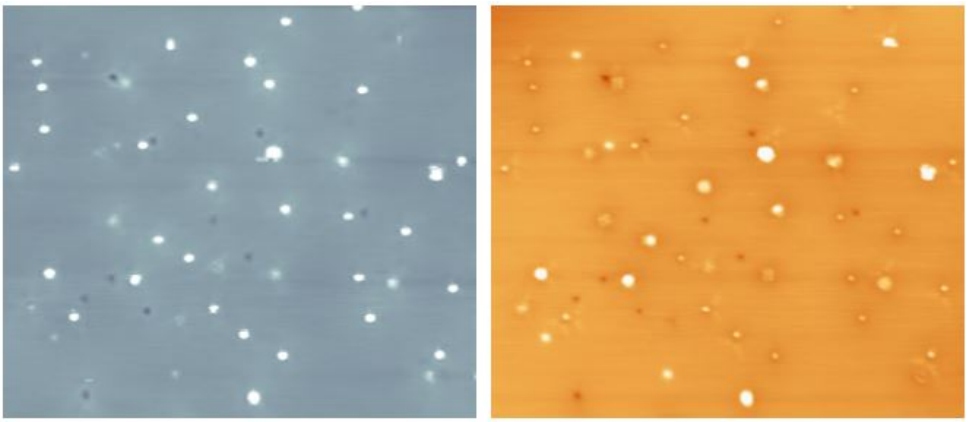

Figure 4.3: 70×60 nm^2 STM topography image of the Bi_2Te_3 surface after atomic cobalt deposition at $I = 2$ nA and (left) $V = +700$ mV (right) $V = -700$ mV.

There are six distinguishable peaks. The first peak has a height of 0.3 ± 0.1 Å (0.3 ± 0.1 Å) in the empty (filled) states. The second peak has a height of 2.4 ± 0.1 Å (1.9 ± 0.1 Å), while the third peak is measured to have 1.8 ± 0.1 Å (2.6 ± 0.1 Å) as height. The height profile reveals a fourth peak with height 0.7 ± 0.1 Å (1.3 ± 0.1 Å) and a fifth peak with height 1.4 ± 0.1 Å (1.6 ± 0.1 Å). The last peak distinguished from this line profile is measured as 0.2 ± 0.1 Å (1.0 ± 0.1 Å). There are only two native defects which are protrusions (native defect 1 and 2). It is difficult to directly compare with the heights determined for these defects in subsection 3.3, since the scans used are taken at different tunneling parameters. That these heights are not necessarily the same can be seen by using the Tersoff-Hamann model (see subsection 2.1.1). However, since there are more than two distinguishable heights, one can say that at least some of the peaks measured after the cobalt deposition are due to the new features. There are several different sizes for this kind of defect. Since the atomic deposition happens at room temperature, the

atoms are mobile: they aggregate and form small clusters of different sizes.

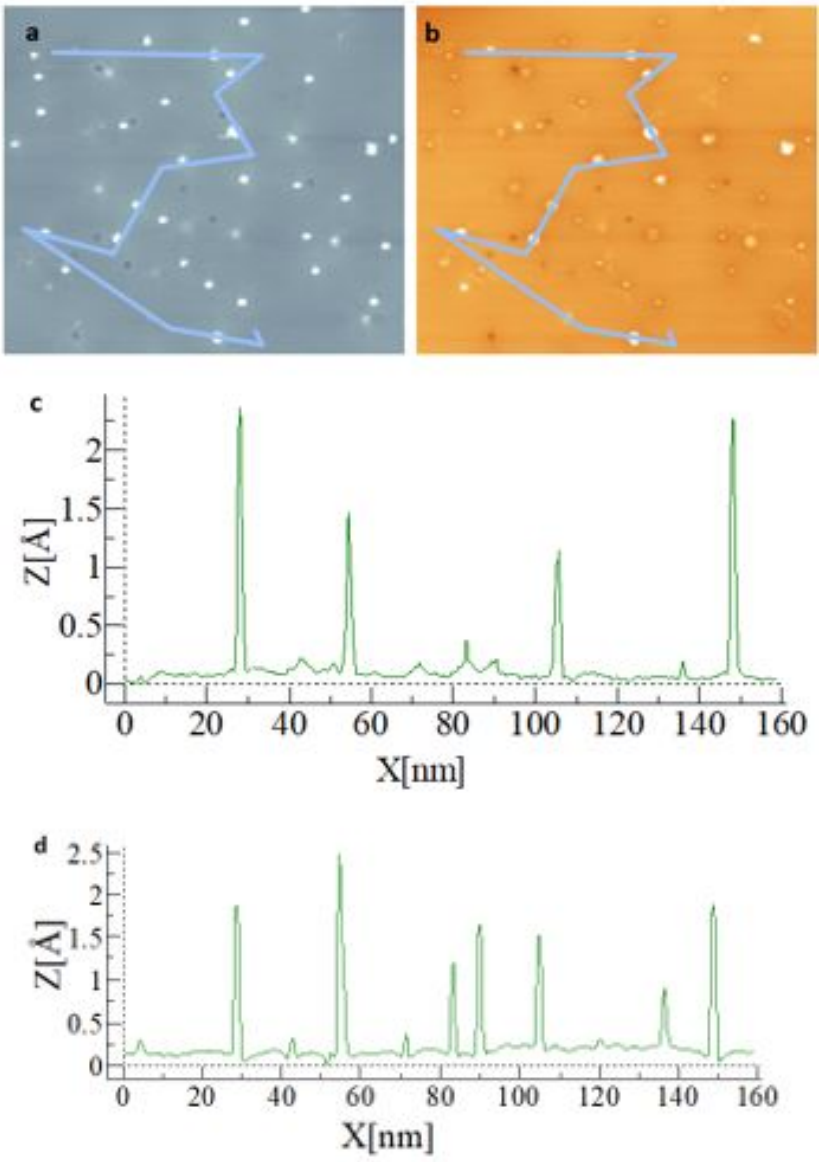

Figure 4.4: (a) and (b) show 70×60 nm^2 STM topography images of the Bi_2Te_3 surface after atomic cobalt deposition at $I = 2$ nA and (a) $V = +700$ mV, (c) $V = -700$ mV. (c) and (d) show the height profiles taken along the surface paths indicated in (a) and (b) respectively.

Geometric features

The first category of features can thus be attributed to cobalt atoms and clusters on the sample surface. The second category is different: instead of spherical shapes, they exhibit geometric structures. The features are believed to arise due to some interaction between the cobalt atoms and the Bi_2Te_3 crystal. Four different features from this second category are distinguished. In what follows, atomically resolved and bias dependent images reveal the topographic signatures of these cobalt features. The comparison of these experimental

data with DFT calculation can provide an understanding of their origin.

Cobalt feature 1. Figure 4.5 shows bias-dependent topography images for the first cobalt feature. The size of the images is around 3×3 nm^2. The scans at ± 50 mV were taken at a tunneling current of $I = 0.5$ nA, while those at ± 100 mV were measured at $I = 2.5$ nA. The tunneling current was $I = 3$ nA for images taken at ± 300, ± 500 and ± 700 mV. The scans at ± 1000 mV were measured at a tunneling current of $I = 2$ nA.

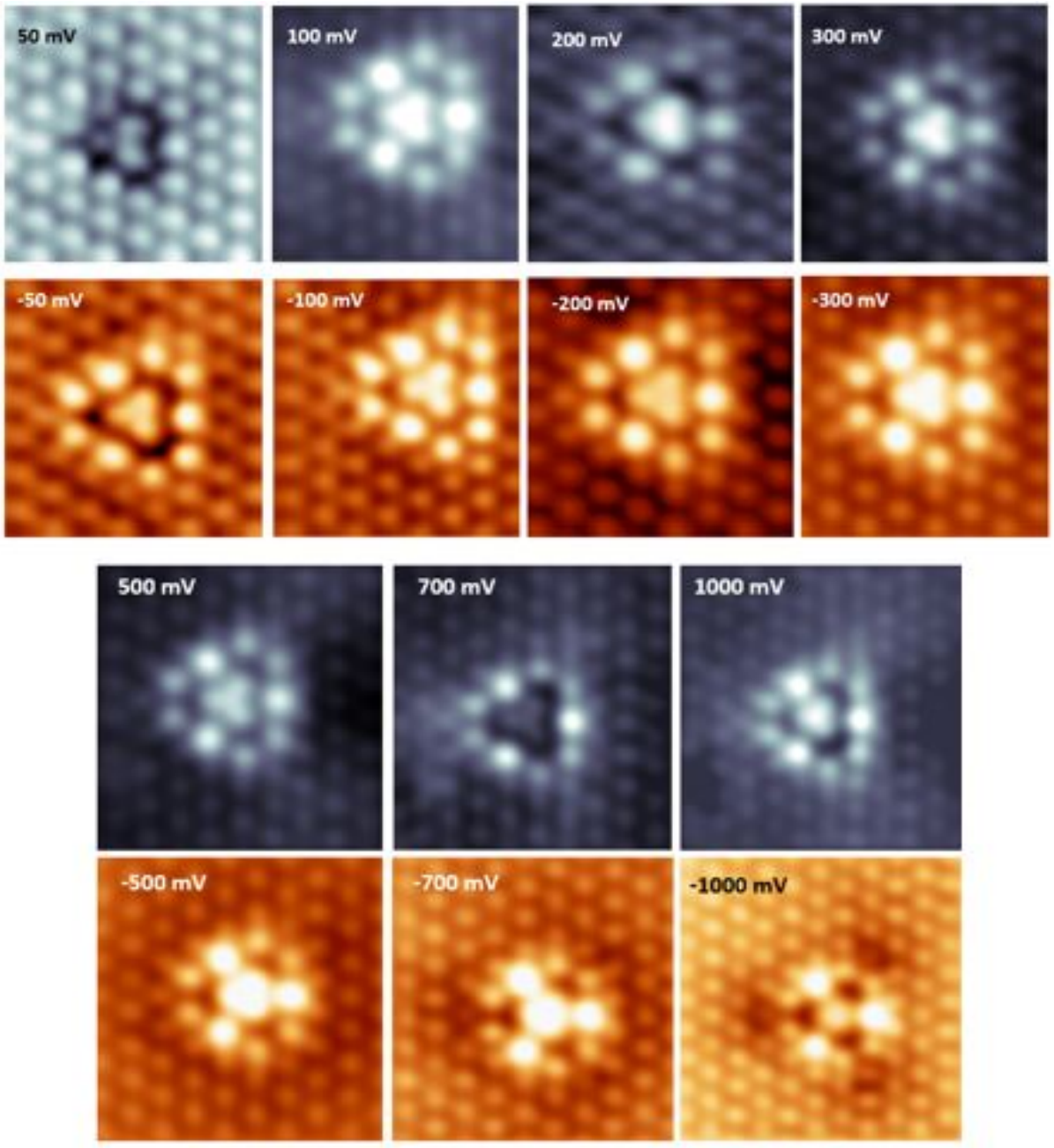

Figure 4.5: Bias-dependent topography images for cobalt feature 1 at $V = \pm 50$, ± 100, ± 200, ± 300, ± 500, ± 700 and ± 1000 mV.

Cobalt feature 2. Figure 4.6 shows bias-dependent topography images for the second cobalt feature. The size of the images is around 3×3 nm^2. The scans at ± 50 mV were taken at a tunneling current of $I = 0.5$ nA, while those at ± 100 mV were measured at $I = 2.5$ nA. The tunneling current was $I = 3$ nA for images taken at ± 300, ± 400, ± 500 and ± 700 mV. The scans at ± 400 and ± 1000 mV were taken at a tunneling current of $I = 2$ nA.

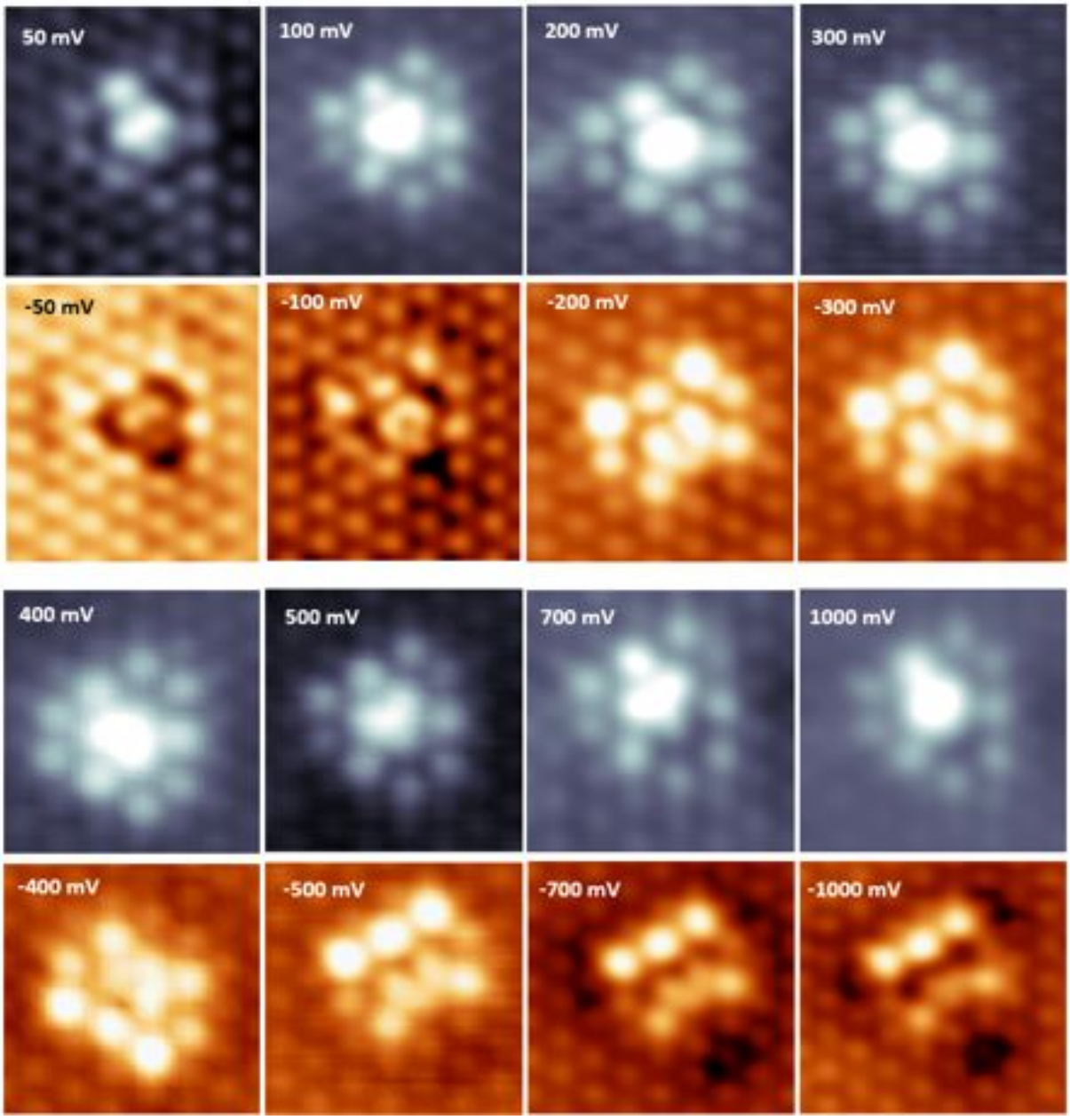

Figure 4.6: Bias-dependent topography images for cobalt feature 2 at $V = \pm 50$, ± 100, ± 200, ± 300, ± 400, ± 500, ± 700 and ± 1000 mV.

Cobalt feature 3. Figure 4.7 shows bias-dependent topography images for the third cobalt feature. The size of the images is around 3×3 nm^2. The scans at ± 50 mV were taken at a tunneling current of $I = 0.5$ nA, while those at ± 100 mV were measured at $I = 1.5$ nA. The tunneling current was $I = 3$ nA for images taken at ± 300, ± 400, ± 500 and ± 700 mV. The scans at ± 1000 mV were taken at a tunneling current of $I = 0.8$ nA.

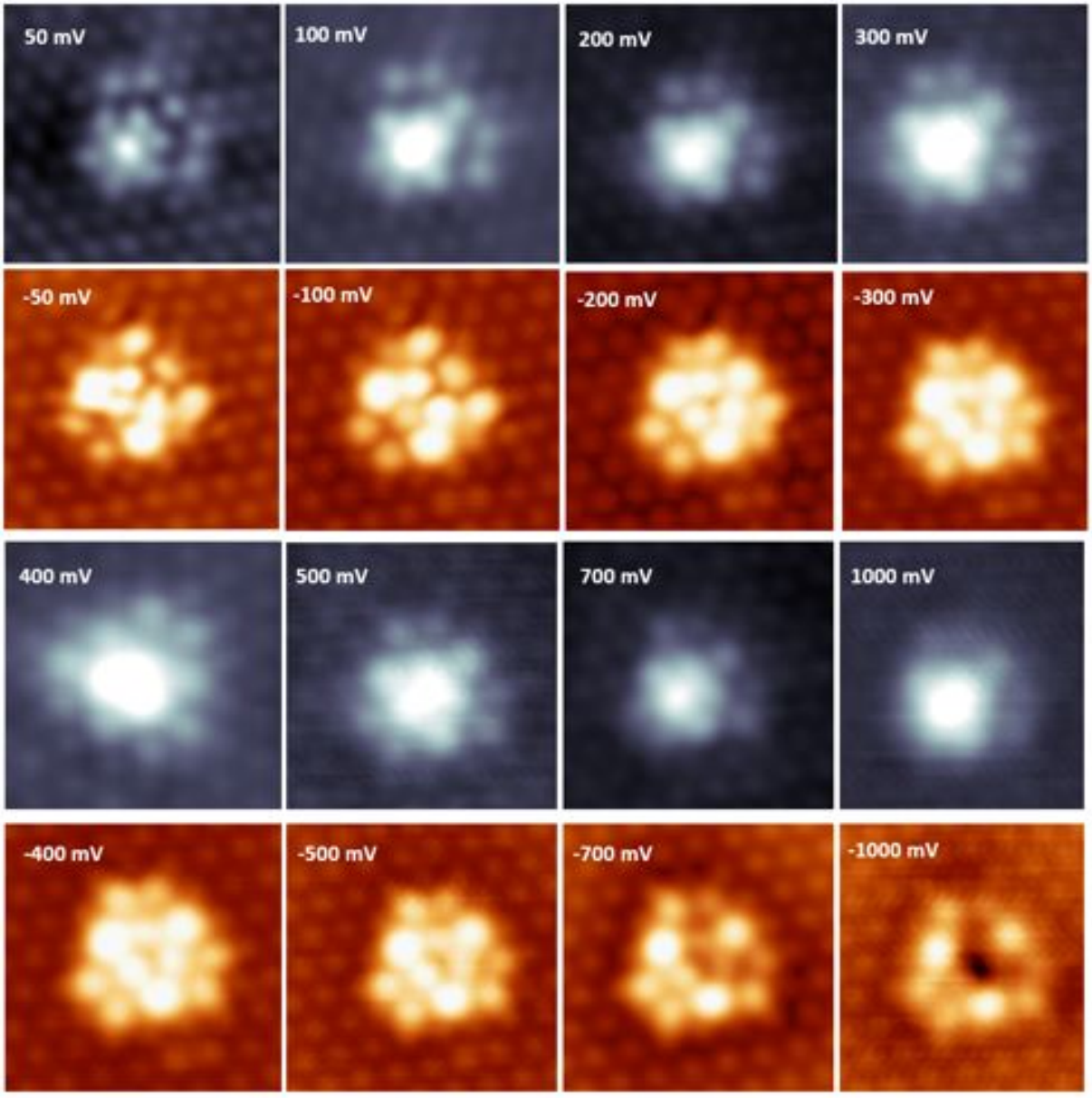

Figure 4.7: Bias-dependent topography images for cobalt feature 3 at $V = \pm 50$, ± 100, ± 200 and ± 300, ± 400, ± 500, ± 700 and ± 1000 mV.

Cobalt feature 4. Figure 4.8 shows bias-dependent topography images for the fourth cobalt feature. The size of the images is around 3×3 nm^2. The scans at ± 50 mV were taken at $I = 0.5$ nA, while those at ± 100 mV were measured at $I = 2$ nA. The tunneling current was $I = 2.5$ nA for images taken at ± 300. Images taken at ± 400, ± 500 and ± 700 mV were measured at $I = 3$ nA. The scans at ± 1000 mV were taken at a tunneling current of $I = 0.8$ nA.

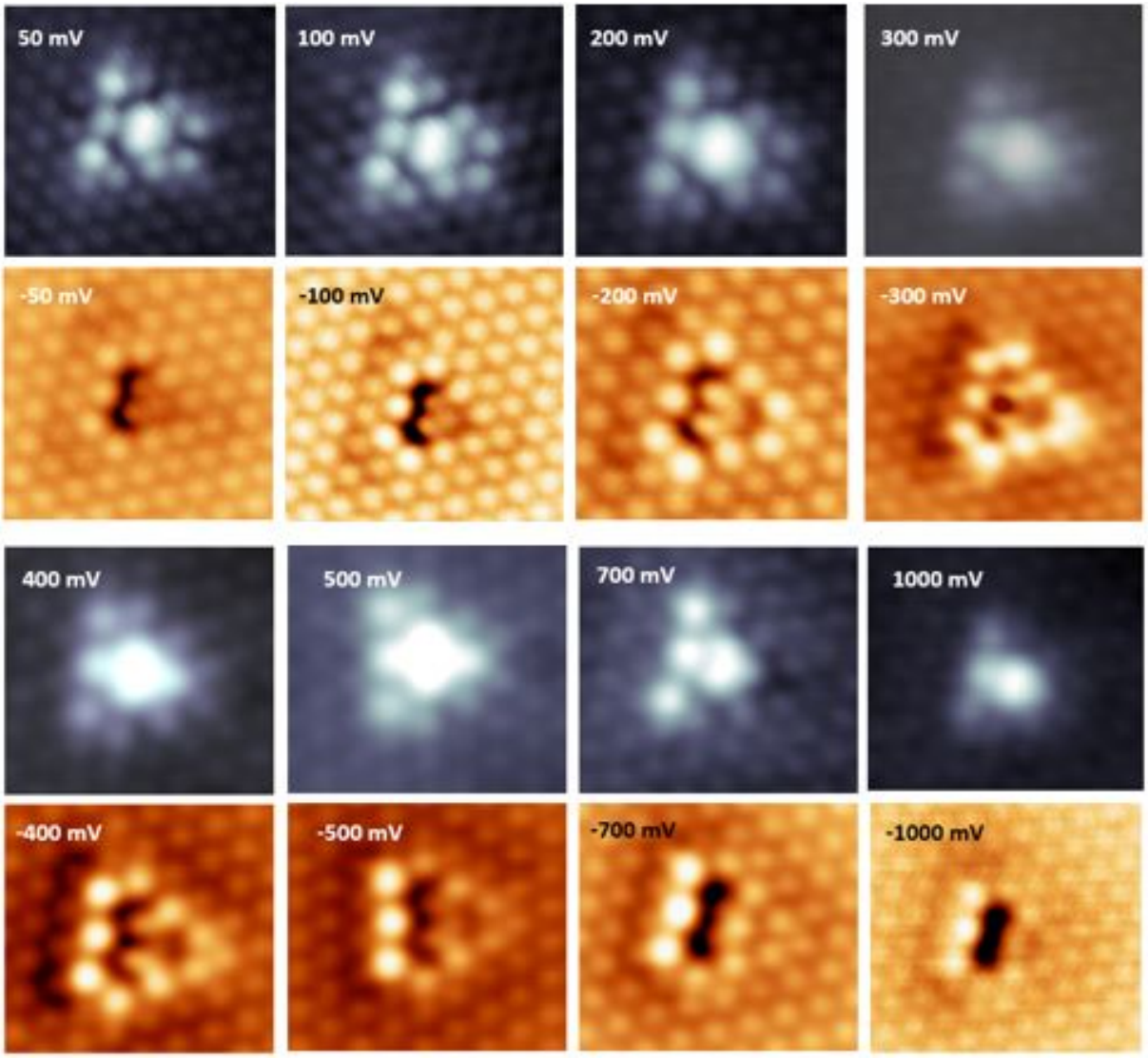

Figure 4.8: Bias-dependent topography images for cobalt feature 4 at $V = \pm 50$, ± 100, ± 200, ± 300, ± 400, ± 500, ± 700 and ± 1000 mV.

Spectroscopy

Having studied the topography of the new features, their spectroscopy is investigated next. Figure 4.9 shows single point spectroscopy taken at the background and on top of several cobalt features.

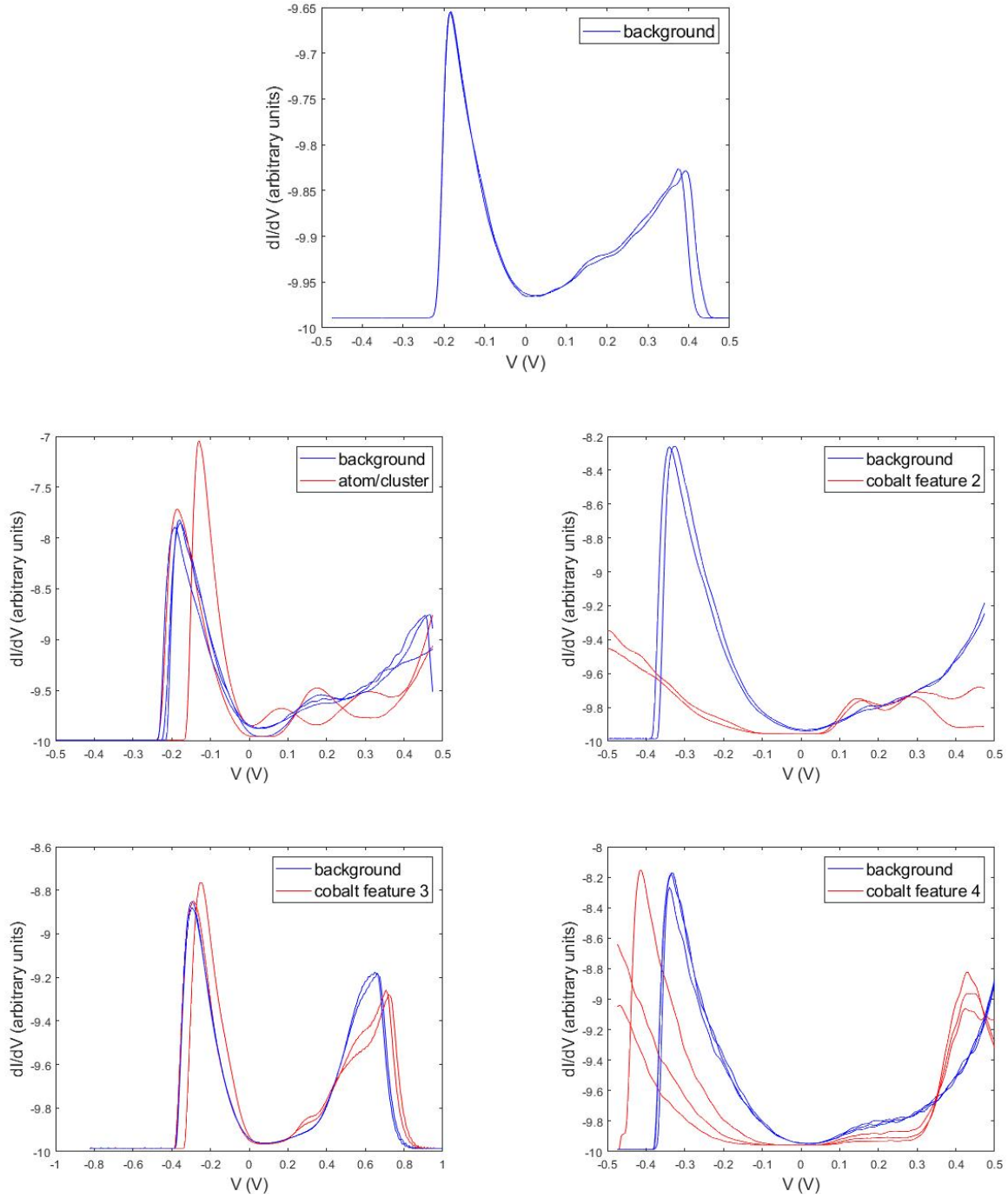

Figure 4.9: Several density of states spectra measured by single point spectroscopy taken after the atomic cobalt deposition. The first plot shows single point spectroscopy taken at the background in blue. Other plots show multiple spectra taken at features in red, with the background spectroscopy as a reference in blue. This is shown for features of the first category, cobalt feature 2, cobalt feature 3 and cobalt feature 4.

The top plot of figure 4.9 shows the $\mathrm{d}I/\mathrm{d}V$ spectrum of the background. It is seen to be comparable to the spectrum before the cobalt deposition (see figure 3.5). In the other plots, spectroscopy taken on top of new features is shown in red and compared to the background. Single point spectroscopy taken on top of features belonging to the fist

category (atoms or small clusters) deviates from the background spectrum, but not in the same way for separate features. This is not very surprising, since there are features of different sizes that belong to this first category. Spectroscopy taken on one of these features shows that the valence band is shifted and fluctuations in the band gap and conduction band. The spectrum measured at cobalt feature 2 has two discrete peaks in the conductance, seen around $V = 0.15$ and 0.3 V. The spectrum is also broadened. Single point spectroscopy on top of cobalt feature 3 shows a modification in the conduction band. Spectra measured at cobalt feature 4 reveal that both the valence band edge and the conduction band edge are shifted down to a lower energy. No conducting states are observed in the band gap.

Origin of the cobalt features

New features appearing after the atomic cobalt deposition are believed to be either atoms or clusters of cobalt on top of the surface or features formed by interaction of the cobalt atoms with the Bi_2Te_3 crystal, perhaps through a mechanism involving the structural defects. In an earlier work on single atom deposition on another Bi_2Te_3 sample, it was found that the observed features can be attributed to one-, two- and three-atom substitution of a bismuth atom in the second atomic layer by a cobalt atom [70]. This might also be the case for the second category features here, but to make definite statements one needs ab initio calculations.

4.3.2 Statistical analysis of native defects

In order to compare the native defects occurring after the cobalt deposition with those at the bare surface, the same statistical analysis as was done in subsection 3.3.2 is performed on a set of topographic scans after atomic cobalt deposition: the number of occurrences of each native defect is counted for several STM topography scans of the same size (70×70 nm^2). The results are shown in table 4.1. As was the case at the bare surface, only the first five defects occur regularly. The first native defect is not yet identified. Defect two is identified as a Bi_{Te} antisite at the first atomic layer, while defect 3 is tellurium vacancy at the first atomic layer. Defects 4 and 5 are Bi_{Te} antisites at the fifth and sixth atomic layers respectively.

Table 4.1: The frequency of the different native defects on 7 different scans of size 70×70 nm^2 for different bias voltages.

	1	**2**	**3**	**4**	**5**	**6**	**7**	**8**	**9**	**10**	**11**	**12**
600 mV	11	11	12	13	/	/	/	/	/	/	1	/
550 mV	12	10	12	16	4	/	/	/	/	/	1	/
500 mV	19	6	7	15	5	/	/	/	/	/	/	/
	12	10	12	20	/	/	/	/	1	/	1	/
450 mV	13	7	12	20	9	4	/	/	/	/	1	/
400 mV	11	10	13	15	/	/	/	/	2	/	4	/
350 mV	5	8	9	21	7	3	/	/	/	/	1	/

Since counting errors can be made, the resolution of scans can differ and different energies allow to probe different features, there is some uncertainty on these counted frequencies. To get a more robust estimate of the amount of the most occurring structural defects, the average is taken and the error is determined by the standard deviation as before and compared with the results found at the bare surface in subsection 3.3.2. The result is shown in table 4.2 and graphically in figure 4.10.

Table 4.2: The average frequency in number per scan of 70×70 nm^2 for the five most abundant defects (defect 1 - defect 5) on the bare surface and after the atomic cobalt deposition.

defect	**1**	**2**	**3**	**4**	**5**
average bare surface	16 ± 2	3 ± 1	21 ± 1	20 ± 1	8 ± 2
average after Co deposition	12 ± 2	11 ± 1	11 ± 1	17 ± 1	4 ± 1

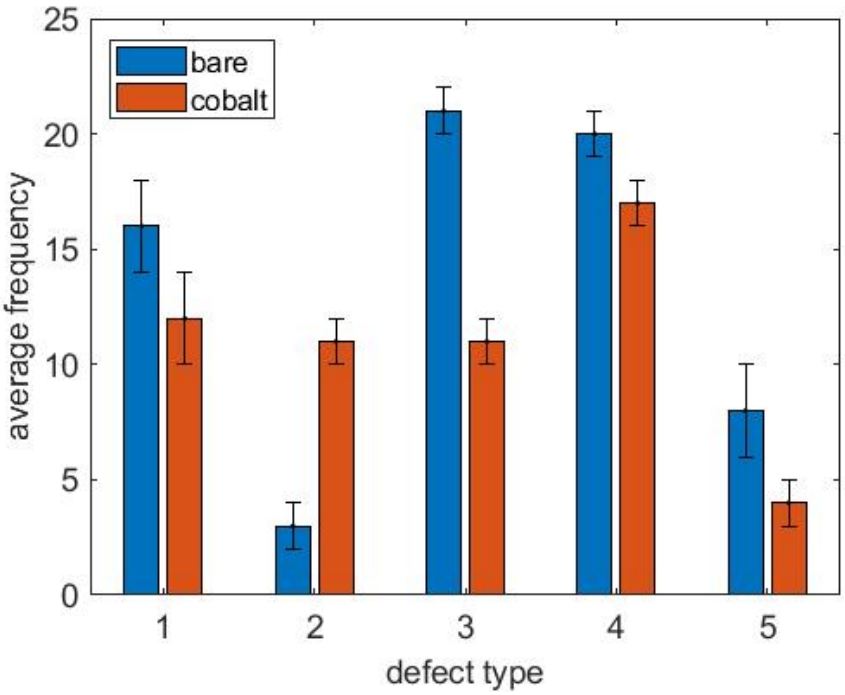

Figure 4.10: Bar plot showing the average frequency in number per scan of 70×70 nm^2 for the five most abundant defects (defect 1 - defect 5) on the bare surface (blue) and after the atomic cobalt deposition (red).

The frequency of defect 1 seems to maintain its order of magnitude while defect 2 appears to occur much more than before. These numbers should be regarded with caution however, since the sample surface shows many protrusions after the cobalt deposition, which are not always easily distinguishable from each other. It is thus possible that defect 1 was counted as defect 2 (or the other way around) or that a feature originating from the cobalt atoms was counted as defect 2. The frequency of defect 3 is halved after the deposition.

This drop might indicate some partial participation of these defects in the formation of new features. Since defect 3 is a tellurium vacancy at the first atomic layer, it might be the case that cobalt atoms are attracted to these vacancies. This hypothesis is plausible, since it has been shown that cobalt atoms are selectively adsorbed on top of Se sites in Bi_2Se_3, which has a similar structure [116]. The frequency of defect 4 seems to stay about the same. The frequency of defect 5 drops down to half of its value at the bare surface. However, this defect is already difficult to resolve at the bare surface. After the cobalt atoms have been deposited, the color scale gets calibrated again and resolving defect 5 becomes even more difficult, which might explain the frequency drop. Defect 5 is also not detected in about half of the scans and so the statistics for this defect are less reliable than those for the others.

4.4 Scattering events

In this section, the scattering events occurring at the surface after the atomic cobalt deposition are examined. As for the bare surface, this is done using QPIs (see subsection 2.1.3). Subsection 4.4.1 entails a discussion about Fourier transforms of LDOS maps measured using STS, and this for several different energies. Subsection 4.4.2 shows the energy dispersion of the surface states in the $\bar{\Gamma} - \bar{\mathrm{M}}$ direction, which is determined using the scattering wavevector determined from these Fourier transforms. From the dispersion, the fermion velocity v_F and the Dirac point energy E_D are estimated.

4.4.1 Quasiparticle interference patterns

Figure 4.11 shows a STM topography image of about 70×65 nm^2 of the surface and its corresponding conductance map, measured as explained in subsection 2.1.2. The QPIs visible in the $\mathrm{d}I/\mathrm{d}V$ map are due to scattering of the electronic states. The scattering patterns have different wavelengths. While there are still visible interference patterns due to the native defects 1 and 3, the strongest scattering centers are the cobalt features (see figure 4.12).

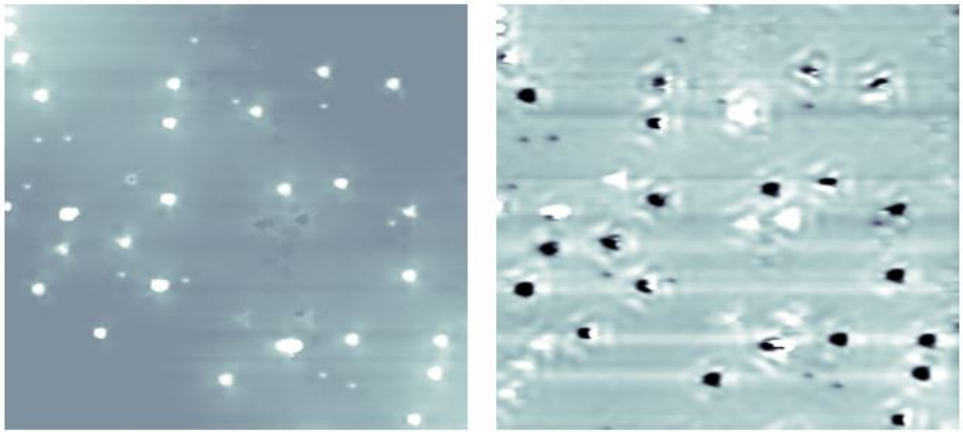

Figure 4.11: (left) 70×65 nm^2 STM topography image of the Bi_2Te_3 surface after atomic cobalt deposition at $I = 2.5$ nA and $V = 400$ mV. (right) The corresponding LDOS map, showing the formation of standing waves on the surface.

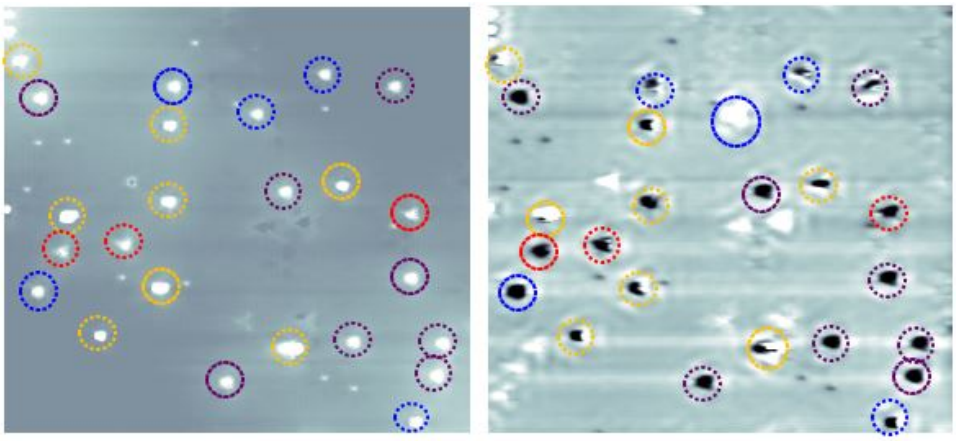

Figure 4.12: The topography (left) and LDOS (right) images shown in the previous figure 4.11, where features are marked. Most of the scattering events are due to the cobalt features. Features of the first category are indicated in yellow, while purple circles denote cobalt feature 2. Cobalt features 3 and 4 are marked with blue and red circles respectively.

Conductance maps like this were studied at several different energies. To better see the periodicity of the patterns, Fourier transforms of them are taken (see figure 4.13).

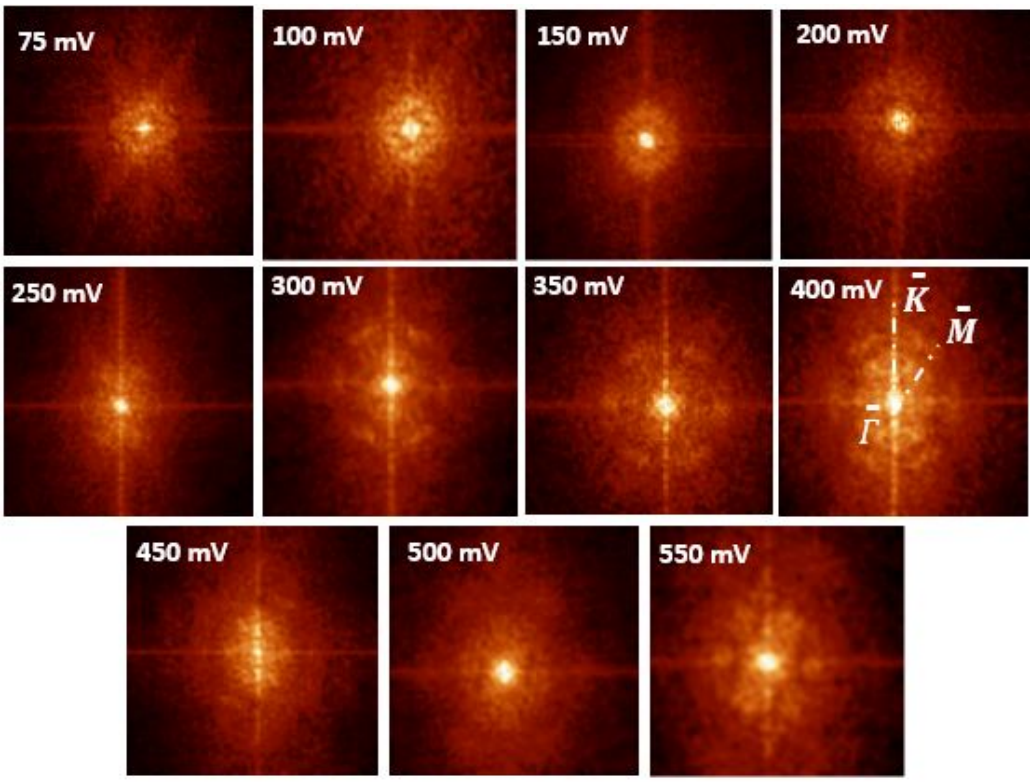

Figure 4.13: The Fourier transforms of conductance maps measured at $V = 75$, 100, 150, 200, 250, 300, 350, 400, 450, 500 and 550 mV after the atomic cobalt deposition. The images are about 2×2 1/nm^2 in size.

Compared to the bare surface (see subsection 3.5), the scattering seems more uniform in direction, especially at lower voltages: at $V = 75$, 100, 150 and 200 mV, the scattering

pattern seem to be uniform in direction. At $V = 250$, 300, 350 and 400 mV, the intensities in the $\bar{\Gamma} - \bar{\mathrm{M}}$ are brighter than those in the $\bar{\Gamma} - \bar{\mathrm{K}}$ direction, but the difference is less pronounced than at the bare surface. At $V = 450$, 500 and 550 mV, the scattering appears to be uniform again. It is plausible that the introduction of magnetic impurities (the deposited cobalt atoms) makes it possible for surface state electrons to backscatter. Aside from this spreading in the angular direction, which is indicative of backscattering, there is also some spread in the radial direction. Interpreting the meaning of this radial spread is not straightforward.

4.4.2 Energy dispersion relation of the surface states

Using information from the Fourier transforms in figure 4.13, the dispersion of energy as a function of q in the $\bar{\Gamma} - \bar{\mathrm{M}}$ direction can be determined for the surface states. The result is shown in figure 4.14. The errors on the q-values are determined by the resolution of the Fourier transform images. The best fit to the data (shown as a red line on the figure) demonstrates that the dispersion is indeed linear, as expected for the Dirac fermions. The dispersion relation is given by

$$E = aq + b,$$

where $a = 220 \pm 30$ meV nm and $b = -220 \pm 70$ meV. The quality of the fit is quantified by an R^2-value of 0.9734.

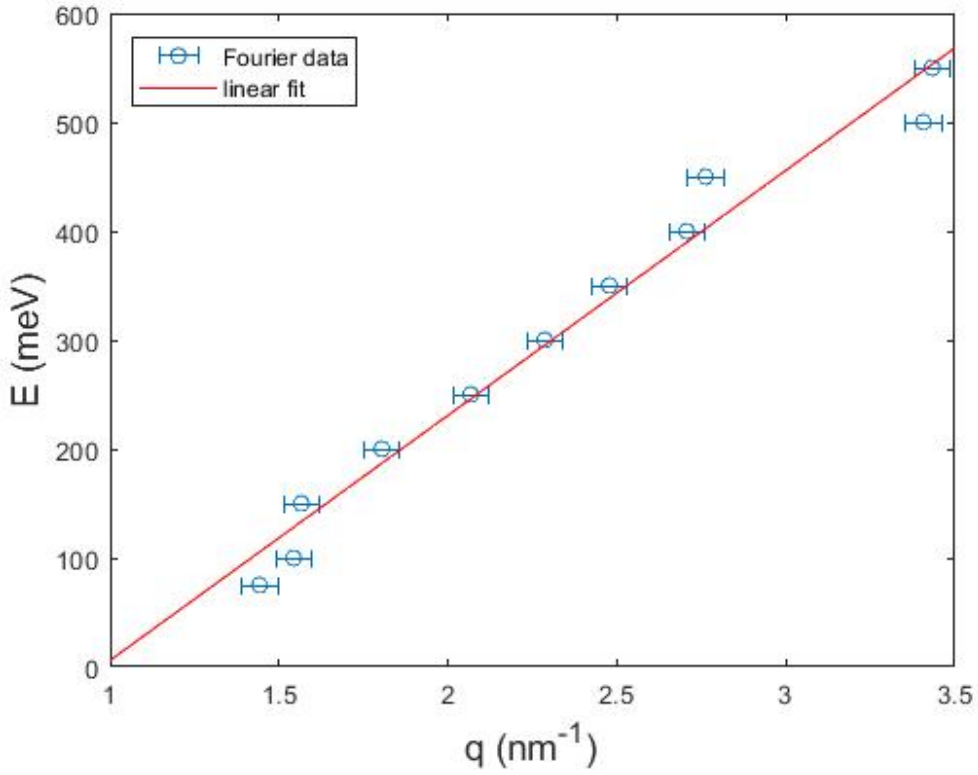

Figure 4.14: The $E(q)$-dispersion in the $\bar{\Gamma} - \bar{\mathrm{M}}$ direction for the surface of Bi_2Te_3 after atomic cobalt deposition.

From this dispersion, the Dirac fermion velocity and the Dirac point energy are estimated.

$$v_F = \frac{1}{\hbar}\frac{\mathrm{d}E}{\mathrm{d}k} = \frac{1}{\sqrt{3}\hbar}\frac{\mathrm{d}E}{\mathrm{d}q} = \frac{1}{\sqrt{3}\hbar}a = (2.0 \pm 0.2) \times 10^5 \text{ m/s},$$
$$E_D = b = -220 \pm 70 \text{ meV}.$$

These values are in agreement with the ones at the bare surface, where they were calculated as $v_F = (2.1 \pm 0.4) \times 10^5$ m/s and $E_D = -260 \pm 90$ meV. The shift in the Dirac energy might indicate some doping induced by the cobalt atoms.

4.5 Chapter summary

This chapter presents the results of the surface characterization of the topological insulator Bi_2Te_3 after atomic cobalt deposition using STM and STS.

Topography of the surface reveals new features arising due to the deposited cobalt atoms as well as the native defects seen at the bare surface. The new features seen after the deposition can be divided into two categories. The features in the first category are protrusions on the surface with a spherical shape and appear with different sizes. These features are assumed to be cobalt atoms and small cobalt clusters. The second category of features are more geometric in their structure. They might be explained as cobalt atoms substituting bismuth atoms at the second atomic layer, but one needs simulations to confirm this hypothesis. A statistical analysis of the native defects of the crystal shows that the frequency of defects 3 and 5 drop down to half of their value at the bare surface. As defect 3 is a tellurium vacancy at the first atomic layer ($V_{Te,1}$), this drop might be indicative of some interaction between the deposited atoms and the vacancies. For defect 5, which is a bismuth atom substituting a tellurium atom at the sixth atomic layer ($V_{Te,6}$), it is not that straightforward to formulate a hypothesis explaining this observation since this defect is not found immediately at the surface.

LDOS maps of the surface show quasiparticle interference patterns. While the main scattering centers at the bare surface (feature 1 and feature 3, which is $V_{Te,1}$) are still visible, there are also new scattering centers due to cobalt features. The scattering patterns appear more uniform in direction than before the atomic cobalt deposition, making it plausible that the deposited cobalt atoms make it possible for surface state electrons to backscatter. There is also some smearing in the radial direction, which is less easily understood. The dispersion relation of the surface states along the $\bar{\Gamma} - \bar{\mathrm{M}}$ direction is linear, as expected for massless Dirac fermions. The fermion velocity and Dirac point energy derived from this dispersion relation are $v_F = (2.0 \pm 0.2) \times 10^5$ m/s and $E_D = -220 \pm 70$ meV. This fermion velocity agrees with the one found at the bare surface, which is $(2.1 \pm 0.42) \times 10^5$ m/s. The Dirac point energy is higher than the one retrieved at the bare surface (-260 ± 90 meV): the deposited cobalt atoms induce some doping.

Chapter 5

Chromium deposition

The objective of this chapter is studying the surface of Bi_2Te_3 after the deposition of single magnetic chromium (Cr) atoms using STM and STS. The motivation for this study is similar to that of the previous chapter: to shed light on the impact of chromium surface dopants on the electronic behavior of the Bi_2Te_3 surface states. There have been studies demonstrating the breaking of time reversal symmetry in bulk chromium doped TIs [117,118], but a detailed study on surface doped TIs by chromium atoms by means of STM/STS has not been reported yet, to the best of our knowledge. Understanding this interaction between the TI surface and the magnetic impurities is an important step in realizing exotic phenomena such as the QAHE and also in improving the knowledge of TI device fabrication.

This chapter is structured as follows. The deposition is briefly discussed in section 5.1. Section 5.2 shows an overview of the sample topography, while section 5.3 focuses on individual features. The concluding section of this chapter, section 5.4 investigates the scattering events occurring at the sample surface by means of QPIs.

5.1 Deposition

The chromium atoms are deposited at room temperature using one of the evaporation cells described in section 2.1.4 for a time of 2 seconds with a flux of 20 nA. As described in chapter 4 for the cobalt dopants on Bi_2Te_3, the deposited amount of chromium atoms is too small to quantify in a reliable way.

5.2 Overview

The surface after the chromium deposition is studied in this section. Figure 5.1 shows a 70×70 nm^2 STM topography image of the Bi_2Te_3 surface after atomic chromium deposition at $I = 0.5$ nA and $V = \pm 500$ mV. Upon comparison to the surface after atomic cobalt deposition (figure 4.1), it is clear that the surface looks similar to how it looked after the cobalt deposition: it shows the same native defects as at the bare surface, but there are also other features present. Some of these features are protrusions on the surface, which the STM tip is likely to interact with. The tip is thus easily modified, making imaging more difficult.

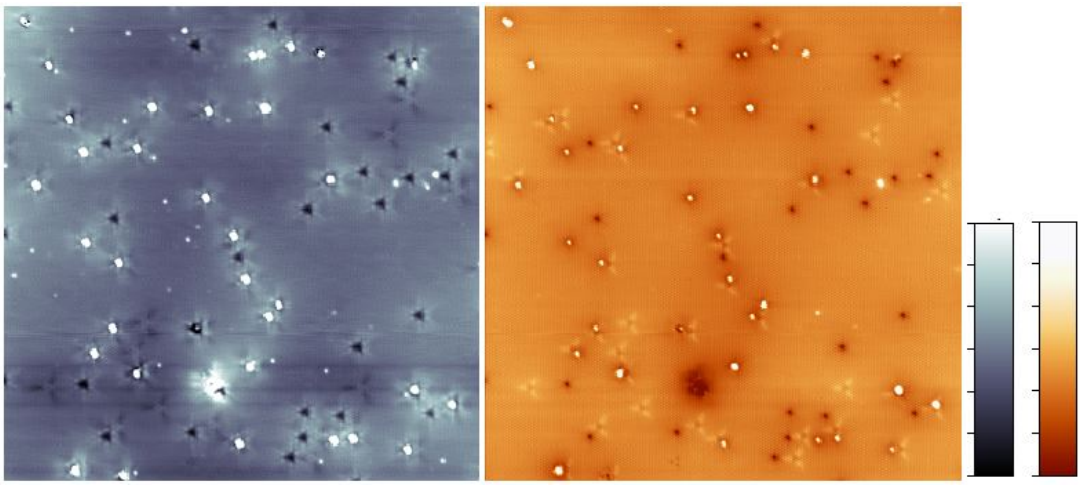

Figure 5.1: 70×70 nm^2 STM topography image of the Bi_2Te_3 surface after atomic chromium deposition at $I = 0.5$ nA and (left) $V = +500$ mV (right) $V = -500$ mV.

5.3 Examining native defects and chromium features

This section is dedicated to studying the growth of chromium atoms on the TI surface of Bi_2Te_3 by means of STM and the resulting electronic properties by means of STS. As for the cobalt deposition, it can be the case that deposited chromium atoms can give rise to interesting features in topographic images of the surface. This is the subject of subsection 5.3.1. It might also be the case that the deposited atoms interact with native defects. This is studied through a statistical analysis in subsection 5.3.2.

5.3.1 Chromium features

Aside from the native defects, some new features can be seen on the surface after the chromium deposition. As was the case after the atomic cobalt deposition (see subsection 4.3.1), the features can be divided into two categories. A first category of features consists of protrusions on the surface with a spherical shape. Features belonging to the second category are more geometric in structure. This subsection is dedicated to gathering more information about these new features by using STM and STS.

Atom and cluster features

The features appearing after the chromium deposition can be divided into two categories. Features in the first category are protrusions on the surface with a spherical shape. A small scale topography image of one of these features is shown in figure 5.2. Topography after the deposition, shown in figure 5.3, reveals that this kind of feature occurs with different sizes. This is also seen from height profiles taken along different features (see figure 5.4).

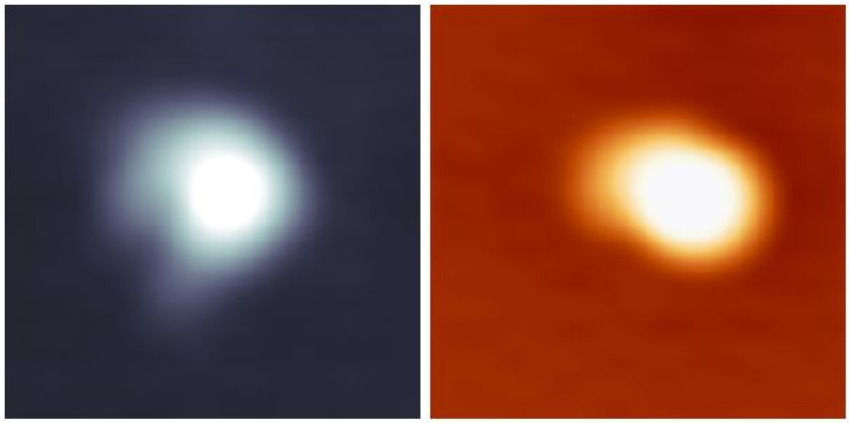

Figure 5.2: 3.4×3.4 nm^2 STM topography image of the Bi_2Te_3 surface after atomic cobalt deposition at $I = 0.5$ nA and (left) $V = +700$ mV (right) $V = -700$ mV.

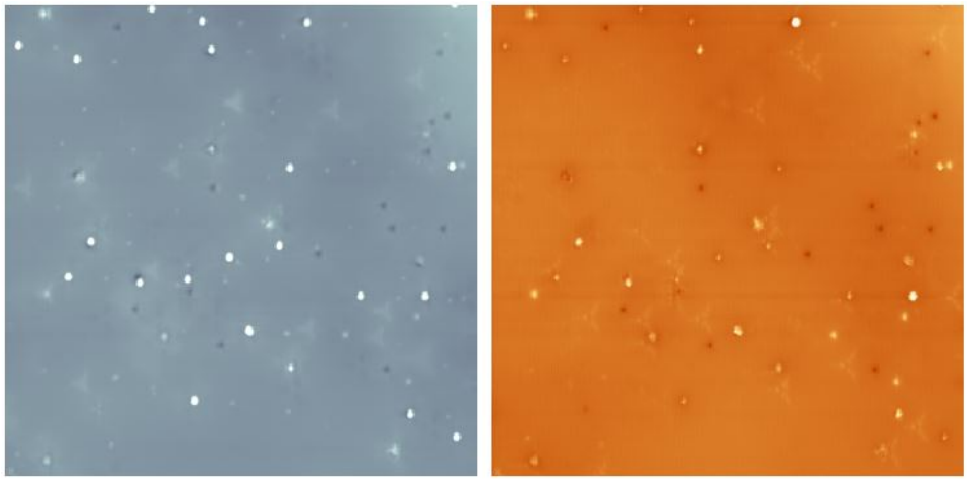

Figure 5.3: 70×70 nm^2 STM topography image of the Bi_2Te_3 surface after atomic chromium deposition at $I = 0.3$ nA and (left) $V = +700$ mV (right) $V = -700$ mV.

There are seven distinguishable peaks. The first peak has a height of 1.9 ± 0.1 Å (0.6 ± 0.1 Å) in the empty (filled) states. The second peak has a height of 0.8 ± 0.1 Å (1.2 ± 0.1 Å), while that of the third peak is 2.0 ± 0.1 Å (1.2 ± 0.1 Å). A fourth peak has the same height as the third in the empty states, but differs from it in the filled states: its height is 2.0 ± 0.1 Å (0.8 ± 0.1 Å). The fifth peak has a height of 1.9 ± 0.1 Å (1.4 ± 0.1 Å), while the sixth is 0.6 ± 0.1 Å (0.4 ± 0.1 Å) high. The seventh and final peak has a height of 2.2 ± 0.1 Å (0.9 ± 0.1 Å). There are only two native defects which are protrusions (native defect 1 and 2). As explained in subsection 4.3.1, the heights of the native defects cannot be directly compared with the heights retrieved here. But since there are more than two different heights, one can conclude that at least some of these peaks are due to the new features. This kind of defect exists with different sizes. The explanation is the same as after the cobalt deposition: the chromium atoms were deposited at room temperature. Because of this, the atoms can aggregate and form small clusters at the sample surface.

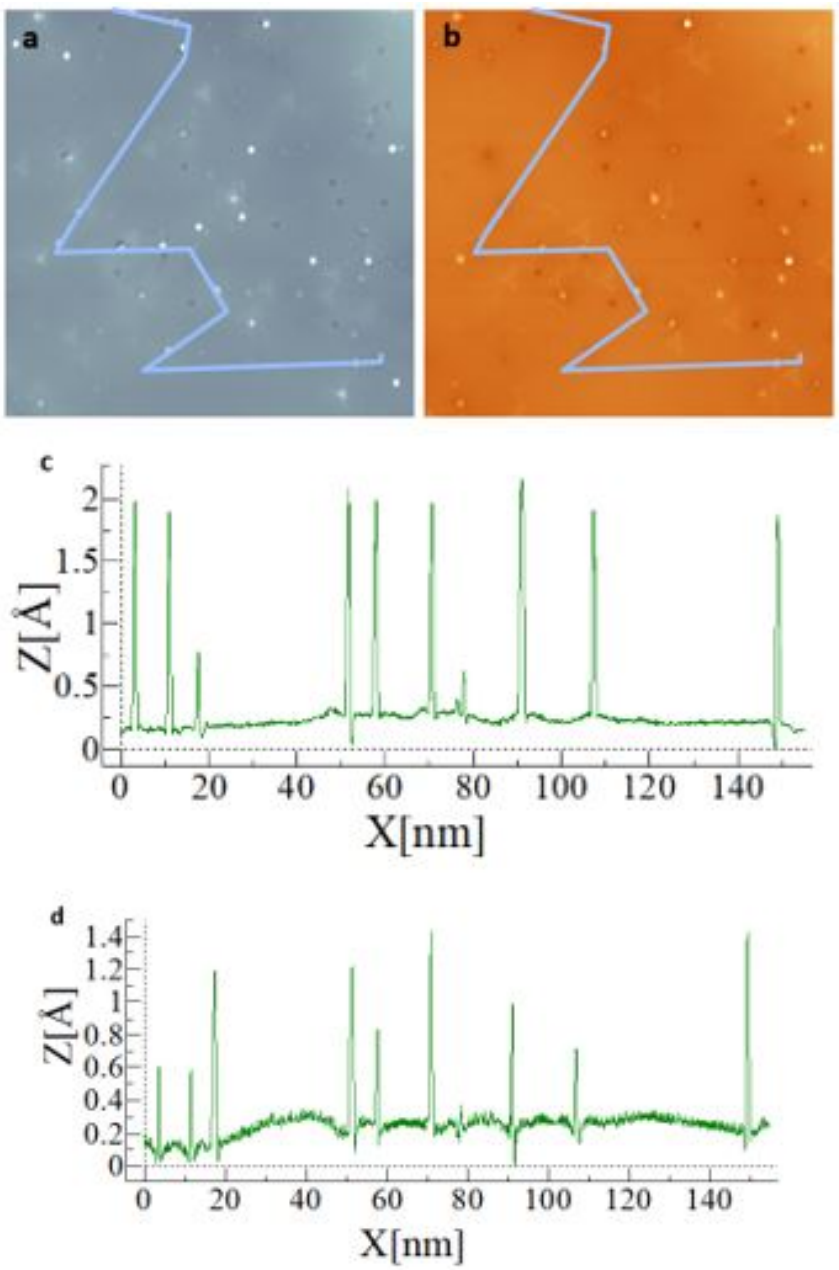

Figure 5.4: (a) and (b) show 70×70 nm^2 STM topography images of the Bi_2Te_3 surface after atomic chromium deposition at $I = 0.3$ nA and (a) $V = +700$ mV, (b) $V = -700$ mV. (c) and (d) show the height profiles taken along the surface paths indicated in (a) and (b) respectively.

Geometric features

The first category of features is thus explained as chromium atoms and clusters on the sample surface. There are also other, new features after the deposition, whose origin cannot be explained in this way. They are more geometric in structure and are believed to arise due to some interaction between the chromium atoms and the Bi_2Te_3crystal. Three of these features are distinguished. The features belonging to this second category are studied in the following paragraphs.

Chromium feature 1. Figure 5.5 shows bias-dependent topography images for the first chromium feature. The size of the images is around 3×3 nm^2. The scans at $\pm$300 mV were taken at a tunneling current of $I = 2.5$ nA, while those at $\pm$400 and $\pm$500 mV were measured at $I = 2$ nA.

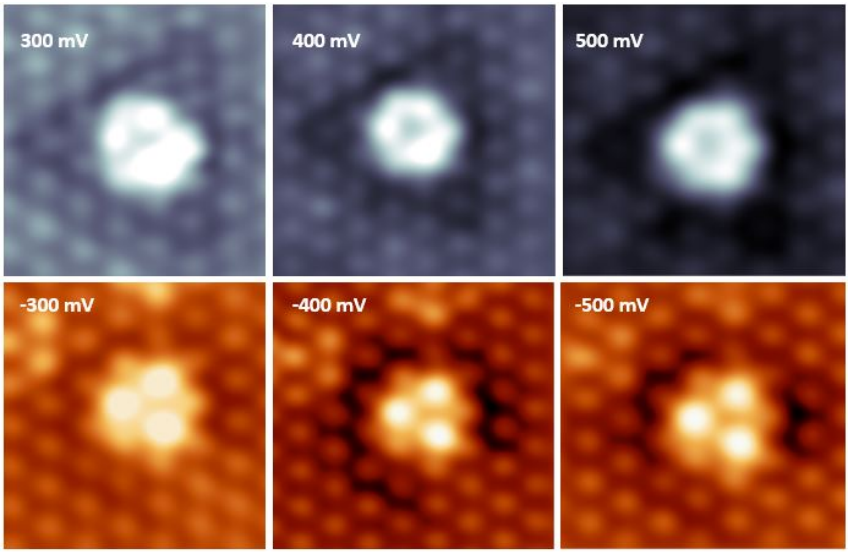

Figure 5.5: Bias-dependent topography images for chromium feature 1 for $V = \pm$300, $\pm$400 and $\pm$500 mV.

Chromium feature 2. In figure 5.6, bias-dependent topography of the second chromium feature is shown. The size of the images is around 3×3 nm^2. The tunneling current was $I = 0.7$ nA for images taken at $\pm$400 and $\pm$500 mV. The scans at $\pm$700 mV were taken at a tunneling current of $I = 1$ nA.

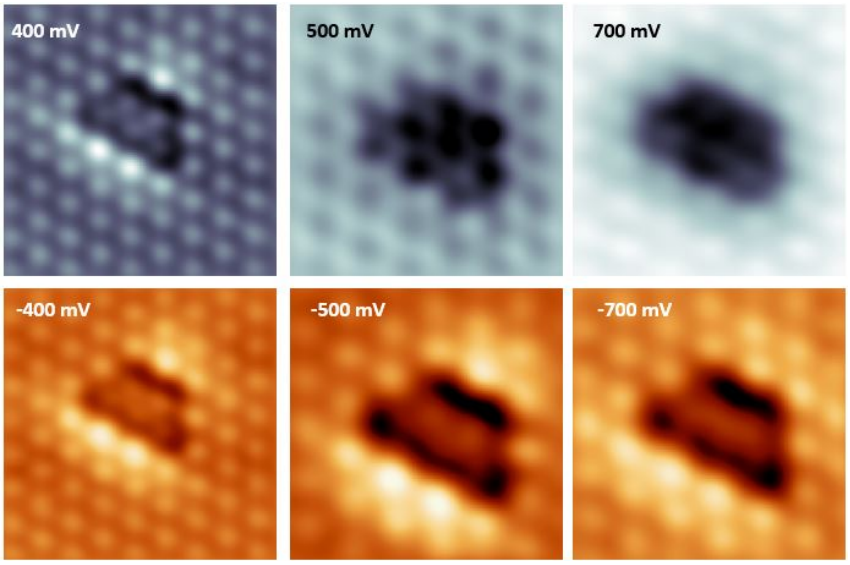

Figure 5.6: Bias-dependent topography images for chromium feature 2 for $V = \pm$400, $\pm$500 and $\pm$700 mV.

This feature looks similar to a feature identified in an earlier work [70] as two-atom Co_{Bi}

substitution in the second atomic layer of a n-type Bi_2Te_3 sample. This similarity makes it plausible that chromium feature 2 is a two-atom Cr_{Bi} substitution in the second atomic layer. Interestingly, this type of feature was not observed among the cobalt features for the series of cobalt deposition experiment (chapter 4), which might indicate that the doping level through native defects in TIs plays a role in the interaction between the magnetic atoms and the surface of Bi_2Te_3.

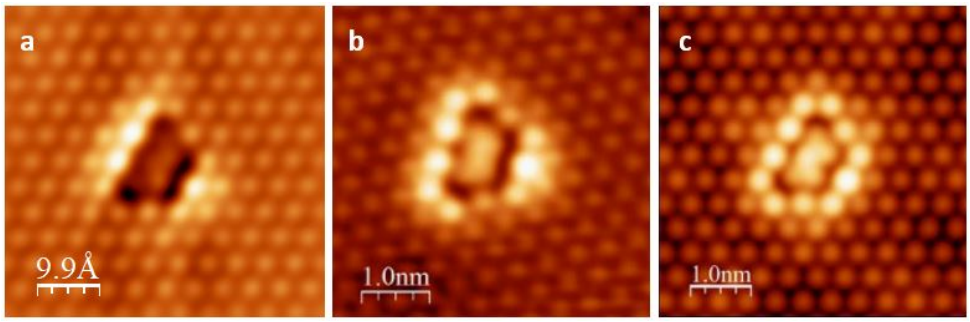

Figure 5.7: (a) Atomically resolved STM image of chromium feature 2 at $I = 0.7$ nA and $V = -400$ mV. (b) Atomically resolved STM image and (c) DFT based STM image of two-atom Co_{Bi} substitution in the second atomic layer. Images (b) and (c) are taken from [70].

Chromium feature 3. Topography images of the third chromium feature are shown in figure 5.8. The size of the images is around 3×3 nm^2. The scans at ± 300 mV were taken at a tunneling current of $I = 0.5$ nA. For the images taken at ± 400 and ± 500 mV, the tunneling current is $I = 1$ nA.

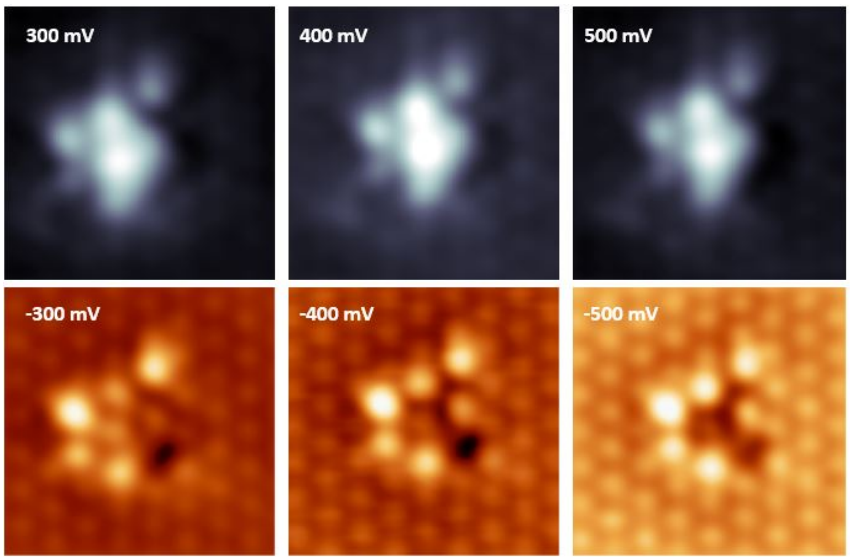

Figure 5.8: Bias-dependent topography images for chromium feature 3 for $V = \pm 300$, ± 400 and ± 500 mV.

Spectroscopy

Having studied the topography of these three features, their density of states is also examined by means of STS (see figure 5.9).

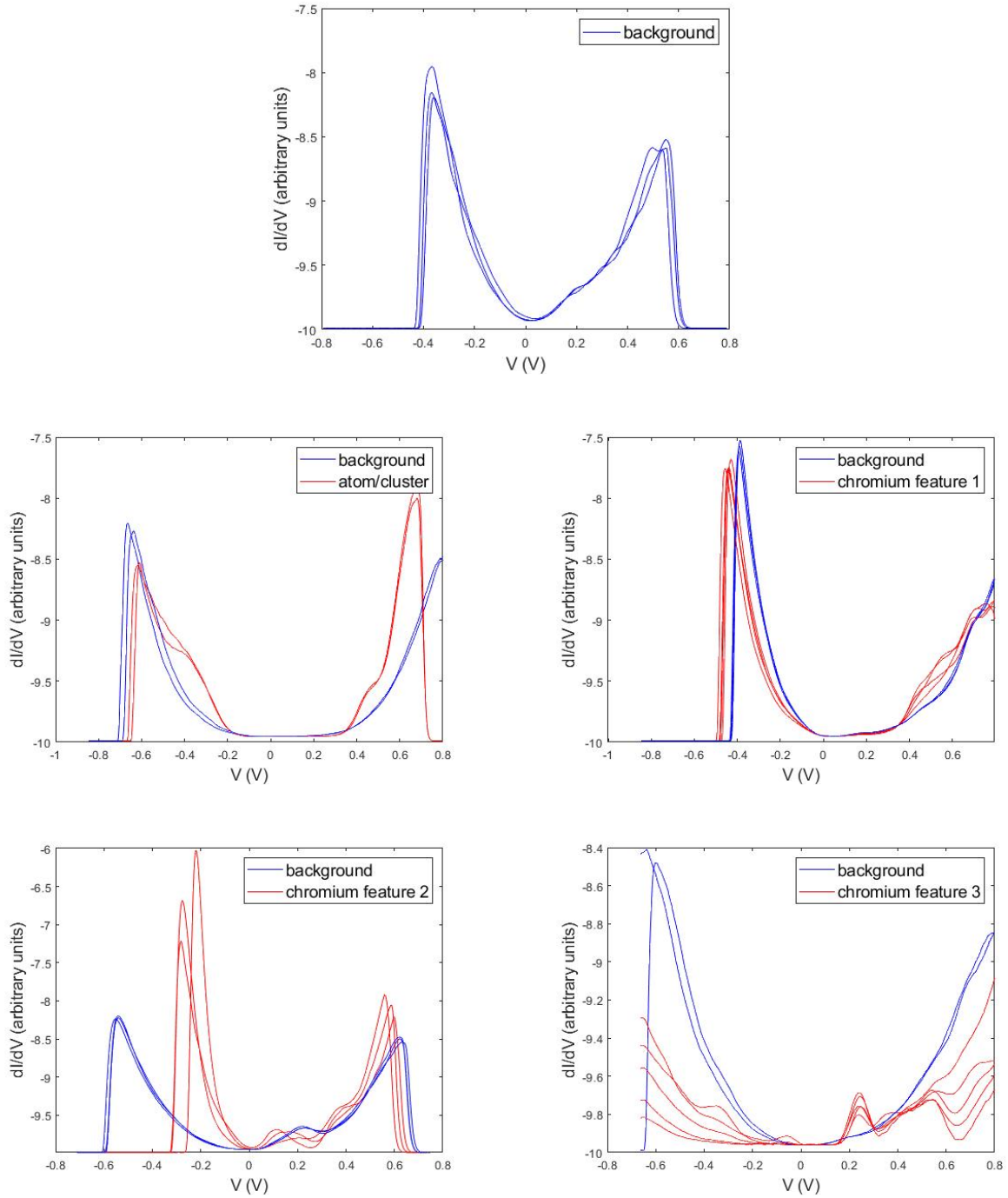

Figure 5.9: Multiple spectra taken by single point spectroscopy after the atomic chromium deposition. Single point spectroscopy taken at the background is shown in blue. Single point spectroscopy taken at features is shown in red, with the background spectroscopy as a reference in blue for features of the first category, chromium feature 1, chromium feature 2 and chromium feature 3.

The background spectrum is similar to the ones measured at the bare surface and after the cobalt deposition (see figures 3.5 and 4.9). The spectra measured for features of the first category show a shift in both the valence and conduction band. Both of the bands show a shoulder. It should be noted that both red spectra in this plot are measured at the same feature. It is expected that the spectroscopic signature of differently sized features also belonging to this category might differ from the one shown here. The spectrum measured at chromium feature 1 shows a small shift of the valence band. The conduction band is also modified. Single point spectroscopy on top of chromium feature 2 reveals a large shift in the valence band, a discrete peak at 0.12 V and a small shift of the conduction band. The spectrum taken on top of chromium feature 3 is broadened and shows a discrete peak at 0.24 V.

Origin of the chromium features

As was the case after the atomic cobalt deposition (see subsection 4.3.1), new features appearing after the atomic chromium deposition can be divided into two categories. The features belonging to the first category are believed to be atoms and small clusters of chromium on top of the surface. The second category of features cannot be identified using only STM topography scans. These features are believed to be formed through some interaction of the chromium atoms with the Bi_2Te_3 crystal, perhaps through a mechanism involving the structural defects. In recent works investigating the chromium bulk doped TIs Bi_2Se_3 and Sb_2Te_3 [117,118], it was found that chromium-induced defects can be explained as substitutional chromium atoms occupying sub-surface bismuth and antimony sites. Knowing this, it is a reasonable hypothesis that the chromium features are formed by chromium atoms that diffuse to the second atomic layer and occupy bismuth sites. Ab initio calculations are needed to verify or disprove this hypothesis.

5.3.2 Statistical analysis of native defects

To see whether the frequency of the native defects observed at the bare surface (see subsection 3.3.2) changes after the chromium deposition, a statistical analysis is performed. Doing this also allows for a comparison with the defect frequencies found after the cobalt deposition (see subsection 4.3.2). The applied method is the same as in subsections 3.3.2 and 4.3.2: several topography scans of 70×70 nm^2 are studied and for each of them, the number of occurrences of each native defect is counted. The numbers retrieved in this way are shown in table 5.1. Only native defects 1, 2, 3, 4 and 9 occur regularly. There is some uncertainty on these numbers because of several reasons. Firstly, during the counting procedure errors can be made. Secondly, the resolution of scans can differ and thirdly, different energies allow to probe different features. Due to this, the average is taken to get a more robust estimate of the amount of the structural defects. The error is determined by the standard deviation.

Table 5.1: The frequency of the different native defects on 26 different scans of size 70×70 nm^2 for different bias voltages.

	1	**2**	**3**	**4**	**5**	**6**	**7**	**8**	**9**	**10**	**11**	**12**
700 mV	13	3	24	13	/	3	/	2	5	/	/	1
	22	6	16	15	/	/	/	/	3	/	/	2
	6	3	8	8	9	1	1	/	6	/	/	2
	7	3	15	17	13	2	1	/	10	/	/	1
	17	3	10	2	/	/	/	1	2	/	/	/
	22	2	16	16	/	/	1	2	1	/	/	/
	19	3	11	21	8	1	/	/	1	/	/	/
	14	/	6	1	3	/	/	/	1	/	/	/
	11	3	9	3	/	/	/	1	/	/	/	/
	22	3	7	13	1	/	/	1	/	/	/	/
	27	5	11	20	/	/	/	1	/	/	/	/
	8	/	13	5	3	/	/	/	/	/	/	/
	22	4	7	9	/	/	/	/	/	/	/	/
	30	2	13	12	/	/	/	/	/	/	/	/
	17	2	9	15	/	/	/	/	/	/	/	/
500 mV	6	1	14	22	6	2	/	/	10	/	1	2
	20	3	20	12	10	2	/	2	1	/	/	/
	24	2	13	19	12	2	/	/	8	/	/	/
	7	/	15	10	/	/	/	/	2	/	/	/
	7	/	12	7	/	/	/	/	/	/	/	/
	7	/	12	7	/	/	/	/	/	/	/	/
	9	1	11	6	/	/	/	/	/	/	/	/
	18	3	3	10	/	/	/	/	/	/	/	/
	23	3	5	9	/	/	/	/	/	/	/	/
300 mV	14	1	8	10	3	2	/	2	1	/	1	/
	12	2	5	11	4	/	/	1	/	/	1	/

To compare with the bare surface and the surface after the cobalt deposition, this average is taken for the first five native defects. The first native defect is not yet identified. Defect two and three are identified as a Bi_{Te} antisite at the first atomic layer and tellurium vacancy at the first atomic layer respectively. Defect 4 and 5 are both Bi_{Te} antisites: defect 4 at the fifth atomic layer and defect 5 at the sixth. The results are shown in table 5.2. A graphical representation comparing the retrieved frequencies with those found at the bare surface and after the cobalt deposition is shown in figure 5.10. The average frequency after the chromium deposition is comparable to that at the bare surface for native defects 1, 2 and 4. Native defect 3 (a tellurium vacancy at the first atomic layer) shows a drop in frequency to half its value at the bare surface. This is similar to the observations after the atomic cobalt deposition and might indicate that this vacancy is in some way participating in the formation of new features. The frequency of defect 5 also drops to half of its value at the bare surface. It should be noted that this observation was also made after the cobalt deposition. It is not straightforward to formulate a hypothesis explaining this frequency drop: defect 5 is a Bi_{Te} antisite at the sixth atomic layer. This defect is

not found directly at the surface and so the mechanism resulting in the frequency drop is not obvious. It should be noted that after the chromium deposition, defect 5 becomes more difficult to resolve than at the bare surface. As such, it is possible that it was not counted when present, resulting in a frequency that is too low.

Table 5.2: The average frequency in number per scan of 70×70 nm^2 for the five most abundant defects (defect 1 - defect 5) on the bare surface, after the atomic cobalt deposition and after the atomic chromium deposition.

defect	**1**	**2**	**3**	**4**	**5**
average bare surface	16 ± 2	3 ± 1	21 ± 1	20 ± 1	8 ± 2
average after Co deposition	12 ± 2	11 ± 1	11 ± 1	17 ± 1	4 ± 1
average after Cr deposition	16 ± 1	2 ± 1	11 ± 1	20 ± 1	3 ± 1

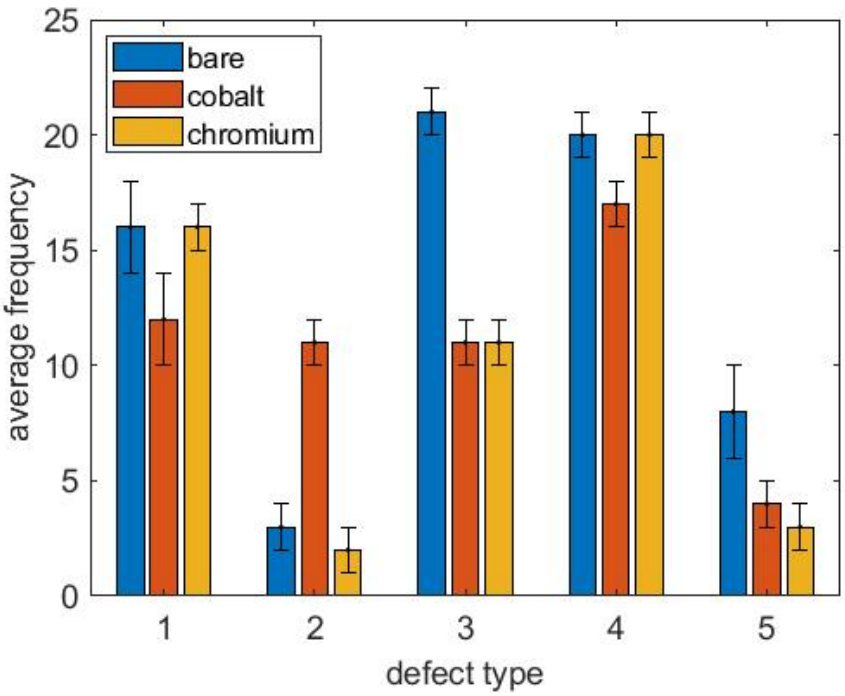

Figure 5.10: Bar plot showing the average frequency in number per scan of 70×70 nm^2 for the five most abundant defects (defect 1 - defect 5) on the bare surface (blue), after the atomic cobalt deposition (red) and after the atomic chromium deposition (yellow).

5.4 Scattering events

The scattering events occurring at the surface after the chromium deposition are studied in this section. Subsection 5.4.1 investigates the QPIs of the surface states. Subsection 5.4.2 shows the energy dispersion of the surface states in the $\bar{\Gamma} - \bar{\mathrm{M}}$ direction. From the dispersion, the fermion velocity v_F and the Dirac point energy E_D are estimated.

5.4.1 Quasiparticle interference patterns

Figure 5.11 shows the surface topography and its corresponding conductance map. The QPIs originate from scattering events due to the native defects 1 and 3 and to the new chromium features. Several of these LDOS maps are taken at different bias voltages. Fourier transforms of the maps are shown in figure 5.12.

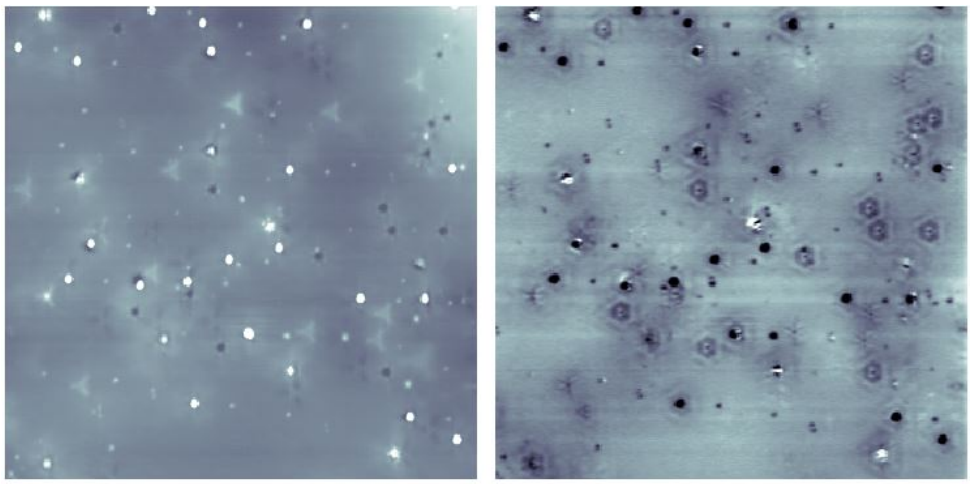

Figure 5.11: (left) 70×70 nm^2 STM topography image of the Bi_2Te_3 surface after atomic chromium deposition at $I = 0.3$ nA and $V = 700$ mV. (right) The corresponding LDOS map, showing the formation of standing waves at the surface.

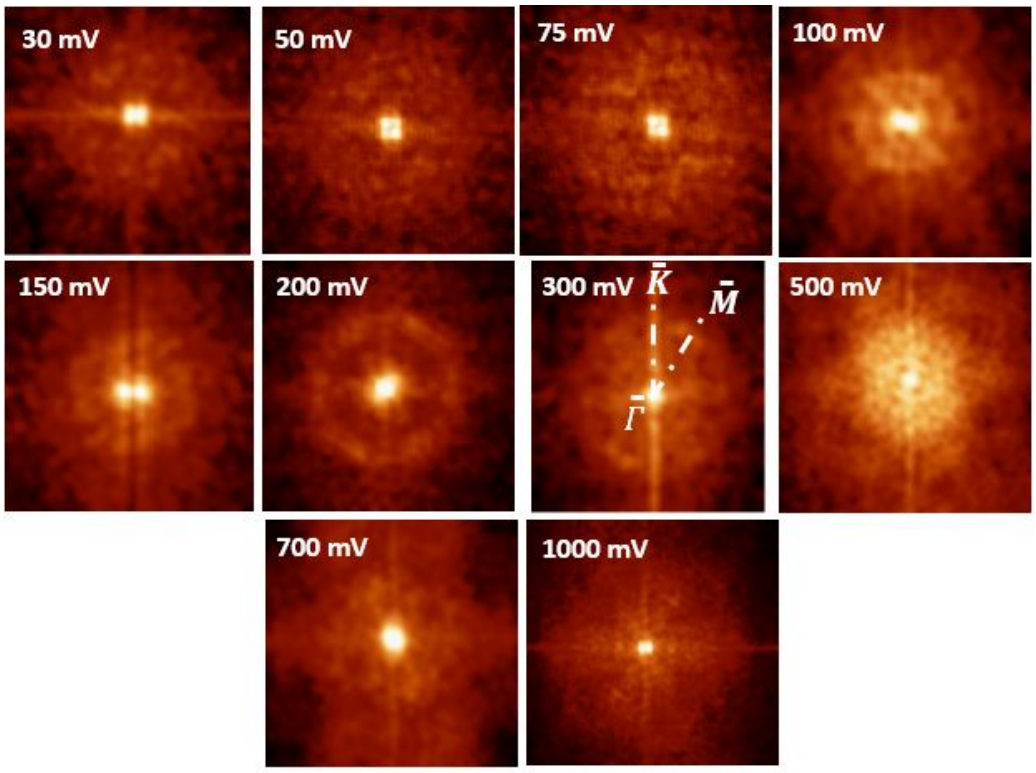

Figure 5.12: The Fourier transforms of conductance maps measured at $V = 30$, 50, 75, 100, 150, 200, 300, 500, 700 and 1000 mV. The images are about 1×1 1/nm^2 in size.

The Fourier transforms make the periodicity of the patterns more visible. They show a hexagonal symmetry in reciprocal space, associated with the symmetry of the lattice in real space. Compared to the bare surface (see subsection 3.5), the scattering seems more uniform in direction. However, the Fourier images are not extremely clear, making it difficult to make absolute statements about allowed or forbidden scattering directions. It is possible that the introduction of magnetic impurities (the deposited chromium atoms) makes it possible for surface state electrons to backscatter. As was the case after the cobalt deposition (see subsection 4.4), there is also some smearing in the radial direction. While the reason for this radial smearing is not clear, the fact that this phenomenon occurs after both depositions might help in understanding its origin.

5.4.2 Energy dispersion relation of the surface states

Using information from the Fourier transforms in figure 5.12, the dispersion of energy as a function of q in the $\bar{\Gamma} - \bar{\mathrm{M}}$ direction can be determined for the surface states. The result is shown in figure 5.13. The errors on the q-values are determined by the resolution of the Fourier transform images. The best fit to the data (shown as a red line on the figure) demonstrates that the dispersion is indeed linear, as expected for the Dirac fermions. The dispersion relation is given by

$$E = aq + b,$$

where $a = 220 \pm 30$ meV nm and $b = -210 \pm 90$ meV. The quality of the fit is quantified by an R^2-value of 0.9794.

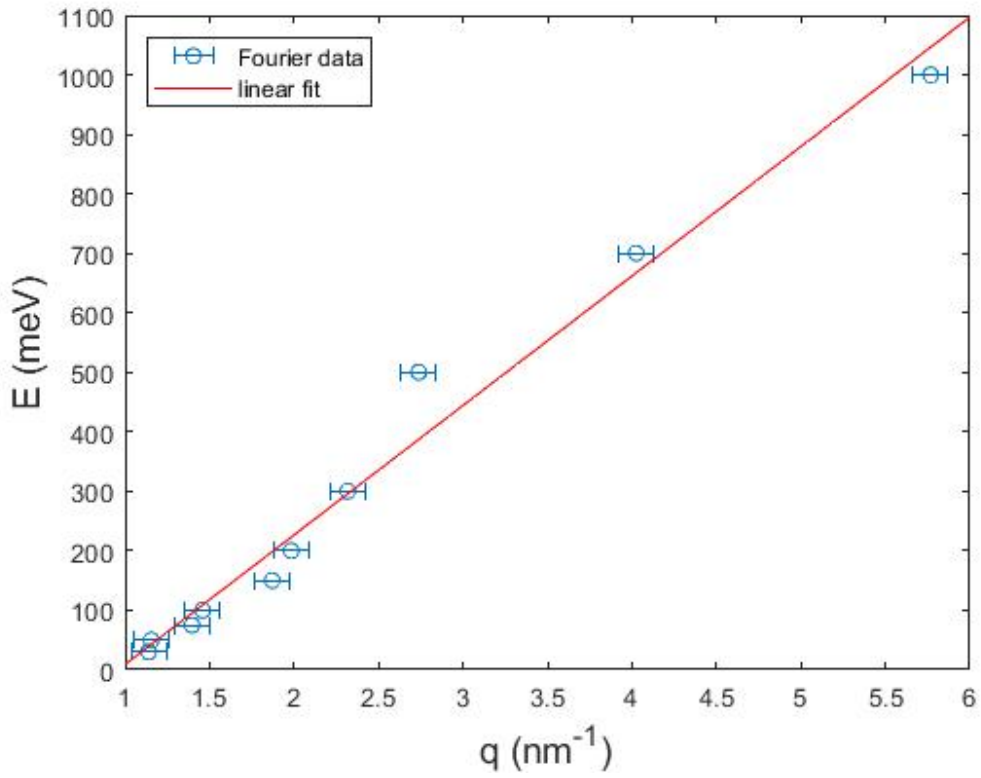

Figure 5.13: The $E(q)$-dispersion in the $\bar{\Gamma} - \bar{\mathrm{M}}$ direction for the surface of Bi_2Te_3 after atomic chromium deposition.

Using this dispersion, the Dirac fermion velocity and the Dirac point energy are calculated to be the following.

$$v_F = \frac{1}{\hbar}\frac{\mathrm{d}E}{\mathrm{d}k} = \frac{1}{\sqrt{3}\hbar}\frac{\mathrm{d}E}{\mathrm{d}q} = \frac{1}{\sqrt{3}\hbar}a = (1.9 \pm 0.2) \times 10^5 \text{ m/s},$$
$$E_D = b = -210 \pm 90 \text{ meV}.$$

The Dirac fermion velocity agrees with the group velocites found at the bare surface and after the cobalt deposition (see subsections 3.5.2 and 4.4.2), where they were determined to be $v_F = (2.1 \pm 0.4) \times 10^5$ m/s and $v_F = (2.0 \pm 0.2) \times 10^5$ m/s. The Dirac point energy is comparable to the one calculated after the cobalt deposition, which is $E_D = -220 \pm 70$ meV. As was the case after the cobalt deposition, the Dirac point shifts to a higher energy compared to the bare surface ($E_D = -260 \pm 90$ meV). This indicates that the deposited chromium atoms induce some doping.

5.5 Chapter summary

This chapter presents the results of the surface characterization of the topological insulator Bi_2Te_3 after atomic chromium deposition using STM and STS.

Topography of the surface reveals both new features arising due to the deposited chromium atoms and the native defects seen at the bare surface. As was the case after the atomic cobalt deposition, the newly arising features can be divided into two categories. The features in the first category are protrusions on the surface with a spherical shape and appear with different sizes. These features are assumed to be chromium atoms and small clusters of chromium atoms. The second category consists of features whose structures are more geometric. They are believed to be caused by chromium atoms substituting bismuth atoms at the second atomic layer, but one needs simulations to confirm this hypothesis. A statistical analysis of the native defects reveals that, similarly to after the cobalt deposition, the frequency of defects 3 and 5 drop down to half of their value at the bare surface. Since 3 is a tellurium vacancy at the first atomic layer ($V_{Te,1}$), this drop might indicate some interaction between the deposited atoms and the vacancies. It is not that straightforward o formulate a hypothesis explaining the frequency drop of defect 5, which is a bismuth atom substituting a tellurium atom at the sixth atomic layer ($V_{Te,6}$) as this defect is not found immediately at the surface.

Conductance maps of the surface show quasiparticle interference patterns. Compared to the bare surface, the scattering patterns are more uniform in direction. It is probable that the introduction of the chromium atoms makes it possible for the surface state electrons to backscatter. As after the cobalt deposition, there is also a radial smearing in the Fourier transforms of the LDOS maps. This smearing is not easily understood, but the fact that it occurs after both depositions might help in discovering its origin. The energy dispersion of the surface states along the $\bar{\Gamma} - \bar{\mathrm{M}}$ direction is determined to be linear, as expected for massless Dirac fermions. The fermion velocity and Dirac point energy derived from this dispersion relation are determined as $v_F = (1.9 \pm 0.2) \times 10^5$ m/s and $E_D = -210 \pm 90$ meV. The fermion velocity is in agreement with the values found at both the bare surface

and after the cobalt deposition, which are $(2.1 \pm 0.4) \times 10^5$ m/s and $(2.0 \pm 0.2) \times 10^5$ m/s respectively. The Dirac point energy is higher than at the bare surface (-260 ± 90 meV), which indicates that depositing the chromium atoms results in some doping effect.

Chapter 6

Summary and outlook

In this thesis, the surface of the 3D TI Bi_2Te_3 is examined. In the first part of this work, the bare surface of the 3D TI Bi_2Te_3 is characterized using several surface analysis techniques (STM, STS, AES and LEED). The native defects of the crystal are examined and identified where possible. This is of interest because of the role structural defects play in the doping of TIs. To realize the quantum phenomena expected at the TI surface and for future applications, it is important that the used TIs are intrinsic.

To break time reversal symmetry, great efforts have been made in the magnetic doping of TI materials. While many studies about magnetic bulk doping of TIs have been performed, magnetic doping at the surface has not been this intensively researched. Experimental studies of the interaction of surface magnetic moments with topological states have predominantly been performed using spatially averaging techniques which are not able to probe local phenomena. An investigation using local techniques like scanning tunneling microscopy is thus needed. For this reason, magnetic doping at the surface of the Bi_2Te_3 sample is studied in the second part of this thesis by means of STM and STS.

The results of the work performed in this thesis are summarized in the paragraphs below. Suggestions for further work are considered in the last part of this chapter.

Characterization of the bare surface and identifying native defects

Topography of the sample surface shows several defects and the interatomic distance is determined to be $d = 4.5 \pm 0.1$ Å. The height of a quintuple layer is measured as 1.0 ± 0.1 nm. Using area-averaged spectroscopy, one can see the surface state conductance in a $\mathrm{d}I/\mathrm{d}V$ spectrum. The sample appears to be either intrinsic or slightly p-doped.
Upon studying the native defects more closely, twelve defects are catalogued. Comparison between STM experiments, first-principles simulations and literature allows to identify various native defects, including tellurium vacancies V_{Te}, Bi_{Te} antisites, Te_{Bi} antisites and tellurium interstitial defects Te_i. The most frequent of these defects are tellurium vacancies at the first atomic layer ($V_{Te,1}$) and bismuth atoms substituting tellurium atoms at the fifth atomic layer ($Bi_{Te,5}$). Four native defects could not be identified (yet). One of these unidentified native defects, labelled as defect 1 shows discrete peaks in its spectroscopy and a shift in the vacuum level. Moreover, this defect is mobile. To gain more information about defect 1, AES is performed. The resulting spectrum only shows peaks

due to transitions in bismuth and tellurium atoms. This could either mean that defect 1 is an impurity with a low density, which the Auger setup is not sensitive enough to detect or that defect 1 is an intrinsic defect of the crystal. If it is a native defect, a plausible hypothesis is it being a tellurium interstitial between QLs which finds itself at the surface after cleaving. Further studies with a scanning Auger microscope, as well as DFT based calculations might shed light on this defect's origins. LEED measurements reveal that the sample surface order is restored after being damaged due to Ar^+ sputtering. The restored surface has the same structure as the in-situ (UHV) cleaved surface measured by STM.

Characterization after depositing magnetic atoms

This paragraph presents the results of the surface characterization of the topological insulator Bi_2Te_3 after atomic cobalt and chromium deposition using STM and STS.
After the magnetic cobalt (chromium) deposition, topography of the sample surface shows that while the structural defects of the crystal are still visible, there are also some new features. These new features can be divided into two categories. The features in the first category are protrusions on the surface with a spherical shape and appear with different sizes. These features are assumed to be cobalt (chromium) atoms and small clusters of cobalt (chromium) atoms. The second category of features are more geometric in their structure. It is possible that these second category features can be explained as substitution of bismuth atoms in the second atomic layer by cobalt or chromium atoms, but this hypothesis can only be verified or disproven with the help of ab initio calculations.
After both depositions, a statistical analysis of the most occurring native defects reveal that frequency of defect 3 ($V_{Te,1}$) drops to half its value at the bare surface, which might indicate some partial participation of this defect in the formation of new features. The frequency of defect 5 ($Bi_{Te,6}$) also drops down to half of its value at the bare surface after both depositions. For the cobalt deposition, there is not enough data for defect 5 to say this drop is a reliable observation. For the frequencies counted after the chromium deposition however, there is enough data to make this observation robust. This also makes it more plausible that the observation after the cobalt deposition is correct. For this defect, which is a bismuth atom substituting a tellurium atom at the sixth atomic layer ($V_{Te,6}$), it is not that straightforward to formulate a hypothesis explaining this observation since this defect is not found immediately at the surface.

Scattering events at the surface

To study scattering events, conductance maps of the surface are measured. At the bare surface, these maps display spatial modulations due to scattering from the native defects, with the main scatter centers being ($V_{Te,1}$) and the unidentified defect 1. This is not unexpected, since both exist at the first atomic layer. After the cobalt deposition, this is slightly different. While the main scattering centers of the bare surface (defect 1 and defect 3, which is $V_{Te,1}$) are still visible, there are also scattering events arising due cobalt features. The interference patterns after the cobalt deposition show different wavelengths. For conductance maps taken after the atomic chromium deposition, there are also scattering centers due to chromium features next to those due to native defects 1 and 3.
Since the periodicity of the patterns is clearer in reciprocal space, the Fourier transforms of the LDOS maps are studied. In general, these Fourier transforms appear quite diffuse,

making it hard to make definite statements about them. This could be due to relatively few scattering events occurring or contributions from bulk states. At the bare surface, the Fourier images show that scattering in the $\bar{\Gamma} - \bar{\mathrm{M}}$ direction of the surface Brillouin zone dominate over scattering in the $\bar{\Gamma} - \bar{\mathrm{K}}$ direction at some voltages, indicating a suppression of backscattering. At higher energies, the Fourier transforms of the conductance maps are warped. This is explained by the surface band structure of Bi_2Te_3, which is warped due to a spin-orbit coupling term at the surface. After both the cobalt and chromium deposition the scattering patterns appear more uniform in direction than at the bare surface. It is plausible that deposited cobalt (or chromium) atoms make it possible for surface state electrons to backscatter and time reversal symmetry is broken. Aside from this spreading in the angular direction, which is indicative of backscattering, there is also some spread in the radial direction. Interpreting the meaning of this radial spread is not straightforward. Through the Fourier transforms, the dispersion relation for the surface states along the $\bar{\Gamma} - \bar{\mathrm{M}}$ direction is obtained. This is done for the bare surface, after the atomic cobalt deposition and after the atomic chromium deposition (see figure 6.1).

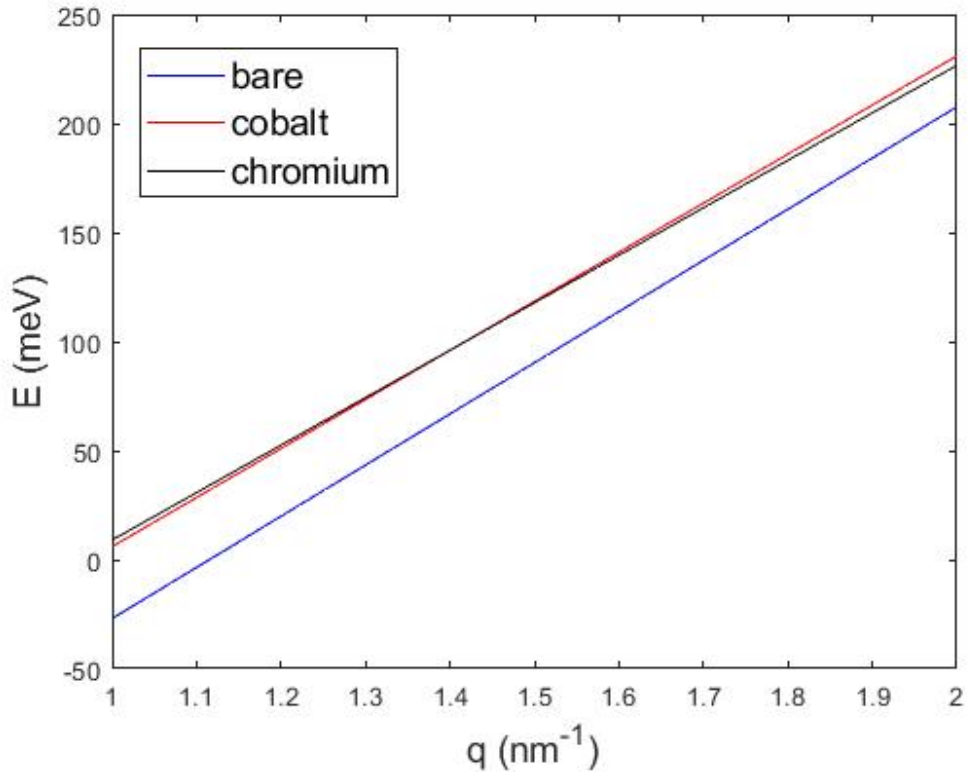

Figure 6.1: The $E(q)$-dispersion in the $\bar{\Gamma}-\bar{\mathrm{M}}$ direction for the bare surface of Bi_2Te_3 (blue), after atomic cobalt deposition (red) and after atomic chromium deposition (black).

This dispersion is linear at the bare surface, as expected for massless Dirac fermions. This remains the case after the atomic depositions. The Dirac fermion velocity and the Dirac point energy are be estimated and shown in table 6.1.

Table 6.1: Fermion group velocity and Dirac point energy calculated at the bare surface, after atomic cobalt deposition and after atomic chromium deposition.

	v_F ($\times 10^5$ m/s)	E_D (meV)
bare surface	2.1 ± 0.4	-260 ± 90
cobalt	2.0 ± 0.2	-220 ± 70
chromium	1.9 ± 0.2	-210 ± 90

The different fermion velocities are in agreement with each other and with values determined from ARPES measurements. The negative Dirac point energy at the bare surface indicates that the native defects do not act to bring the Dirac point out of the valence band. While still negative, the calculated Dirac point energies after the magnetic atom depositions are higher in energy than that at the bare surface: there is some doping effect, but it is not large enough to bring the Dirac point out of the valence band and into the energy gap.

Outlook

The experimental results presented in this thesis are important for the understanding of the interaction between the surface of 3D TIs and magnetic surface dopants. As mentioned previously, further identification of the native defects of Bi_2Te_3 can be achieved by means of scanning Auger microscopy. In addition, further DFT calculations can shed light on the origin of the not yet identified defects. The same can be said for features arising after the magnetic atom depositions: ab initio calculations are needed to verify whether these defects are indeed magnetic atoms diffusing to lower atomic layers. From the experiments performed in this work, it is plausible that time reversal symmetry is broken. To gain a better understanding, measurements with spin-polarized STM would be interesting as this technique can probe the spin scattering. It would also be beneficial to perform ARPES measurements, as this technique allows to directly visualize opening of the gap at the Dirac point.

To better understand the interaction between the crystal and the deposited impurities, it is important to realize that the growth conditions of the bulk crystal have an effect on its electronic properties. For this reason, a repetition of the experiments in this thesis with another Bi_2Te_3 sample grown under different conditions is an interesting proposal. Thin TI films of several QLs grown by molecular beam epitaxy are good candidates for this, since they are shown to host less native defects [119, 120]. Transfer of these samples to a STM setup is challenging. For this purpose, all measurements have to be performed in-situ in an integrated system. While the surface properties can be varied in this way, the properties of the deposited impurities can also be altered. This could be done by varying the deposited amount of atoms. By depositing for a longer time, the density of the atoms will be higher and this will likely affect the interaction. For cobalt and chromium atoms deposited on a gold surface, it has been reported that the atoms self-organize into small islands [121, 122]. It is worthwhile to deposit for a longer time and see if this phenomenon also occurs at the Bi_2Te_3 surface. Another possibility to modify the properties of the

magnetic impurities is to deposit size-selected clusters. Small clusters are intriguing because their properties depend strongly on the exact size and composition (meaning the exact number and type of atoms in the cluster). Cobalt clusters are one of the most interesting examples because of their magnetic properties [123–127]. For cobalt clusters consisting of up to six atoms it was found that the total spin magnetic moment rises as the number of atoms in the clusters increases [128]. The magnetic scattering of electrons due to cobalt clusters is thus different from the magnetic scattering of electrons due to single cobalt atom and because the magnetic properties of small cobalt clusters depend on their size so strongly, the scattering mechanisms of electrons with these clusters are also size-dependent. This makes it interesting to exactly control the size of clusters on the Bi_2Te_3 surface. Since the atomic depositions considered in this thesis are performed at room temperature, the atoms are mobile and form small clusters. This formation of clusters does however not happen in a very controlled way. To deposit size-selected cobalt clusters in a controlled way, the KU Leuven magnetron sputtering cluster setup can be used [129]. Characterization by STM can be done after transferring, but as mentioned before, this is challenging. One could also repeat the atomic depositions using materials with a magnetic moment other than cobalt or chromium.

A next step in this research could be investigating the magnetic properties of the deposited magnetic impurities. This could be done through spin-polarized STM and STS or X-ray magnetic circular dichroism [130], as both of these techniques are surface sensitive.

Appendix: basics of the topology in topological insulators

In this appendix, the notions of Berry phase, Berry connection and Berry curvature are introduced. Using these quantities, the topological invariant used to distinguish between topological and ordinary insulators is constructed. The material in this appendix is based on [36, 39].

Berry phase

The notion of Berry phase is important in the discussions of topological phases. Here, its definition and meaning are briefly discussed.

Let $\mathbf{R}(t)$ be a set of time-dependent parameters and consider it as a vector in the parameter space. The Hamiltonian of a system specified by the parameter $\mathbf{R}(t)$ is written as $H[\mathbf{R}(t)]$ and its n-th eigenstate as $|n, \mathbf{R}(t)\rangle$. The Schrödinger equation for this system is given by

$$H[\mathbf{R}(t)]\,|n, \mathbf{R}(t)\rangle = E_n[\mathbf{R}(t)]\,|n, \mathbf{R}(t)\rangle\,.$$

When $\mathbf{R}(t)$ changes adiabatically from the $t = 0$ value $\mathbf{R_0}$, the time evolution of the state follows

$$H[\mathbf{R}(t)]\,|n, t\rangle = i\hbar\frac{\partial}{\partial t}\,|n, t\rangle\,,$$

in which the state at time t is given by

$$|n, t\rangle = \exp\left(\frac{i}{\hbar}\int_0^t \mathrm{d}t' L_n[\mathbf{R}(t')]\right)|n, \mathbf{R}(t)\rangle\,,$$

with

$$L_n[\mathbf{R}(t)] = i\hbar\dot{\mathbf{R}}(t)\cdot\langle n, \mathbf{R}(t)|\,\nabla_R\,|n, \mathbf{R}(t)\rangle - E_n[\mathbf{R}(t)].$$

Using this definition of $L_n[\mathbf{R}(t)]$, one may write the time-dependent state as

$$|n, t\rangle = \exp\left(-\int_0^t \mathrm{d}t'\dot{\mathbf{R}}(t')\cdot\langle n, \mathbf{R}(t')|\,\nabla_R\,|n, \mathbf{R}(t')\rangle\right)|n, \mathbf{R}(t)\rangle \times \exp\left(\frac{i}{\hbar}\int_0^t \mathrm{d}t' E_n[\mathbf{R}(t')]\right)$$

In this expression of $|n, t\rangle$, the first exponential term represents the nontrivial effect of the quantum-mechanical phase accumulated during the time evolution, and the last exponential term is a trivial one called the dynamical term. When $\mathbf{R}$ moves on a closed loop C from $t = 0$ and returns to the original position at $t = T$, such that $\mathbf{R}(T) = \mathbf{R}_0$, the Berry phase $\gamma_n[C]$ for this loop C is defined as

$$\begin{aligned}\gamma_n[C] &\equiv \int_0^T \mathrm{d}t\dot{\mathbf{R}}(t)\cdot i\left\langle n,\mathbf{R}(t)\right|\nabla_R\left|n,\mathbf{R}(t)\right\rangle \\ &= \oint_C \mathrm{d}\mathbf{R}\cdot i\left\langle n,\mathbf{R}(t)\right|\nabla_R\left|n,\mathbf{R}(t)\right\rangle \\ &= -\oint_C \mathrm{d}\mathbf{R}\cdot\mathbf{A}_n(\mathbf{R}) = -\int_S \mathrm{d}\mathbf{S}\cdot\mathbf{B}_n(\mathbf{R}),\end{aligned}$$

where the last equation follows from Stokes' theorem. Here, the Berry connection

$$\mathbf{A}_n(\mathbf{R}) = -i\left\langle n,\mathbf{R}(t)\right|\nabla_R\left|n,\mathbf{R}(t)\right\rangle$$

and its rotation, the Berry curvature

$$\mathbf{B}_n(\mathbf{R}) = \nabla_R\times\mathbf{A}_n(\mathbf{R})$$

are defined.

One can see that the Berry phase takes on the meaning of the accumulated phase factor of a quantum-mechanical system after it completes a closed path in the parameter space. The Berry connection corresponds to the gauge field defined on that parameter space, similar to the vector potential for electromagnetic fields in real space.

TKKN invariant

The topological invariant defined for the integer quantum Hall system is the TKKN invariant, named after Thouless, Kohmoto, Nightingale and den Nijs. It is closely related to the Berry phase. To see this, it is derived by calculating the Hall conductivity of a 2D electron system of size $L\times L$ in perpendicular magnetic fields, where the electric field E and the magnetic field B are applied along the y- and z-axes, respectively. By treating the effect of the electric field E as a perturbation potential $V=-eEy$, one may use the perturbation theory to approximate the perturbed eigenstate $\left|n\right\rangle_E$ as

$$\left|n\right\rangle_E = \left|n\right\rangle + \sum_{m(\neq n)}\frac{\left\langle m\right|(-eEy)\left|n\right\rangle}{E_n-E_m}\left|m\right\rangle + \ldots.$$

Using this perturbed eigenstate, one may obtain the expectation value of the current density along the x-axis, j_x, in the presence of the E field along the y-axis as

$$\begin{aligned}\left\langle j_x\right\rangle_E &= \sum_n f_n(E_n)\left\langle n\right|_E\left(\frac{ev_x}{L^2}\right)\left|n\right\rangle_E \\ &= \left\langle j_x\right\rangle_{E=0} + \frac{1}{L^2}\sum_n f_n(E_n) \\ &\qquad\times\sum_{m(\neq n)}\left(\frac{\left\langle n\right|ev_x\left|m\right\rangle\left\langle m\right|(-eEy)\left|n\right\rangle}{E_n-E_m} + \frac{\left\langle n\right|(-eEy)\left|m\right\rangle\left\langle m\right|ev_x\left|n\right\rangle}{E_n-E_m}\right),\end{aligned}$$

where v_x is the electron velocity along the x-direction and $f(E_n)$ is the Fermi distribution function. The Heisenberg equation of motion $\frac{d}{dt}y = v_y = \frac{1}{i\hbar}[H, y]$ leads to

$$\langle m| v_y |n\rangle = \frac{1}{i\hbar}(E_n - E_m) \langle m| y |n\rangle ,$$

which allows one to evaluate the Hall conductivity as

$$\sigma_{xy} = \frac{\langle j_x \rangle_E}{E} = -\frac{i\hbar e^2}{L^2} \sum_n f_n(E_n) \times \sum_{m(\neq n)} \frac{\langle n| v_x |m\rangle \langle m| v_y |n\rangle - \langle n| v_y |m\rangle \langle m| v_x |n\rangle}{(E_n - E_m)^2}.$$

When considering a system a system in a periodic potential like a crystal with Bloch states $|u_{n\mathbf{k}}\rangle$ as the eigenstates, the identity

$$\langle u_{m\mathbf{k}'}| v_\mu |u_{n\mathbf{k}}\rangle = \frac{1}{\hbar} (E_{n\mathbf{k}} - E_{m\mathbf{k}'}) \langle u_{m\mathbf{k}'}| \frac{\partial}{\partial k_\mu} |u_{n\mathbf{k}}\rangle$$

allows one to rewrite σ_{xy} into the form

$$\sigma_{xy} = -\frac{i\hbar e^2}{L^2} \sum_{\mathbf{k}} \sum_{n(\neq m)} f_n(E_{n\mathbf{k}}) \times \left(\frac{\partial}{\partial k_x} \langle u_{n\mathbf{k}}| \frac{\partial}{\partial k_y} u_{n\mathbf{k}}\rangle - \frac{\partial}{\partial k_y} \langle u_{n\mathbf{k}}| \frac{\partial}{\partial k_x} u_{n\mathbf{k}}\rangle \right).$$

The Berry connection $\mathbf{A}_n(\mathbf{R}) = -i \langle n, \mathbf{R}(t)| \nabla_R |n, \mathbf{R}(t)\rangle$ is written as

$$\mathbf{a}_n(\mathbf{k}) = -i \langle u_{n\mathbf{k}}| \nabla_k |u_{n\mathbf{k}}\rangle = -i \langle u_{n\mathbf{k}}| \frac{\partial}{\partial \mathbf{k}} |u_{n\mathbf{k}}\rangle$$

for Bloch states, and so the Hall conductivity reduces to

$$\sigma_{xy} = N\frac{e^2}{h}$$

where

$$N = \sum_n \int_{\mathrm{BZ}} \frac{\mathrm{d}^2\mathbf{k}}{2\pi} \left(\frac{\partial a_{n,y}}{\partial k_x} - \frac{\partial a_{n,x}}{\partial k_y} \right).$$

This N can be expressed as $N = \sum_n \nu_n$, in which ν_n is the contribution from the n-th energy band, also known as the energy band's Chern number. One can see that ν_n is related to the Berry phase through

$$\begin{aligned} \nu_n &= \int_{\mathrm{BZ}} \frac{\mathrm{d}^2\mathbf{k}}{2\pi} \left(\frac{\partial a_{n,y}}{\partial k_x} - \frac{\partial a_{n,x}}{\partial k_y} \right) \\ &= \frac{1}{2\pi} \oint_{\partial \mathrm{BZ}} \mathrm{d}\mathbf{k} \cdot \mathbf{a}_n(\mathbf{k}) \\ &= -\frac{1}{2\pi} \gamma_n[\partial \mathrm{BZ}]. \end{aligned} \tag{6.1}$$

Because of the single-valued nature of the wave function, its change in the phase factor after encircling the Brillouin zone boundary ∂BZ can only be an integer multiple of 2π, which means

$$\gamma_n[\partial \mathrm{BZ}] = 2\pi m, \quad (m \in \mathbb{Z}).$$

Because of this, ν_n can only take integer values, leading to σ_{xy} being quantized to integer multiples of e^2/h.

The integer N is called the TKKN invariant, and it plays the role of the topological invariant of the quantum Hall system, which is a time reversal symmetry breaking TI. From equation 6.1, it is clear that N becomes nonzero (meaning the system is in the topological phase) only when the Berry connection $\mathbf{a}_n(\mathbf{k})$ is not a single-valued function.

Bibliography

[1] F. Ortmann, S. Roche and S.O. Valenzuela, editor. *Topological Insulators: fundamentals and perspectives*. Wiley-VCH, Weinheim, Germany, 2015.

[2] H. Zhang, C.-X. Liu, X.-L. Qi, X. Dai, Z. Fang and S.-C. Zhang. Topological insulators in Bi_2Se_3, Bi_2Te_3 and Sb_2Te_3 with a single Dirac cone on the surface. *Nature Physics*, 5(438), 2009.

[3] L. He, X. Kou and K.L. Wang. Review of 3D topological insulator thin-film growth by molecular beam epitaxy and potential applications. *Physica Status Solidi RRL*, 7(50), 2013.

[4] O. Eibl, K. Nielsch, N. Peranio and F. Völkein. *Thermoelectric Bi_2Te_3 Nanomaterials*. Wiley-VCH, Weinheim, Germany, 2015.

[5] Y. Ando. Topological Insulator Materials. *Journal of the Physical Society of Japan*, 82, April 2013.

[6] J. Zhang, C.-Z. Chang, Z. Zhang, J. Wen, X. Feng, K. Li, M. Liu, K. He, L. Wang, X. Chen, Q.-K. Xue, X. Ma and Y. Wang. Band structure engineering in $(Bi_{1x}Sb_x)_2Te_3$ ternary topological insulators. *Nature Communications*, 2, December 2011.

[7] Z. Ren, A.A. Taskin, S. Sasaki, K. Segawa and Y. Ando. Large bulk resistivity and surface quantum oscillations in the topological insulator Bi_2Te_2Se. *Phys. Rev. B*, 82, December 2010.

[8] D. Hsieh, Y. Xia, D. Qian, L. Wray, J. H. Dil, F. Meier, J. Osterwalder, L. Patthey, J. G. Checkelsky, N. P. Ong, A. V. Fedorov, H. Lin, A. Bansil, D. Grauer, Y. S. Hor, R. J. Cava and M. Z. Hasan. A tunable topological insulator in the spin helical Dirac transport regime. *Nature*, 460:1101–1105, 2009.

[9] D. Kim, S. Cho, N.P. Butch, P. Syers, K. Kirshenbaum, S. Adam, J. Paglione and M.S. Fuhrer. Surface conduction of topological Dirac electrons in bulk insulating Bi_2Se_3. *Nature Physics*, 8:459–463, April 2012.

[10] M. Eschbach, E. Młyńczak, J. Kellner, J. Kampmeier, M. Lanius, E. Neumann, C. Weyrich, M.s Gehlmann, P. Gospodarič, S. Döring, G. Mussler, N. Demarina, M. Luysberg, G. Bihlmayer, T. Schäpers, L. Plucinski, S. Blügel, M. Morgenstern, C.M. Schneider and D. Grützmacher. Realization of a vertical topological p-n junction in epitaxial Sb_2Te_3/Bi_2Te_3 heterostructures. *Nature Communications*, 6, November 2015.

[11] H. Beidenkopf, P. Roushan, J. Seo, L. Gorman, I. Drozdov, Y.S. Hor, R.J. Cava and A. Yazdani. Spatial fluctuations of helical Dirac fermions on the surface of topological insulators. *Nature Physics*, 7:939–943, October 2011.

[12] Y.L. Chen, J.H. Chu, J.G. Analytis, Z.K. Liu, K. Igarashi, H.H. Kuo, X.L. Qi, S.K. Mo, R.G. Moore, D.H. Lu, M. Hashimoto, T. Sasagaw, S.C. Zhang, I.R. Fisher, Z. Hussain and Z.X. Shen. Massive Dirac fermion on the surface of a magnetically doped topological insulator. *Science*, 329, 2010.

[13] Y. Okada, C. Dhital, W. Zhou, E.D. Huemiller, H. Lin, S. Basak, A. Bansil, Y.-B. Huang, H. Ding, Z. Wang, S.D. Wilson and V. Madhavan. Direct Observation of Broken Time-Reversal Symmetry on the Surface of a Magnetically Doped Topological Insulator. *Phys. Rev. Lett.*, 106:206805, May 2011.

[14] J.S. Dyck, W. Chen, P. Hájek, P. Lošták and C. Uher. Low-temperature ferromagnetism and magnetic anisotropy in the novel diluted magnetic semiconductor $Sb_{2-x}V_xTe_3$. *Physica B: Condensed Matter*, 312-313:820–822, March 2002.

[15] J.S. Dyck, P. Hájek, P. Lošták and C. Uher. Diluted magnetic semiconductors based on $Sb_{2-x}V_xTe_3$ ($0.01 < x < 0.03$). *Phys. Rev. B*, 65, March 2002.

[16] J.S. Dyck, Č. Drašar, P. Lošták and C. Uher. Low-temperature ferromagnetic properties of the diluted magnetic semiconductor $Sb_{2-x}Cr_xTe_3$. *Phys. Rev. B*, 71, March 2005.

[17] J.S. Dyck, P.Švanda, P. Lošták, J. Horák, W. Chen and C. Uher. Magnetic and transport properties of the V_2-VI_3 diluted magnetic semiconductor $Sb_{2-x}Mn_xTe_3$. *Journal of Applied Physics*, 94, 2003.

[18] J. Choi, S. Choi, J. Choi, Y. Park, H.-M. Park, H.-W. Lee, B.-C. Woo and S. Cho. Magnetic properties of Mn-doped Bi_2Te_3 and Sb_2Te_3. *Phys. Status Solidi B*, 241, 2004.

[19] Y.S. Hor, P. Roushan, H. Beidenkopf, J. Seo, D. Qu, J.G. Checkelsky, L.A. Wray, D. Hsieh, Y. Xia, S.-Y. Xu, D. Qian, M.Z. Hasan, N.P. Ong, A. Yazdani and R.J. Cava. Development of ferromagnetism in the doped topological insulator $Bi_{2-x}Mn_xTe_3$. *Phys. Rev. B*, 81, 2010.

[20] V.A. Kulbachinskii, A.Y. Kaminskii, K. Kindo, Y. Narumi, K. Suga, P. Lošták and P. Švanda. Ferromagnetism in new diluted magnetic semiconductor $Bi_{2-x}Fe_xTe_3$. *Physica B: Condensed Matter*, 311, 2002.

[21] R. Yu, W. Zhang, H.-J. Zhang, S.-C. Zhang, X. Dai and Z. Fang. Quantized Anomalous Hall Effect in Magnetic Topological Insulators. *Science*, 329(5987):61–64, July 2010.

[22] Q. Liu, C.-X. Liu, C. Xu, X.-L. Qi and S.-C. Zhang. Magnetic Impurities on the Surface of a Topological Insulator. *Phys. Rev. Lett.*, 102, 2009.

[23] L.A. Wray, S.-Y. Xu, Y. Xia, D. Hsieh, A.V. Fedorov, H. Lin, A. Bansil, Y. S. Hor, R.J. Cava and M.Z. Hasan. A topological insulator surface under strong Coulomb, magnetic and disorder perturbations. *Nature Physics*, 7:32–37, 2011.

[24] T. Valla, Z.-H. Pan, D. Gardner, Y.S. Lee and S. Chu. Photoemission spectroscopy of magnetic and nonmagnetic impurities on the surface of the Bi_2Se_3 topological insulator. *Phys. Rev. Lett.*, 108, 2012.

[25] M.R. Scholz, J. Sánchez-Barriga, D. Marchenko, A. Varykhalov, A. Volykhov, L.V. Yashina and O. Rader. Tolerance of Topological Surface States towards Magnetic Moments: Fe on Bi_2Se_3. *Phys. Rev. Lett.*, 108, 2012.

[26] L.R. Shelford, T. Hesjedal, L. Collins-McIntyre, S.S. Dhesi, F. Maccherozzi and G. van der Laan. Electronic structure of Fe and Co magnetic adatoms on Bi_2Te_3 surfaces. *Phys. Rev. B*, 86, 2012.

[27] P. Sessi, F. Resi, T. Bathon, K.A. Kokh, O.E. Tereshchenko and M. Bode. Signatures of Dirac fermion-mediated magnetic order. *Nature Communications*, 5, 2014.

[28] F. Bloch. Über die Quantenmechanik der Elektronen in Kristallgittern. *Zeitschrift fur Physik*, 52:555–600, July 1929.

[29] F. Mandl and G. Shaw. *Quantum Field Theory.* John Wiley & Sons, Ltd., The Atrium, Southern Gate, Chichester, West Sussex, PO19 8SQ, United Kingdom, 2 edition, July 2010.

[30] M.Z. Hasan and C.L. Kane. Colloquium: Topological insulators. *Review of Modern Physics*, 82, October-December 2010.

[31] E.H. Hall. On a New Action of the Magnet on Electric Currents. *American Journal of Mathematics*, 2(5851):287–292, September 1879.

[32] K. von Klitzing, G. Dorda and M. Pepper. New Method for High-Accuracy Determination of the Fine-Structure Constant Based on Quantized Hall Resistance. *Phys. Rev. Lett.*, 45(494), August 1980.

[33] K. von Klitzing. Developments in the quantum Hall effect. *Philosophical Transactions of the Royal Society A: Mathematical, Physical and Engineering Sciences*, 363, August 2005.

[34] S.D. Sarma and A. Pinczuk. *Perspectives in Quantum Hall Effects.* Wiley-VCH, Weinheim, Germany, 2004.

[35] M. Nakahara. *Geometry, Topology and Physics.* Institute of Physics Publishing, Dirac House, Temple Back, Bristol BS1 6BE, UK, second edition, 2003.

[36] D.J. Thouless, M. Kohmoto, M.P. Nightingale and M. den Nijs. Quantized Hall Conductance in a Two-Dimensional Periodic Potential. *Phys. Rev. Lett.*, 49(405), August 1982.

[37] V. Guillemin and A. Pollack. *Differential topology.* AMS Chelsea Publishing, Providence, Rhode Island, 1974.

[38] M. Onoda and N. Nagaosa. Quantized Anomalous Hall Effect in Two-Dimensional Ferromagnets: Quantum Hall Effect in Metals. *Phys. Rev. Lett.*, 90, May 2003.

[39] M.V. Berry. Quantal phase factors accompanying adiabatic changes. *Proceedings of the Royal Society of London. A.*, 392, March 1984.

[40] C.L. Kane and J.E. Moore. Topological insulators. *Physics World*, 24, 2011.

[41] I.I. Geru. Time Reversal in Classical and Relativistic Physics. In *Time-Reversal Symmetry: Seven Time-Reversal Operators for Spin Containing Systems*, pages 1–31. Springer International Publishing, Cham, 2018.

[42] C.L. Kane and E.J. Mele. Quantum Spin Hall Effect in Graphene. *Phys. Rev. Lett.*, 95:32–36, November 2005.

[43] D.J. Griffiths. *Introduction to quantum mechanics*, volume 1. Pearson Prentice-Hall, New Jersey, 2005.

[44] R. Winkler. Spin-Orbit Coupling in Solid-State Physics. In *Spin-Orbit Coupling Effects in Two-Dimensional Electron and Hole Systems*, pages 1–6. Springer-Verlag, Berlin Heidelberg, 2003.

[45] C. Wu, B.A. Bernevig and S.-C. Zhang. Helical Liquid and the Edge of Quantum Spin Hall Systems. *Phys. Rev. Lett.*, 96, March 2006.

[46] P.W. Anderson. Absence of diffusion in Certain Random Lattices. *Phys. Rev.*, 109, March 1958.

[47] P.A. Lee and T.V. Ramakrishnan. Disordered electronic systems. *Phys. Mod. Lett.*, 57, April 1985.

[48] H.A. Kramers. Théorie générale de la rotation paramagnétique dans les cristaux. *Proceedings Koninklijke Akademie van Wetenschappen*, 33:959–972, 1930.

[49] L. Fu, C.L. Kane and E.J. Mele. Topological Insulators in Three Dimensions. *Phys. Rev. Lett.*, 98, March 2007.

[50] J.E. Moore and L. Balents. Topological invariants of time-reversal-invariant band structures. *Phys. Rev. B*, 75, March 2007.

[51] R. Roy. Topological phases and the quantum spin Hall effect in three dimensions. *Phys. Rev. B*, 79, May 2009.

[52] L. Fu and C. L. Kane. Topological insulators with inversion symmetry. *Phys. Rev. B*, 76, July 2007.

[53] D. Hsieh, D. Qian, L. Wray, Y. Xia, Y. S. Hor, R. J. Cav and M. Z. Hasan. A topological Dirac insulator in a quantum spin hall phase. *Nature*, 452(970), April 2008.

[54] A. Damascelli, Z.-X. Shen and Z. Hussain. Angle-resolved photoemission spectroscopy of the cuprate superconductors. *Rev. Mod. Phys.*, 75(473), 2003.

[55] Y. Xia, D. Qian, D. Hsieh, L. Wray, A. Pal, H. Lin, A. Bansil, D. Grauer, Y. S. Hor, R. J. Cava and M. Z. Hasan. Observation of a large-gap topological-insulator class with a single Dirac cone on the surface. *Nature Physics*, 5:398, 2009.

[56] D. Hsieh, Y. Xia, D. Qian, L. Wray, F. Meier, J.H. Dil, J. Osterwalder, L. Patthey, A.V. Fedorov, H. Lin, A. Bansil, D. Grauer, Y.S. Hor, R.J. Cava and M.Z. Hasan. Observation of time-reversal-protected single-Dirac-cone topological-insulator states in Bi_2Te_3 and Sb_2Te_3. *Phys. Rev. Lett.*, 103(14), 2009.

[57] Y.L. Chen, J.G. Analytis, J.-H. Chu, Z.K. Liu, S.-K. Mo, X. L. Qi, H.J. Zhang, D.H. Lu, X. Dai, Z. Fang, S.-C. Zhang, I.R. Fisher, Z. Hussain and Z.-X. Shen. Experimental realization of a three-dimensional topological insulator, Bi_2Te_3. *Science*, 325(5916):178–181, 2009.

[58] J.G. Checkelsky, Y.S. Hor, M.-H. Liu, D.-X. Qu, R.J. Cava and N.P. Ong. Quantum interference in macroscopic crystals of nonmetallic Bi_2Se_3. *Phys. Rev. Lett.*, 103(24), 2009.

[59] Y.S. Hor, A. Richardella, P. Roushan, Y. Xia, J. G. Checkelsky, A. Yazdani, M. Z. Hasan, N.P. Ong and R.J. Cava. P-type Bi_2Se_3 for topological insulator and low-temperature thermoelectric applications. *Phys. Rev.B*, 79(19), 2009.

[60] H. Peng, K. Lai, D. Kong, S. Meister, Y. Chen, X. L. Qi, S. C. Zhang, Z. X. Shen and Y. Cui. Aharonov-Bohm interference in topological insulator nanoribbons. *Nature Materials*, 9(24), 2010.

[61] S.D. Mahanti, P.M. Larson, D. Bile and H. Li. Electronic structure of complex bismuth chalcogenide systems. In G. Kanatzidis, S.D. Mahanti and T.P. Hogan, editor, *Chemistry, Physics, and Materials Science of Thermoelectric Materials: Beyond Bismuth Telluride*, pages 227–247. Kluwer Academic/Plenum Publishers, Boston, 2003.

[62] C. Howard, M. El-Batanouny, R. Sankar and F.C. Chou. Anomalous behavior in the phonon dispersion of the (001) surface of Bi_2Te_3 determined from helium atom-surface scattering measurements. *Phys. Rev. B*, 88, 2013.

[63] Z. Alpichshev, J.G. Analytis, J.-H. Chu, I.R. Fisher, Y.L. Chen, Z.X. Shen, A. Fang and A. Kapitulnik. STM imaging of electronic waves on the surface of Bi_2Te_3: topologically protected surface states and hexagonal warping effects. *Phys. Rev. Lett.*, 104, 2010.

[64] T. Zhang, P. Cheng, X. Chen, J.-F. Jia, X. Ma, K. He, L. Wang, H. Zhang, X. Dai, Z. Fang, X. Xie and Q.-K. Xue. Experimental Demonstration of Topological Surface States Protected by Time-Reversal Symmetry. *Phys. Rev. Lett.*, 103, December 2009.

[65] C.-X. Liu, X.-L. Qi, X. Dai, Z. Fang and S.-C. Zhang. Quantum Anomalous Hall Effect in $Hg_{1-y}Mn_yTe$ Quantum Wells. *Phys. Rev. Lett.*, 101, October 2008.

[66] X.-L. Qi, Y.-S. Wu and S.-C. Zhang. Topological quantization of the spin Hall effect in two-dimensional paramagnetic semiconductors. *Phys. Rev. B*, 74, August 2006.

[67] X.-L. Qi, T.L. Hughes and S.-C. Zhang. Topological field theory of time-reversal invariant insulators. *Phys. Rev. B*, 78, November 2008.

[68] K. Nomura and N. Nagaosa. Surface-Quantized Anomalous Hall Current and the Magnetoelectric Effect in Magnetically Disordered Topological Insulators. *Phys. Rev. Lett.*, 106, April 2011.

[69] M.C. Martíntez-Velart, B. Kretz, M. Moro-Lagares, M.H. Aguirre, T.M. Riedemann, T.A. Lograsso, L. Morellón, M.R. Ibarra, A. Garcia-Lekue and D. Serrate. Chemical Disorder in Topological Insulators: A Route to Magnetism Tolerant Topological Surface States. *Nano Lett.*, 17:4047–4054, 2017.

[70] A.M. Netsou, D.A. Muzychenko, U. Thupakala, A. Seliverstov, T. Chen, F. Song and C. Van Haesendonck. STM/STS study of the magnetically doped topological insulator Bi_2Te_3 by Co surface dopants [abstract]. In D. Alsteens and Y. Dufrêne, editor, *Proceedings of ISPM 2019*. UC Louvain, May 2019.

[71] D.A. Muzychenko *et al*. Density function simulations of native defects in Bi_2Te_3. Unpublished.

[72] K. Schouteden. *Tunneling microscopy and spectroscopy of metallic and magnetic nanoparticles on atomically flat surfaces*. PhD thesis, KU Leuven, November 2008.

[73] G. Binnig, H. Rohrer, C. Gerber and E. Weibel. Surface studies by scanning tunneling microscopy. *Phys. Rev. Lett.*, 49, 1982.

[74] Nobel Prize Committee. The nobel prize in physics 1986. Press release. Available at `https://www.nobelprize.org/prizes/physics/1986/press-release/`.

[75] M. Schmid. The Scanning Tunneling Microscope. TU Wien. Available at `https://www.iap.tuwien.ac.at/www/surface/stm_gallery/stm_schematic`, December 2018.

[76] J. Tersoff and D.R. Hamann. Theory of the scanning tunneling microscope. *Phys. Rev. B*, 31(805), 1985.

[77] M. Bode, M. Dreyer, M. Getzla, M. Kleiber, A. Wadas and R. Wiesendanger. Recent progress in high-resolution magnetic imaging using scanning probe techniques. *J. Phys.: Condens. Matter*, 11, 1999.

[78] J. Bardeen. Tunneling from a many-particle point of view. *Phys. Lett.*, 6, 1961.

[79] I. Giaever. Energy gap in superconductors measured by electron tunneling. *Phys. Rev. Lett.*, 5, 1960.

[80] M.S.J. Marshall and M.R. Castell. Scanning tunnelling microscopy of epitaxial nanostructures. *Chem. Soc. Rev.*, 43:2226–2239, February 2014.

[81] R. Wiesendanger. *Scanning Probe Microscopy and Spectroscopy: Methods and Applications*. Cambridge University Press, Cambridge, 1994.

[82] G. Binnig, K.H. Frank, H. Fuchs, N. Garcia, B. Reihl, H. Rohrer, F. Salvan and A.R. Williams. Tunneling spectroscopy and inverse photoemission: image and field states. *Phys. Rev. Lett.*, 55:991–994, August 1985.

[83] P. Roushan. *Visualizing Surface States of Topological Insulators with Scanning Tunneling Microscopy*. PhD thesis, Princeton University, September 2011.

[84] M. Franz and L. Molenkamp. Topological Insulators. In E. Burstein, A.H. MacDonald and P.J. Stiles, editor, *Contemporary Concepts of Condensed Matter Science*, volume 5. Elsevier B.V., USA, 2018.

[85] M.F. Crommie, C.P. Lutz and D.M. Eigler. Imaging standing waves in a two-dimensional electron gas. *Science*, 363(524), June 1993.

[86] L. Petersen, P.T. Sprunger, P. Hofmann, E. Lægsgaard, B.G. Briner, M. Doering, H.-P. Rust, A.M. Bradshaw, F. Besenbacher and E.W. Plummer. Direct imaging of the two-dimensional fermi contour: Fourier-transform STM. *Phys. Rev. B*, 57(12), March 1998.

[87] Scienta Omicron GmbH. LT STM - The LT STM cryostat. Available at `https://www.scientaomicron.com/en/products/low-temperature-spm/instrument-concept`, May 2019.

[88] M.I. Horcas, R. Fernandez, J.M. Gomez-Rodriguez, J. Colchero, J. Gomez-Herrero and A.M. Baro. WSxM: A software for scanning probe microscopy and a tool for nanotechnology, 2007.

[89] K. Schouteden, K. Govaerts, J. Debehets, U. Thupakula, T. Chen, Z. Li, A. Netsou, F. Song, D. Lamoen, C. Van Haesendonck, B. Partoens and K. Park. Annealing-Induced Bi Bilayer on Bi_2Te_3 Investigated via Quasi-Particle-Interference Mapping. *ACS Nano*, 10(9):8778–8787, 2016.

[90] A. Netsou, U. Thupakula, J. Debehets, T. Chen, B. Hirsch, A. Volodin, Z. Li, F. Song, J.W. Seo, S. De Feyter, K. Schouteden and C. Van Haesendonck. Scanning probe microscopy induced surface modifications of the topological insulator Bi_2Te_3 in different environments. *Nanotechnology*, 28, July 2017.

[91] L. Meitner. Über die Entstehung der β-Strahl-Spektren radioaktiver Substanzen. *Zeitschrift für Physik*, 9:131–144, 1922.

[92] P. Auger. Sur les rayons secondaires produits dans un gaz par des rayons X. *Comptes rendus hebdomadaires des séances de l'Académie des sciences*, 177:169–171, 1923.

[93] K.D. Childs, B.A. Carlson, L.A. LaVanier, J.F. Moulder, D.F. Paul, W.F. Stickle and D.G. Watson. *Handbook of Auger Electron Spectroscopy*. Physical Electronics, Inc., 6509 Flying Cloud Drive, Eden Prairie, MN 55344, USA, 1995.

[94] Institute for Nuclear and KU Leuven Radiation Physics. Surface analysis chamber. Available at `https://fys.kuleuven.be/iks/nvsf/experimental-facilities/surface-analysis-chamber`.

[95] M. Prutton. *Introduction to Surface Physics*. Oxford University Press, Oxford, 1994.

[96] T.B. Rymer. *Electron diffraction*. Methuen, London, 1970.

[97] M. Gulde. Methods and Concepts. In *Development of an Ultrafast Low-Energy Electron Diffraction Setup*, pages 9–25. Springer International Publishing, Cham, 2015.

[98] T.A. Carlson. Photoelectron and Auger spectroscopy. *Physics Today*, 29(53), Augustus 1976.

[99] Institute for Nuclear and KU Leuven Radiation Physics. UHV system. Available at `https://fys.kuleuven.be/iks/nvsf/experimental-facilities/uhv-system`.

[100] J. Dai, D. West, X. Wang, Y. Wang, D. Kwok, S.-W. Cheong, S.B. Zhang and W. Wu1. Toward the Intrinsic Limit of the Topological Insulator Bi_2Se_3. *Phys. Rev. Lett.*, 117, September 2016.

[101] 2D Semiconductors. Bismuth Telluride (Bi_2Te_3). Available at `https://www.2dsemiconductors.com/bismuth-telluride-bi2te3/`, 2019.

[102] M. Nagao. Crystal Growth Techniques for Layered Superconductors. *Condens. Matter*, 2(4), October 2017.

[103] L.-L. Wang, M. Huang, S. Thimmaiah, A. Alam and S.L Bud'ko. Native defects in tetradymite $Bi_2(Te_xSe_{3-x})$ topological insulators. *Phys. Rev. B*, 87, 2013.

[104] A. Hashiboan and C. Elsässer. First-principles density functional theory study of native point defects in Bi_2Te_3. *Phys. Rev. B*, 84, October 2011.

[105] C. Freysoldt, B. Grabowski, T. Hickel, J. Neugebauer, G. Kresse, A. Janotti and C.G. Van de Walle. First-principles calculations for point defects in solids. *Rev. Mod. Phys.*, 86(253), March 2014.

[106] C.G. Van de Walle and J. Neugebaure. First-principles calculations for defects and impurities: Applications to III-nitrides. *Journal of Applied Physics*, 95(8), March 2004.

[107] D.A. Drabold and S.K. Estreicher. Theory of Defects. In *Semiconductors, Topics in Applied Physics*, volume 104. Springer Verlag, Berlin Heidelberg, 2007.

[108] C. Mann, D. West, I. Miotkowski, Y.P. Chen, S. Zhang and C.-K. Shih. Mapping the 3D surface potential in Bi_2Se_3. *Nature Communications*, 4, August 2013.

[109] S. Urazhdin, D. Bilc, S.H. Tessmer, S.D. Mahanti, T. Kyratsi and M.G. Kanatzidis. Scanning tunneling microscopy of defect states in the semiconductor Bi_2Se_3. *Phys. Rev. B*, 66, October 2002.

[110] H. Bando, K. Koizumi, Y. Oikawa, K. Daikohara, V.A. Kulbachinskii and H. Ozaki. The time-dependent process of oxidation of the surface of Bi_2Te_3 studied by X-ray photoelectron spectroscopy. *Journal of Physics: Condensed Matter*, 12(26):5607–5616, June 2000.

[111] J. Krumrain, G. Lussler, S. Borisova, T. Stoica, L. Pluckinski, M. Schneider and D. Grützmacher. MBE growth optimization of topological insulator Bi_2Te_3 films. *Journal of Crystal Growth*, 324(1):115–118, June 2011.

[112] Y. Sakai, M. Kudo and C. Nielsen. Surface potential measurement with high spatial resolution using a scanning Auger electron microscope. *Journal of Vacuum Science & Technology A: Vacuum, Surfaces, and Films*, 19(4):1139–1142, 2001.

[113] S.E. Harrison, B. Zhou, Y. Huo, A. Pushp, A.J. Kellock, S.S.P. Parkin, J.S. Harris, Y. Chen and T. Hesjedal. Preparation of layered thin film samples for angle-resolved photoemission spectroscopy. *Appl. Phys. Lett.*, 105(12):115–118, June 2014.

[114] L. Fu. Hexagonal warping effects in the surface states of the topological insulator Bi_2Te_3. *Phys. Rev. Lett.*, 103(26), December 2009.

[115] Q.-H. Wang and D.-H. Lee. Quasiparticle scattering interference in high-temperature superconductors. *Phys. Rev. B*, 67, January 2003.

[116] M. Ye, S. V. Eremeev, K. Kuroda, E. E. Krasovskii, E. V. Chulkov, Y. Takeda, Y. Saitoh, K. Okamoto, S. Y. Zhu, K. Miyamoto, M. Arita, M. Nakatake, T. Okuda, Y. Ueda, K. Shimada, H. Namatame, M. Taniguchiand A. Kimura. Quasiparticle interference on the surface of 3D topological insulator Bi_2Se_3 induced by cobalt adatom in the absence of ferromagnetic ordering. *Phys. Rev. B*, 85, 2012.

[117] C.Z. Chang, P. Tang, Y.L. Wang, L.L. Wang, X. Chen, C. Liu, W. Duan, K. He, X.C. Ma and Q.K. Xue. Chemical-potential-dependent gap opening at the Dirac surface states of Bi_2Se_3 induced by aggregated substitutional Cr atoms. *Phys. Rev. Lett.*, 112(5), 2014.

[118] W. Zhang, D. West, S.H. Lee, Y. Qiu, C.-Z. Chang, J.S. Moodera, Y.S. Hor, S. Zhang and W. Wu. Electronic Fingerprints of Cr and V Dopants in Topological Insulator Sb_2Te_3. *Phys. Rev. B*, 98, 2018.

[119] J. Krumrain, G. Mussler, S. Borisova, T. Stoica, L. Plucinski, C.M. Schneider and D. Grützmacher. MBE growth optimization of topological insulator Bi_2Te_3 films. *Journal of Crystal Growth*, 324(1):115–118, June 2011.

[120] Y.-Y. Li, G. Wang, X.-G. Zhu, M.-H. Liu, C. Ye, X. Chen, X.-Y. Wang, K. He, L.-L. Wang, X.-C. Ma, H-.J. Zhang, X. Dai, Z. Fang, X.-C. Xie, Y. Liu, X.-L. Qi, J.-F. Jia, S.-C. Zhang and X.-K. Xue. Intrinsic Topological Insulator Bi_2Te_3 Thin Films on Si and Their Thickness Limit. *Advanced Materials*, 22:4002–4007, 2010.

[121] K. Schouteden, D.A. Muzychenko, C. Van Haesendonck. Spin-Polarized Scanning Tunneling Spectroscopy of Self-Organized Nanoscale Co Islands on Au(111) Surfaces. *Journal of Nanoscience and Nanotechnology*, 8(7):3616–3620, 2008.

[122] K. Schouteden, D.A. Muzychenko, P. Lievens, C. Van Haesendonck. Low-Temperature Scanning Tunneling Microscopy and Spectroscopy Investigation of the Electronic Surface State of Self-Organized Cr Islands on Au(111). *Journal of Nanoscience and Nanotechnology*, 9(11):6767–6771, 2009.

[123] D.C. Douglass, A.J. Cox, J.P. Bucher and L.A. Bloomfield. Magnetic properties of free cobalt and gadolinium clusters. *Phys. Rev. B*, 47, May 1993.

[124] I.M.L. Billas, A. Châtelain and W.A. de Heer. Magnetism of Fe, Co and Ni clusters in molecular beams. *Journal of Magnetism and Magnetic Materials*, 168:64–84, May 1997.

[125] D. Gerion, A. Hirt, I.M.L. Billas, A. Châtelain and W.A. de Heer. Experimental specific heat of iron, cobalt, and nickel clusters studied in a molecular beam. *Phys. Rev. B*, 62, 2000.

[126] X. Xu, S. Yin, R. Moro and W.A de Heer. Magnetic moments and adiabatic magnetization of free cobalt clusters. *Phys. Rev. Lett.*, 95, 2005.

[127] C.D. Dong and X.G. Gong. Magnetism enhanced layer-like structure of small cobalt clusters. *Phys. Rev. B*, 78, July 2008.

[128] A. Sebetci. Cobalt clusters (Co_n, $n \leq 6$) and their anions. *Chemical Physics*, 354, 2008.

[129] T. Picot. Magnetron sputtering setup. Available at `https://fys.kuleuven.be/vsm/class/sputter`.

[130] H. Wende and C. Antoniak. X-Ray Magnetic Dichroism. In E. Beaurepaire, H. Bulou, F. Scheurer and K. Jean-Paul, editor, *Magnetism and synchrotron radiation: new trends*, Springer proceedings in physics, 133, chapter 5, pages 145–167. Springer, Berlin, London, 2010.

SOLID STATE PHYSICS AND MAGNETISM
Celestijnenlaan 200d, box 2414
3001 LEUVEN, BELGIË
tel. +32 16 3 27172
fax +32 16 3 27980
www.kuleuven.be